공학박사 학위논문

Materials, Device Design, And Integration Approach for Biodegradable 3D Printable Structural Bioelectronics

생분해성 3차원 인쇄형 바이오 구조전자소자를 위한 재료, 소자 설계 및 집적화에 관한 연구

2023 년 8 월

서울대학교 대학원

재료공학부

이 주 용

Materials, Device Design, And Integration Approach for Biodegradable 3D Printable Structural Bioelectronics

생분해성 3차원 인쇄형 바이오 구조전자소자를 위한 재료, 소자 설계 및 집적화에 관한 연구

지도 교수 강 승 균

이 논문을 공학박사 학위논문으로 제출함
2023 년 8 월

서울대학교 대학원
재료공학부
이 주 용

이주용의 공학박사 학위논문을 인준함
2023 년 6 월

위 원 장 이 관 형 (인)

부위원장 강 승 균 (인)

위 원 선 정 윤 (인)

위 원 설 승 권 (인)

위 원 구 자 현 (인)

Abstract

This thesis presents the development of an additive manufacturing-enabled electronic material that allows for the integration of passive/active electronic components within a customized 3D structure for wirelessly controllable bio interfaced electronics that can provide electrical stimulation and sensing bio-cues in biodegradable form. Furthermore, the thesis includes metamaterials with conductor/frame that is resistant to multi-axial deformation and photoresist that can be primarily patterned onto a 3D structure for in-situ vapor deposition.

In Chapter 1, the needs of additive manufacturing in bio-interfaced electronics is discussed. Conventional approaches, such as thin film/soft electronics for customized contact to bio-construct, employ rigid islands, fully stretchable materials, or reverse engineering. However, these approaches can face reliability issues during attachment, high costs associated with complexity, and limited 3D spatial utilization in terms of designing freedom. Furthermore, claiming needs of integrated voxelated active components for biomedical applications in wireless operation. To address these challenges, the thesis aims to fabricate electronic components in primarily 3D bespoke structure using additive manufacturing.

Chapter 2 focuses on the development of 3D printable biodegradable electronic inks, including conductive, semiconductor, and dielectric inks. Strategies to enhance conductivity in electronic inks are explored, along with novel ideas for semiconductor materials. The investigation of junctions between different inks enables the fabrication of active components based on ohmic, Schottky, and PN junctions. Furthermore, the chapter demonstrates the customized contact of physical, chemical, and biosensors on complex 3D static/dynamic structures.

In Chapter 3, leveraging the biodegradable electronic inks and components developed in Chapter 2, the thesis presents the development of devices for various conformal contact modes, such as surrounding contact, penetration contact, and embedded contact. These devices enable wireless electrical stimulation, 3D spatially organized transduction, and wireless pressure monitoring. Pre-clinical studies involving small and large animal experiments demonstrate the feasibility of wireless stimulation and the therapeutic effects of the developed devices.

Chapter 4 aims to fabricate electronics capable of stable operation under multi-axis deformation. Segregation of both the structural and electronic components within singular negative Poisson's structure entity via multi-material printing. Various sensors/heaters based on structured passive components are fabricated, and integration with pneumatic actuators is demonstrated, showcasing the applicability of the devices on dynamic structures.

In Chapter 5, methods to enable vapor deposition on bespoke forms was explored incorporating new photoresist. An eco-friendly and 3D patternable photoresist is developed, composed of materials known for their biodegradability and high biocompatibility. The patternability of the photoresist is validated on three-dimensional objects, porcine skin, and leaves. It is shown that the photoresist can be developed using water and removed using weak alkaline water or propylene carbonate. It can be used as a mask for electronic fabrication through in-situ vapor deposition or as a mold for fluidics fabrication.

Keyword : Biodegradable electronics, Multi-material printing, Wireless electroceutical, Physical/Chemical/Biosensors, Expandable electronics, 3D Eco-friendly photoresist

Student Number : 2019-30761

Table of Contents

Chapter 1. Introduction 1
1.1. Bio-interfaced electronics
1.2. Current fabrication form factor for customized contact
1.3. Needs of higher form factor fabrication for customized contact
1.4. Additive manufacturing for customized contact

Chapter 2. 3D printed biodegradable electronic system..... 11
2.1. Motivation
2.2. Materials and methods
2.2.1. Materials used for biodegradable printable electronic inks
2.2.2. Characterization of electrical properties of inks
2.2.3. Characterization of electrochemical sintering process
2.2.4. Characterization of rheological properties of inks
2.2.5. Design and multi-material printing of inks
2.2.6. Characterization of printed encapsulation inks
2.2.7. Characterization of mechanical properties of inks
2.2.8. Measurement of energy level of inks
2.2.9. Measurement of passive/active components performance
2.2.10. Characterization of wireless powering system
2.2.11. Characterization of sensors
2.2.12. Formulation of inks
2.3. Results and discussion
2.3.1. Electrical properties of inks
2.3.1.1. Conductivity of inks
2.3.1.1.1. Room-temperature sintering
2.3.1.1.2. Room-temperature grafting
2.3.1.2. Dielectric properties of inks
2.3.2. Rheological properties of inks
2.3.2.1. Humectant
2.3.2.2. Volume fraction of fillers
2.3.2.3. Filler size
2.3.3. Degradation properties of inks
2.3.4. Mechanical properties of inks
2.3.5. Multi-material printing rule
2.3.5.1. XY line gap
2.3.5.2. Z interconnections / periodicity
2.3.5.3. Z line gap
2.3.6. Junctions between inks
2.3.6.1. Conducting inks – Semiconducting inks
2.3.6.2. Semiconducting inks – Semiconducting inks
2.3.7. Passive / Active components
2.3.8. Physical / Chemical biosensors
2.4. Conclusion

Chapter 3. 3D printed biodegradable electronic system for biomedical applictions 76
3.1. Motivation
3.2. Materials and methods
3.2.1. Small animal model
3.2.2. Large animal model
3.2.3. Measurement of electrophysiology
3.2.4. Tissue collection
3.2.5. Immunohistochemistry
3.2.6. Measurement of muscle atrophy and recovery
3.2.7. Statistics
3.3. Results and discussion
3.3.1. Wireless nerve stimulator
3.3.1.1. Design and fabrication
3.3.1.1.1. Electronic components
3.3.1.1.2. 3D integration
3.3.1.2. Performance
3.3.1.3. In-vivo stimulation in small / large animal
3.3.1.4. Therapeutic effects in small animal
3.3.1.5. Accelerated / In-vivo degradation
3.3.2. Plug-in EcoG sensor
3.3.2.1. Design and fabrication
3.3.2.2. In-vivo sensing in small animal
3.3.3. Wireless bone sensor
3.3.1.1. Design and fabrication
3.3.1.2. Performance
3.4. Conclusion

Chapter 4. 3D printed expadnable electronic system 118
4.1. Motivation
4.2. Materials and methods
4.2.1. Preparation of soft electronic inks
4.2.2. Characterization of electrical properties of ink
4.2.3. Characterization of rheological properties of inks
4.2.4. Characterization of mechanical properties of inks
4.2.5. Design and multi-material printing of inks
4.2.6. Measurement of electronic components performance
4.3. Results and discussion
4.3.1. Strategy for expandable structural electronics
4.3.2. Electrical properties of inks
4.3.3. Rheological properties of inks
4.3.4. Mechanical properties of inks
4.3.5. Mechanical properties of missing rib structure
4.3.6. Electronic components within missing rib structure
4.3.7. Pneumatic soft actuator integration
4.4. Conclusion

Chapter 5. 3D patternable eco-friendly photoresist 135
5.1. Motivation
5.2. Materials and methods
5.2.1. Preparation of 3D patternable eco-friendly photoresist
5.2.2. Characterization of rheological properties of photoresist
5.2.3. Characterization of wettability of photoresist
5.2.4. Characterization of coating ability of photoresist
5.2.5. Design and 3D patterning / 3D printing of photoresist
5.3. Results and discussion
5.3.1. Strategy for 3D patternable eco-friendly photoresist
5.3.2. Characterization of photoresist matrix
5.3.3. Characterization of photoresist matrix with inhibitor
5.3.4. Patterning on complex surface / tissue surface
5.3.5. Patterning mask for electronics
5.3.6. Patterning mold for fluidics
5.4. Conclusion

References 152

Abstract in Korean 163

Acknowledgement 165

Chapter 1. Introduction

1.1. Bio-interfaced electronics

Bioelectronics was defined by leading European scientists and industry professionals at the first C.E.C workshop in Brussels in 1991 as "the use of biological materials and biological architectures for information processing systems and new devices"[1]. Medical electronics, on the other hand, was coined at an international conference in Paris in 1958, referring to the combination of electronics engineering and medicine[2]. Both bioelectronics and medical electronics have been developed to measure biological activity, provide stimulation, and create healthcare platforms or treatments by integrating electronic engineering with biological systems[3-6]. In this thesis paper, the concept of bio-interfaced electronics is discussed, which integrates these two fields.

Bio-interfaced electronics aims to seamlessly integrate with biological constructs to record signals, deliver stimulation based on recorded data, and implement diagnostics and therapeutics as a closed-loop system[7]. This field encompasses various market demands. When looking at the global market growth rate, the keyword "Bioelectric Medicine" includes devices such as implantable cardioverter-defibrillators, cardiac pacemakers, cochlear implants, spinal cord stimulators, deep brain stimulators, transcutaneous electrical nerve stimulators, sacral nerve stimulators, and vagus nerve stimulators. The market size is projected to reach $20.1 billion with a compound annual growth rate (CAGR) of 5.8% from 2022 to 2030 [8]. The keyword "Wearable Medical Device," which includes diagnostic and therapeutic devices, is expected to show a high growth rate with a CAGR of 28.1%, reaching $21.3 billion from 2022 to 2030 [9]. The keyword "Brain Computer Interface (BCI)," including invasive BCI, partially invasive BCI, and non-invasive BCI, had a market size of $1.52 billion in 2021 and is projected to have a CAGR of 17.16% from 2022 to

2030 [10].

To ensure the proper functioning of bio-interfaced electronics with high demand, the most critical factor is achieving customized contact with complex bio-constructs to enable accurate and stable communication with biological systems [11-14]. Various approaches have been developed to create flexible and stretchable components, such as thinning materials like silicon to be soft despite having a modulus in the GPa range, or conducting research on intrinsically stretchable materials [3, 4, 12]. Flexible and elastic materials have been proposed for wiring, components, substrates, and encapsulation in electronic devices, leading to diverse designs. [15-17]. Research has been conducted to apply these designs to bio-constructs such as skin and organs for healthcare platforms [13, 18-20]. In this context, this paper aims to discuss the structural and material approaches previously taken to achieve conformal contact.

1.2. Current fabrication form factor of customized contact

Many attempts have been made to create customized contact on the rough / complex surface of bio-construct using processes based on photolithography or large area solution processes to fabricate thin films with reduced bending stiffness or to combine stretchable components for seamless attachment. In the case of flexible electronics fabricated using thin films, conformal contact has been achieved by adjusting the bending stiffness [21]. Bending stiffness is expressed by the equation $EI = Eh^3/12$ (where E is modulus and h is the thickness), and it is influenced by the modulus, particularly through dramatic adjustments based on thickness [21]. When creating active components from inorganic materials, such as silicon, which is crucial elements in semiconductor industry, it is important to fabricate them as nanomembranes using unconventional methods for flexible production [22]. Epitaxially grown silicon nanomembranes have been extensively researched

using transfer printing, a method involving stamping from silicon on wafer (SOI) [23]. There have been also cases where ultra-thin and light-weighted electronics were produced using thin organic semiconducting materials with relatively low modulus [16]. Additionally, there have been examples where templates were produced through electrospinning and metal deposition was performed on top to create gas-permeable nanomembranes with conformal contact [24].

Subsequently, there have been many studies on fabricating components with stretchable structures to achieve stable integration into complex curvatures or high-aspect ratio structures and dynamic bioconstructs that change shape over time[25]. To create stretchable devices, two main approaches have been explored: using a structure with rigid islands and using materials that are fully stretchable[25].

In the case of the structural solution, known as rigid islands, rigid devices are components made of silicon-based chips or flexible materials[25]. These devices are connected to stretchable conductors and a stretchable substrate to make them stretchable. Various methods, such as mechanical cutting, photolithography, laser cutting, and spinning, have been used to make the conductors stretchable[25]. Some examples include:

(1) Serpentine structures, which have a wavy shape that provides stretchability. The basic structure typically has an stretchability of about 30%[15]. The stretchability is defined by the in-plane design of the electrode and the structural flexibility in the out-of-plane direction[25]. In cases where there is no substrate, stretchability can reach over 1600% strain[26]. Factors that affect stretchability include bending, conductor thickness, substrate stiffness, and adhesion between the conductor and substrate[27, 28].

(2) Mesh structures allow for the adjustment of stretchability through various internal designs. For the basic square-shaped openings, a stretchability of 25% has been observed[29]. Kirigami structures with thin-line cuts have also been introduced to achieve high stretchability, with certain structures capable of elongation up to 1100%[30, 31]. Additionally, gas-permeable nanomembranes discussed earlier are made up of a network of nanofibers. When transferred onto a PDMS substrate, the sheet resistance was measured to be 17Ω/sq, and the stretchability reached approximately 50%[32].

(3) Longitudinal wave structures refer to conducting lines that pop up with a regular period in the out-of-plane direction[33]. Stretchability is achieved by utilizing the phenomenon of buckling, where the buckled structure unfolds in the in-plane direction[33]. In many cases, a prestretched elastomeric substrate is used for deposition or lamination of a conducting film[34, 35]. This approach has been applied not only to metals but also to semiconductors as nanoribbon[36]. By patterning nodes for adhesion on the substrate, prestretching the substrate, and depositing a film, stretchability up to 1.2% for rectangular-shaped GaAs and up to approximately 30% for serpentine-shaped Si ribbon structures have been achieved [36, 37].

In the case of material solution which has intrinsic stretchability, some examples include :

(1) Liquid metals are conductive liquids with infinite elongation capability with high conductivity (>10^4 S/cm)[38]. Non-toxic metals such as gallium (Ga) alloyed with indium (In) in the form of EGaIn or alloyed with indium (In) and tin (Sn) in the form of Galinstan are commonly used[38]. It has been observed that strains of up to 800% can be achieved when these liquid metals are placed in fluidic channels within elastomeric fibers[39]. However, they tend to oxidize easily, so addressing this issue is crucial. Patterning

can be achieved through wettability control during printing, photolithography, or laser ablation[38].

(2) Ionic conductors refer to electrodes composed of ions and ionic liquid-based hydrogels[40]. These gels exhibit high stretchability (>600%) while maintaining good ion conduction[41]. Although their conductivity is low (10^{-3} S/cm), they maintain softness with Young's modulus in the range of 10-100 kPa, even when millimeters thick[41].

(3) Conducting polymers can exhibit hole mobility in completely dry states or mixed transport of ions and electrons in the presence of water[42]. In the case of mixed ionic conduction, it is possible to reduce interfacial impedance, enabling various applications such as electrophysiology, actuators, and batteries[43-45]. Poly(2,3-dihydro thieno-1,4-dioxin)-poly(styrenesulfonate) (PEDOT:PSS) has garnered significant attention and research as a stretchable conductor[46]. In its natural state, PEDOT:PSS exhibits only about 5% elongation, but plasticizers have been used to address this limitation[47, 48]. For example, when Triton-X is used, it shows elongation of 60% and conductivity of 78 S/cm. The use of ionic salts results in even higher elongation and conductivity. This is because the ionic salts reduce the electrostatic interaction of PSS and improve the crystallinity of the conductive region, PEDOT[49-51]. When bis(trifluoromethane) sulfonamide lithium salt is used, conductivity exceeding 4100 S/cm at 100% strain has been observed[50]. There are also cases where conductivity is enhanced through morphological changes and doping by ionic liquids[52].

1.3. Needs of higher form factor fabrication for customized contact

As discussed earlier, various strategies have been used to implement customized contact of planar electronics on static or dynamic three-dimensional surfaces, combining thin structures and

soft materials with stretchability. When there is a material's elastic limit, reverse engineering is used to analyze prerequisite design parameters and apply contact to the target area using origami/kirigami structures[53, 54]. These approaches are truly exceptional, and I firmly believe that their prominence will significantly increase in the future. At this moment, for complex structures including Riemann's surface, dynamic deformation in limited jagged volumetric spaces I have claimed several missing features regarding this approach where customized contact is achieved through structural deformation:

(1) The reliability of attachment techniques for handling the deformation of free-standing ultra-thin components and accurately targeting specific areas on tubular, branched networks (vessels, nerve), high aspect ratio array surfaces.

(2) Mechanical reliability during operation periods, considering additional multidimensional deformations that may exceed the failure elongation of the materials while maintaining conformal contact with dynamic targets. In other words, designing structures that consider conformal contact and deformation from the initial stage is essential.

(3) The increased calculation for cost associated with reverse engineering as the complexity rises.

(4) Integration efficacy may decrease when applied to structures with a high aspect ratio within complex curvatures in three-dimensional space due to the consideration of deformation in physically stretchable components.

(5) When integrating with volumetric artificial constructs rather than biological construct surfaces, there is a possibility of low space utilization due to wrapping or occupying space only through the surface. In this regard, efficient space utilization means that

connecting points on the surface of a sphere with a radius of 1 centered at (0, 0, 0) using XY, YZ, and XZ planes is less efficient than drawing a diagonal line (1, 1, 1).

Therefore, I considered the need for a higher form factor fabrication process that allows customized contact on three-dimensional surfaces from the initial fabrication stage, enable higher space utilizations and not incurring high costs based on complexity. So as to figure the issues, we needed voxelated multiple materials which can be placed in 3D space within customized contact from the initial stages.

1.4. Additive manufacturing for customized contact

Additive manufacturing is a method of fabricating objects by layer-by-layer deposition of materials, allowing for on-demand fabrication tailored to the desired design. It enables prototyping in cases where continuous design modifications are needed[55, 56]. Additionally, it is eco-friendly as it reduces waste and has significantly lower power consumption compared to traditional vacuum deposition methods[57, 58]. Additive manufacturing builds structures via data-driven voxelated multi-materials configuration, including electronic materials, responsive materials, and cells, within an on-demand / single step fabrication process[59-62]. The integration of diverse materials enables the creation of multifunctional structures, going beyond mere structural support. As a result, it finds applications in fields such as wearable electronics, soft actuators, and artificial biomedical implants[63-66].

However, the previously raised concerns need to be discussed in comparison with the resolution of additive manufacturing and conventional fabrication methods, as factors like integration efficacy are directly influenced by resolution. For multi-materials configuration, conventional methods typically operate at the scale of

< 1 μm[67], while additive manufacturing, especially direct ink writing, achieves a resolution of ~100 μm[68, 69], indicating that conventional methods are expected to have better integration efficacy. Although there are active research efforts to improve resolution through nanoprinting, the simultaneous nanoscale printing of conductors, semiconductors, and dielectrics is still not widely developed[70–74]. Even if advancements have been made in conductive and semiconductive materials, the level of printing them together with structural components to realize structural electronics integration is still limited. While conventional methods seem to offer better integration efficacy, there are still reliability issues when customization is not considered from the initial state, cost implications due to high complexity, and limited space utilization with low designing freedom within the 3D structure. Therefore, research on producing bio–interfaced electronics through additive manufacturing is seen as a viable option to explore.

Due to the limitations imposed by low resolution, the types of electronic devices that can be produced through additive manufacturing are not aimed at achieving the performance of processing chips such as CPUs or GPUs. Instead, the goal should be to create components capable of wireless communication, receiving information from external sources or transmitting device information through near field communication (NFC) with a certain level of performance. Assuming that a single complementary metal–oxide–semiconductor (CMOS) transistor is integrated into each device and considering a nanofabrication process that allows for the integration of 18 billion devices in a 602 mm^2 area[75], additive manufacturing with a feature size of 100 μm would enable the integration of approximately 3000 devices. As the feature size decreases to a few micrometers, even more devices can be integrated. Considering that NFC tags may require near 1000 devices[76], it is believed that advanced printing techniques could be used to achieve this.

Alternatively, the quests can be modified to include the printing of small information processing units such as rectification units or logic units, along with wiring that allows for sensing external environments using various indicators, while ensuring high space utilization. In this case, considerations must be given to the integration with chips fabricated through conventional methods. However, one challenge that arises when considering the junction between the chip and wiring is the issue of heterogeneous integration, which can introduce additional reliability concerns. Therefore, it may be necessary to integrate electronic materials composed of a homogenous matrix to address the junction problem.

Looking at the current examples of bio-interfaced electronics that have been 3D printed, we can see cases such as instrumented micro-physiological systems combined with cardiac cells[77], in-situ printing of pressure sensors on expanding surfaces[78], connection of SMD chips and stretchable passive component-based sensors using pick and place methods[79, 80], modeling similar to an aortic valve with embedded pressure sensors[81], creation of neural probes using soft conductive polymers[82], patches capable of recording and stimulating with the presence of cardiac cells[83], patches for electrical hemostasis inside blood vessels[84], sensors capable of detecting UV-VIS while attached to the skin[85], implementation of electronics based on hydrogel matrix blended with Ag flakes[86], combination with cardiac organoids for spatio-sensing[87], and attempts to create electronic blood vessels through screen printing, although not strictly 3D printing[88].

These examples mainly aimed to print biocompatible conducting materials, but they relied on connections with external devices and posed difficulties in achieving wireless functionality. Although researchers worked on ink-writing or aero-jetting based active components such as LEDs, OLEDs, electrochemical transistors, and their integrated circuits exist, the components are not capable of being structural components in final product[89-93]. To make truly

voxelated semiconductors, it should provide structural components and electronic components. Also soldering is needed to integrate components which causes reliability issues between heterogeneous materials.

Therefore, the goal was to conduct research on developing a voxelated conductor, semiconductor, dielectrics including biocompatibility within homogeneous matrix to allow three-dimensionally configuring electronic components for wireless operations of therapeutics and diagnostics in diverse structures applicable for bio-interfacing such as tubes, branched pipes, scaffolds by on-demand additive manufacturing in a single step.

Chapter 2. 3D printed biodegradable electronic system

2.1. Motivation

With the miniaturization, flexibility, and wirelessization of electronic components, the utilization of implantable medical devices has also garnered attention. Implantable medical devices are directly inserted into the body tissues to provide precise/real-time diagnostics and deliver direct and concentrated treatment to the affected area. Due to these irreplaceable advantages, despite the drawback of requiring invasive surgery, it is expected to continue to evolve and develop as a major future healthcare industry for early disease diagnosis and post-treatment. It is recommended that these implantable medical devices be removed after use. Residual devices in the body can cause damage to internal organs through movement and foreign body reactions, as well as lead to problems such as bleeding and infection[94]. Surgical removal to prevent this can result in secondary issues such as additional infections and damage during the removal process. Particularly in the case of complex surgeries such as deep tissue surgery, the risk of additional surgeries dramatically increases during the process of removing fibrous tissues[95]. For example, in cardiac surgery, cases of excessive bleeding leading to death have been frequently reported, and removal surgeries for cardiac pacemakers have recorded a failure rate of approximately 20%[96]. Biodegradable implantable medical devices eliminate the need for additional removal after completing their function at the local site, thereby reducing the secondary risks[97-101].

In applying implantable electronic devices, human tissues and organs possess unique functions and exhibit diverse and complex shapes[102]. Even for the same organ in different patients, the shape can vary depending on age and gender. Therefore, the design

and fabrication methods for customized medical devices that match the internal tissues or organ structures are necessary. In such situations, existing technologies have mainly emphasized conformal contact based on thin-film electronics. However, there are difficulties in separately fabricating and integrating modules such as electrodes, circuits, communication components, and power sources within the limited and complex space. Several issues need to be addressed in this regard. (1) Placing standardized modules in a 2D plane reduces space utilization within the limited internal body space, and mechanical reliability may decrease when deformation is required for conformal contact. (2) Various process equipment, including spin coating, photolithography, and thin-film deposition, are required to fabricate each module, and multi-step processes are needed. (3) During soldering and packaging, excessive thermal, mechanical stress driven residual stress caused by the junction of dissimilar materials can lead to damage or fracture, and other issues in the complex internal environment.

To overcome these challenges, a 3D additive manufacturing is required, where semiconducting, conductive, and dielectric electronic materials, as well as structural and packaging materials, are all produced and packaged in a single step without the need for masks or molds, using a homogeneous matrix. (1) It will be better using a single equipment capable of processing all electronic materials and packaging substances, which reduces the costs and power consumption needed for large process equipment and inter-process transportation[83]. Additionally, (2) using a homogeneous matrix for all products enhances material compatibility and mitigates residual stress generated during the junction of dissimilar materials. Furthermore, (3) with electronic design and a single with electronic design and a single 3D printer loaded with electronic materials in a cartridge, fabrication can be carried out at any site, allowing for rapid application in medical facilities and hospitals after imaging the patient's affected area.

2.2. Materials and methods

2.2.1. Materials used for biodegradable printable electronic ink

Filler :

Zinc powder (dust, <10 μm, 98%, 209988-1KG, Sigma-Aldrich, Inc), Molybdenum powder (800nm, 99.9%, US Research Nanomaterials, Inc), Tungsten powder (5 μm, 99.9%, US Research Nanomaterials, Inc), Iron powder (800 nm, 99.9%, US Research Nanomaterials, Inc), Zinc Oxide (ZnO, 99.9+%, 500nm, US Research Nanomaterials, Inc), Zinc Oxide Doped with 2wt% Aluminum powder (AZO, 99.9%, 300nm, US Research Nanomaterials, Inc), Milled P type silicon wafer (4" x 0.525 mm, <100>, B doped, 0.001-0.002 ohm cm, prime, Taewon scientific co., ltd) 100 – 300 nm, in pH11 with DLS analysis (Milling condition, 600 RPM, 12 h, 12g wafer with Zirconia ball 10mm : 3mm = 70g : 30g), Magnesium Oxide powder (MgO, 99+%, 40 nm, US Research Nanomaterials, Inc), Silicon nitride powder (Si3N4, ≥98.5%, <50 nm, Sigma-Aldrich, Inc), Silicon Dioxide (SiO2, 99+%, 20 - 30nm, US Research Nanomaterials, Inc), Iron (Ⅱ, Ⅲ) oxide powder (Fe3O4, 95%, < 5 μm, Sigma-Aldrich, Inc), Molybdenum Oxide (MoO3, 99.9%, 6 μm, US Research Nanomaterials, Inc)

Binder :

Polycaprolactone (PCL, average Mn 80,000, Sigma-Aldrich, Inc), Polybutylene adipate terephthalate (S-EnPol co., ltd)

Solvent :

THF (Tetrahydrofuran anhydrous, 99.8%, Daejung co., ltd), Chloroform (99.5%, Daejung co., ltd)

Humectant :

Tetraglycol (Bioxtra, non-ionic, Sigma-Aldrich, Inc)

Conjugated molecule :

Guanine (98%, Sigma-Aldrich, Inc), Indigo (Dye content 95%, synthetic, Sigma-Aldrich, Inc), Brilliant Yellow (Dye content ≥50%, Sigma-Aldrich, Inc), Curcumin (from Curcuma longa (Turmeric), powder, Sigma-Aldrich, Inc), Solvent Green 3 (Dye content 95%, Sigma-Aldrich, Inc), Indigo carmine (certified by the Biological Stain Commission, Dye content 85%, Sigma-Aldrich, Inc), β-Carotene (synthetic, ≥93% (UV), powder, Sigma-Aldrich, Inc)

Reagents & Buffer solution :

Ultra-pure water (EXL, water purification system, 18.2 MΩ·cm @25℃), Acetic acid (glacial, 99.5%, Sigma-Aldrich, Inc), pH buffer solution (pH 4.00 ± 0.02 @25℃, pH 10 ± 0.02 @25℃, Samchun pure chemical co., ltd), PBS 1X solution (pH 7.4 ± 0.1, Sterile-filtered, Samchun pure chemical co., ltd), Agarose (Higel-agarose ClearTM, biotechnology grade, E&S Bio Electronics Company, Inc), Sodium Chloride (Daejung.Inc), Glucose oxidase from Aspergillus niger (Type X-S, lyophilized powder, 100,000 - 250,000 units/g solid, Sigma-Aldrich, Inc), Ferrocene (98%, Sigma-Aldrich, Inc), D-(+)-Glucose (≥99.5% (GC) Sigma-Aldrich, Inc

2.2.2. Characterization of electrical properties of inks

Conductivity :

The inks were screen-printed via stencil mask or extruded via nozzle into mold on polyimide (PI) taped glass substrate, and the geometrical parameter was scanned and measured. LCR meter (4100, Wayne Kerr Co., Ltd) and Digital multimeter (DT4282, HIOKI) were used to measure the resistance of the traces, and conductivity was calculated.

$$\sigma_{ink} = \frac{1}{\rho_{ink}} = \frac{l}{Rwt}$$

Terms are σ is conductivity, ρ is resistivity, R is resistance, l is

length of resistor, w is width of resistor, and t is thickness of resistor.

Dielectric constant, Capacitance :

Film formed by solvent casted inks was coated with Pt on double side of the film. Thin film deposition on nanocomposite film was to make no gap between metal plate and film which work as parasitic capacitance interfering capacitance measurement. Digital multi meter (DT4282, HIOKI) was used to measure DC capacitance of the film.

$$\varepsilon = \frac{Cd}{A}$$

Terms are ε is dielectric constant, C is capacitance, d is length between two metal plate which we measure as film thickness, and A is area of metal plate. Capacitance of 3D printed capacitor was characterized with LCR meter (4100, Wayne Kerr Co., Ltd) and Digital multimeter (DT4282, HIOKI).

2.2.3. Characterization of electrochemical sintering process

Printed conducting trace was wired at two terminal edges and immersed in a 10% acetic acid solution. Resistance of the trace was measured by immersion time in the solution. XRD (X-Ray Diffractometer (Xpert Pro (HR-XRD), PANalytical)) analysis was performed to verify the formation of acetate passivation layer in printed Zn trace. Scanning electron microscope (SEM) and energy dispersive spectroscopy (EDS) (Merlin Compact (FE-SEM), ZEISS) was used to verify the existence of porosity of inks for acetic acids to be permeated through within reactive diffusion model and to verify electrochemical sintering.

2.2.4. Characterization of rheological properties of inks

Rheometer (MCR 702e MultiDrive, AntonPaar) was used to characterize rheological behavior of possible candidates of inks for 3D printing. Inks were placed at cavity between two plates (gap = 0.5 mm), for sweep mode, viscosity was measured within shear rate range of 0.1 to 100 s−1 in 25℃ and for amplitude mode, storage and loss shear modulus was measured within shear strain range of 0.01 to 10 % at angular frequency 10 rad/s. Oil was introduced at the perimeter of top plate after ink load to prevent solvent vaporization while measurement.

2.2.5. Design and multi−material printing of inks

Modelling was performed by Autodesk Fusion 360, sliced by Repetier−Host, and generated G−code for the shape−adapted customised components. G−code was manipulated to generate a path for each material with Hamiltonian path to reduce printing time. Then G−code was transferred to 3D printer (BIOX, Cellink, inc) having multi nozzles that can print three materials at one step. For cases with more than four materials or post treatment in between printing steps, a zero point was set at a near object on the substrate and calibrated using the standard at each step.

2.2.6. Characterization of printed encapsulation of inks

Printed inks were on glass with PDMS containing PBS inside and incubated in an oven at 37℃. SEM image also verified the degradation of fillers and binders on the surface of the inks. Encapsulation layer was examined by measuring doubling time of encapsulated conducting inks which is wired for resistance measurements. Printed ink resistance was measured for incubation time and a set doubling time, with a time point twice larger than the initial resistance.

2.2.7. Characterization of mechanical properties of inks

The inks were printed with 0.5–1 mm thickness, 5–6 mm width, 30 mm length, and strain–stress curves were obtained by dynamic mechanical analyser (DMA Q800, TA Instruments, USA). Furthermore, uniaxial tensile tester (customised, jueuntech, Korea) was used to test stability of resistance of Mo–PBAT trace within flexural strain.

2.2.8. Measurement of energy level of inks

Kelvin probe in Atomic Force Microscope (NX–10, Park systems) was used to measure work function of conducting inks (Zn, Fe, Mo, W). UPS (ultraviolet photoelectron spectroscopy) by Electron spectroscopy for chemical analysis Ⅱ (AXIS SUPRA, Kratos, UK) was used to measure work function and valence band level of semiconducting inks (ZnO). UV–VIS spectrometer (Microplate Spectrophotometer, Epoch 2, Bio Tek Instruments) was used to measure band gap of semiconducting inks and conjugated molecules.

2.2.9. Measurement of passive/active components performance

Passive components (resistor, capacitor, inductor) were characterized by LCR meter and DMM. Active components (diode, transistor) were characterized by Semiconductor analyzer with probe station (4200A–SCS Parameter Analyser, Keithley) by measuring I–V curve.

2.2.10. Characterization of wireless powering system

Absorbance of printed RF antenna and wireless stimulator was characterized by vector Network Analysers (TTR500 Series, 100 kHz to 6 GHz, Tektronix co., ltd), which measured S–parameters and impedance by frequency. Wireless powering by the external

device was performed by a combination of Arbitrary Function generator (AFG 31000 SERIES, Tektronix co., ltd), RF amplifier (210 L, E&I co., ltd for small animal, High-speed biopolar amplifier BA4850, DC to 50 MHz, 8W max, output voltage ±20 V, output current ±1 A, NF corporation co., ltd for large animal), and adjusted transmission frequency, amplitude, burst mode (interval, cycle). The wireless operation of the device was measured with Digital Oscilloscope (TBS 1052B, 50MHz, 1GS/s, Tektronix co., ltd)

2.2.11. Characterization of sensors

Temperature sensor was measured with resistance by DMM and LCR meter (AC, 20Hz) with sample placed on temperature varying print bed. For pressure sensor, AC capacitance by LCR meter (1 MHz,10 mV) was measured with an external load on electrode and pressure were calculated from division of load and the interfacing area. UV sensor was measured with conductance by LCR meter under UV lamp (365nm, 15 W). pH sensor was measured with open circuit potential in two electrode system with potentiostat (DY2100) in a cell using reference of Ag/AgCl electrode. Glucose sensor was measure with response current in three electrode system with potentiostat (V = −0.2 V) in a cell with Ag/AgCl electrode for reference and platinum electrode for counter electrode.

2.2.12. Formulation of inks

Binder solution :

(1) Put solvent (THF, Chloroform) 30 ml in glass vial
(2) Put magnetic bar in the solvent and stir (RPM ~ 250)
(3) Weigh pellet of binder to make PCL/THF 0.15 g/ml and PBAT / Chloroform 0.2 g/ml and put the pellets in solvent while stirring
(4) Seal vial with Teflon tape and wait for it disperse well

3D printable inks :

(1) Weigh adequate amount of fillers and put in 35 ml container

(2) Weigh 0.5 ml of tetraglycol and put in the previous 35 ml container

(3) Put 1 ml of binder solution in the previous 35 ml container via norm-ject syringe

(4) Then rapidly close the container and seal with Teflon tape

(5) Weigh container's total mass and adjust balance of planetary centrifugal mixer (ARM-310, Thinky mixer) with 2000 rpm, 2m 30s.

(6) Weigh container's total mass after blend to check solvent dry

Ink loading in print head :

(1) Load ink into 3 ml barrel (EFD Norsdon) and pack with white piston and orange piston serially.

(2) Eject a small amount of ink then rapidly close tip and end with cap (Teflon sealed).

(3) Ink filled barrel is transferred to printhead

2.3. Results and discussion

2.3.1. Electrical properties of inks

2.3.1.1. Conductivity of inks

In the case of conductor composites, the conductivity undergoes a sharp increase at a certain threshold volume fraction of fillers known as the percolation threshold. This relationship is expressed as follows[103]:

$$\sigma_{composite} = \sigma_{filler}(\rho_{filler} - \rho_c)^t$$

Here, $\sigma_{composite}$, σ_{filler}, ρ_c, t represent the conductivity of the printed ink, conductivity of the conductive fillers, threshold volume fraction of fillers for percolation, and critical power law component,

respectively. In this study, the volume fraction calculation was conducted considering only the filler and binder, as follows:

$$\rho_{filler} = \frac{V_{filler}}{V_{filler} + V_{binder}} = \frac{\frac{M}{d}_{filler}}{\frac{M}{d}_{filler} + \frac{M}{d}_{binder}}$$

However, in cases where there are fillers, binders, and humectants, it is defined as:

$$\rho_{filler} = \frac{V_{filler}}{V_{filler} + V_{binder} + V_{humectant}} = \frac{\frac{M}{d}_{filler}}{\frac{M}{d}_{filler} + \frac{M}{d}_{binder} + V_{humectant}}$$

Here, M represents mass, V represents volume, and d represents density. However, the intergranular conductivity between fillers within the composite is often hindered by the native oxide layer of the fillers, which requires tunneling through the matrix and native oxide layer for electron conduction. Therefore, even if a percolating network is formed, it does not result in the desired conductivity for electronic devices. In particular, biodegradable metals such as Zn, Mo, and Fe are prone to oxidation compared to noble metals (Ag, Cu, etc.) or carbon-based conductors (carbon nanotubes, graphene, etc.)[104]. Thus, to enhance intergranular conductivity, sintering can be performed to establish lattice connections between fillers, resulting in increased electron conduction. However, for biodegradable electronics, which use biodegradable polymers as the matrix, low melting points (e.g., PCL at 60°C) necessitate conductivity enhancement strategies that can be carried out at room temperature. For conductors, electrochemical sintering methods previously reported in the literature were optimized for the specific materials[105-107]. For semiconductors, since there is no room temperature sintering method available, considering the use of conjugated molecules to create indirect conduction was a possible approach[108, 109].

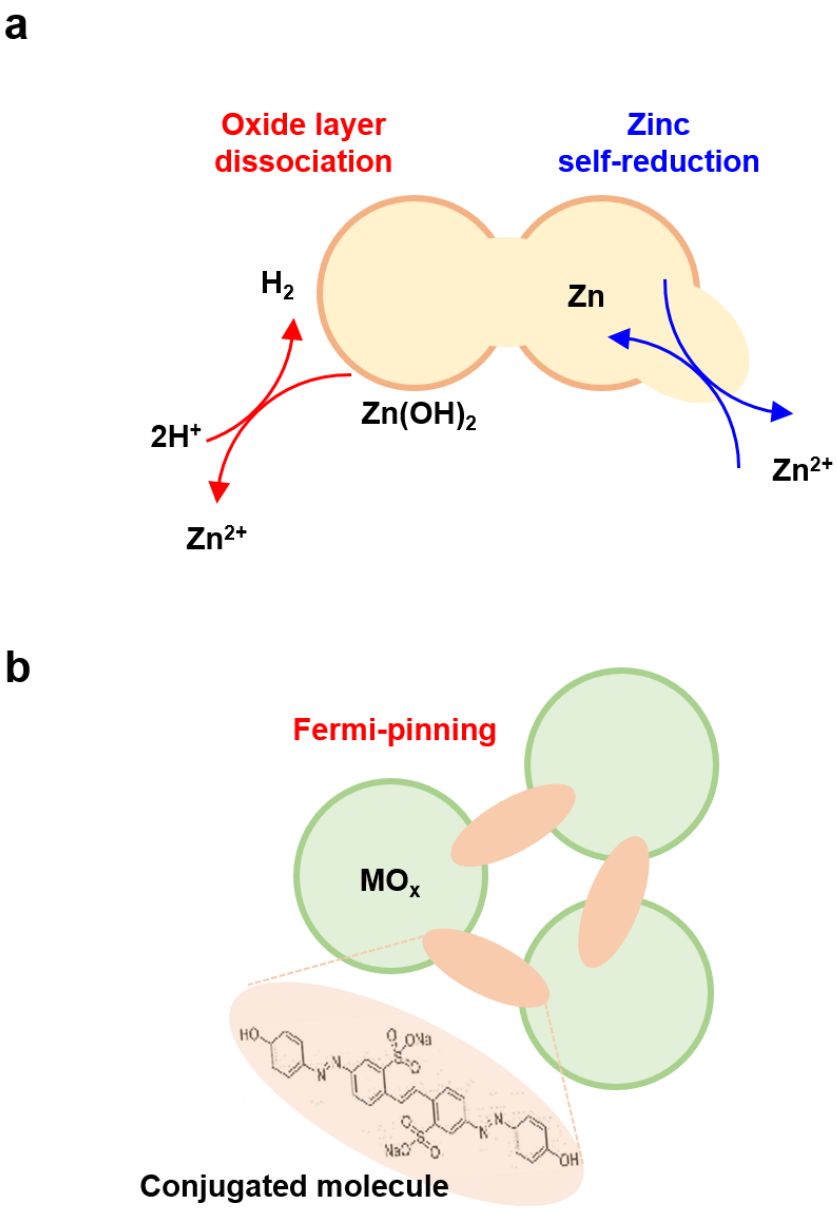

Figure 1. Conductivity enhancement strategy in voxelated biodegradable electronic ink (a) Room-temperature sintering (b) Room-temperature grafting

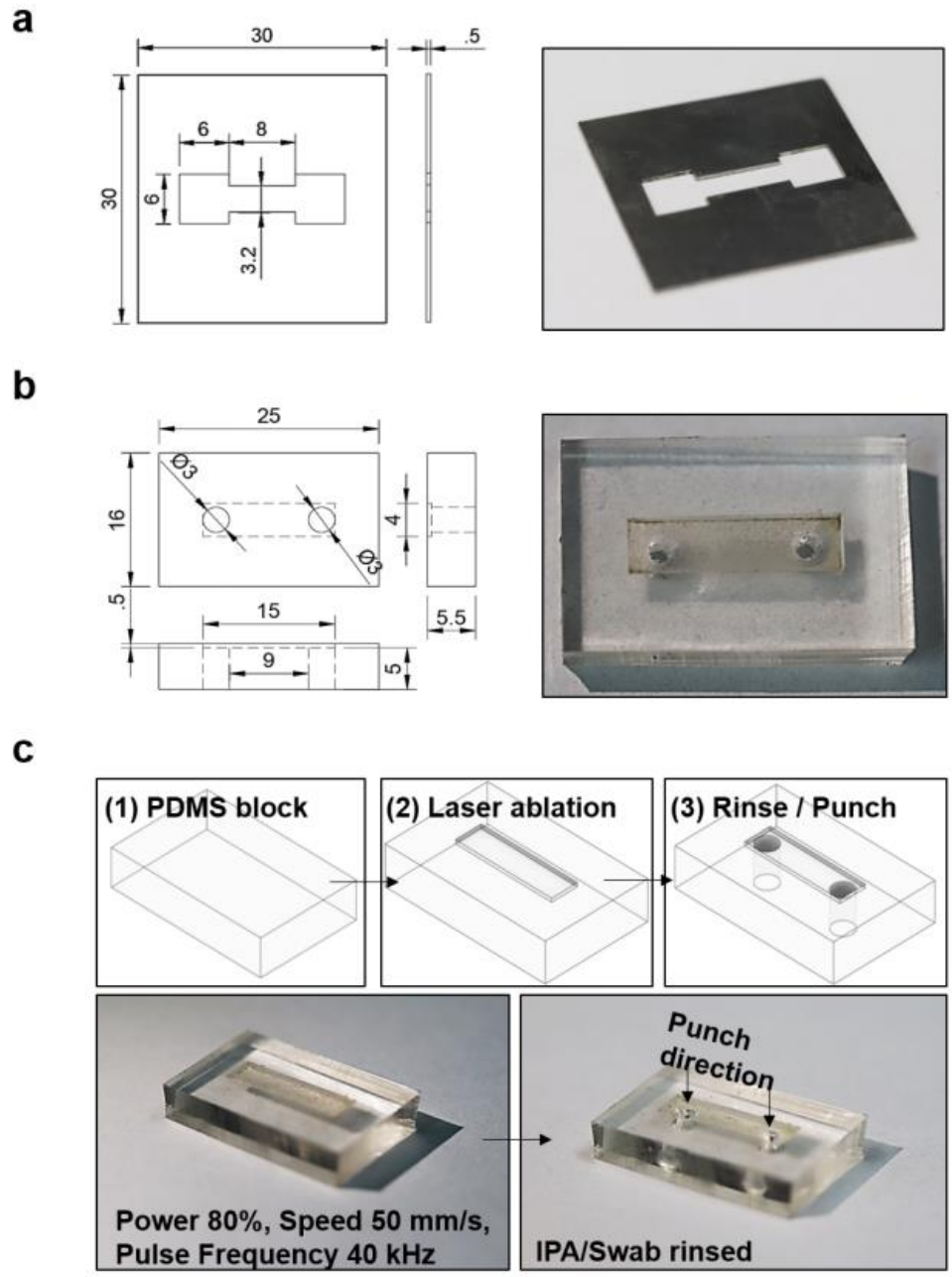

Figure 2. Stencil mask and PDMS mold for conductivity measurement sample (a) For filler+binder+solvent (b,c) For filler+biner+solvent+humectant

2.3.1.1.1. Room-temperature sintering

Variation in the conductivity of a screen-printed and electrochemically sintered Zn-PCL trace in 10% acetic acid for approximately 10 minutes (3.2 mm (W) × 0.1 mm (H) × 14 mm (L)) was observed. The conductivity showed a dramatic increment at around 40 vol% of Zn fillers, reaching values greater than 10^3 S/m. When the actual percolation network equation was applied, a larger value of t = 2.5 was obtained.

Electrochemical sintering of the printed Zn-PCL trace (2.86 mm (W) × 0.97 mm (H) × 9.41 mm (L)) in 10% acetic acid rapidly enhanced conductivity and saturated within 10 minutes, resulting in conductivity increases of up to ~2×10^7 times. This sintering mechanism involves the self-exchange of Zn/Zn^{2+} at the Zn/H_2O interface. The native oxide layer is dissolved by the acidic solution, generating Zn^{2+} at the Zn/H_2O interface. Zn^{2+} then self-reduces on the Zn surfaces, inducing direct contact between percolated Zn fillers. After drying the Zn ink, acetate anions(ac) produced from the corrosion reaction of Zn and CH_3COOH form a new passivation layer, $Zn(ac)_2$, covering the welded solid[105]. We confirmed the direct interface between Zn fillers in the PCL matrix via the sintered path and the formation of the $Zn(ac)_2$ passivation layer after the sintering process using SEM images and XRD analysis.

Among the four types of metal fillers that are 3D printable in the PBAT matrix, Zn showed the best conductivity enhancement effects with the highest conductivity which seems to show the only one element undergone sintering process. The initial conductivity values seemed to follow the order Fe < Zn < Mo < W. These initial values are relevant to the reduction potential (vs SHE) = −0.76(Zn^{2+}/Zn), −0.44(Fe^{2+}/Fe), −0.2(Mo^{3+}/Mo), −0.09(W^{4+}/W)), which is consistent with the reactivity of the metals[105].

Modeling on the sintering process was conducted, specifically

using a reactive diffusion model[110]. This choice was made because estimating the sintering time internally, based on the external sintering solution, is important for structural electronics. The electrochemical sintering kinetics can be described by analytical models of the reactive diffusion model, where the rate determining step is defined by the diffusion of CH_3COO^- ions and H^+ ions into the printed inks throughout the thickness direction (z). This can be expressed as :

$$D\frac{\partial^2 w}{\partial z^2} - kw = \frac{\partial w}{\partial t}$$

where D and k represent the diffusivity for CH_3COOH in the porous ink structure (P) and the reaction constant reflecting the formation of the Zn/Zn^{2+} interface, which consumes acetic acid due to the chelation of Zn^{2+} for the interface, respectively. The concentration of CH_3COOH is denoted by w.

Following boundary conditions and initial condition are used for the diffusion equations.

(1) $w\ (z = H_0) = w_0$ (Constant acetic acid at top)
(2) $\partial w/\partial z\ (z = 0) = 0$ (No flux of acetic acid at bottom)
(3) $w\ (t = 0) = 0,\ (0 \leq z \leq H_0)$ (Zero concentration of acetic acid)

In this model, for times (t) before complete sintering between Zn fillers, the thickness of the non-sintered porous trace (H) decreases approximately linearly with t, as given by following equation:

$$H = H_0 - \alpha\sqrt{kD}\ t\ tanh\sqrt{kH_0^2/D}$$

where H_0 represents the initial thickness of the printed trace, $M(CH_3COOH)$ and $M(P)$ are the molar masses of acetic acid and porous P, respectively, w_0 is the initial water concentration, n_P is the number of CH_3COOH molecules reacting with P, ρ_P is the mass density of P, and α is a constant with $\alpha = \left[\frac{M(P)}{M(CH_3COOH)}\right] w_0/(n_P \rho_P)$.

The saturation time for the thickness to reach zero can be approximated as:

$$t_{H=0} = \frac{H_0}{tanh\sqrt{kH_0^2/D}\ \alpha\sqrt{kD}} = C^*(H_0)H_0$$

Since $R_{sintered} \ll R_{non-sintered}$, the total resistance of the trace at time (t) can be formulated as:

$$R_{total} = \frac{C^*(H_0)L}{\sigma_{sintered}Wt} + R_{contact}\ (t \le t_{H=0})$$

where $\sigma_{sintered}$ represents the conductivity of the completely sintered P, L is the length of the trace, W is the width of the trace, and $R_{contact}$ is the resistance between the probe and the trace.

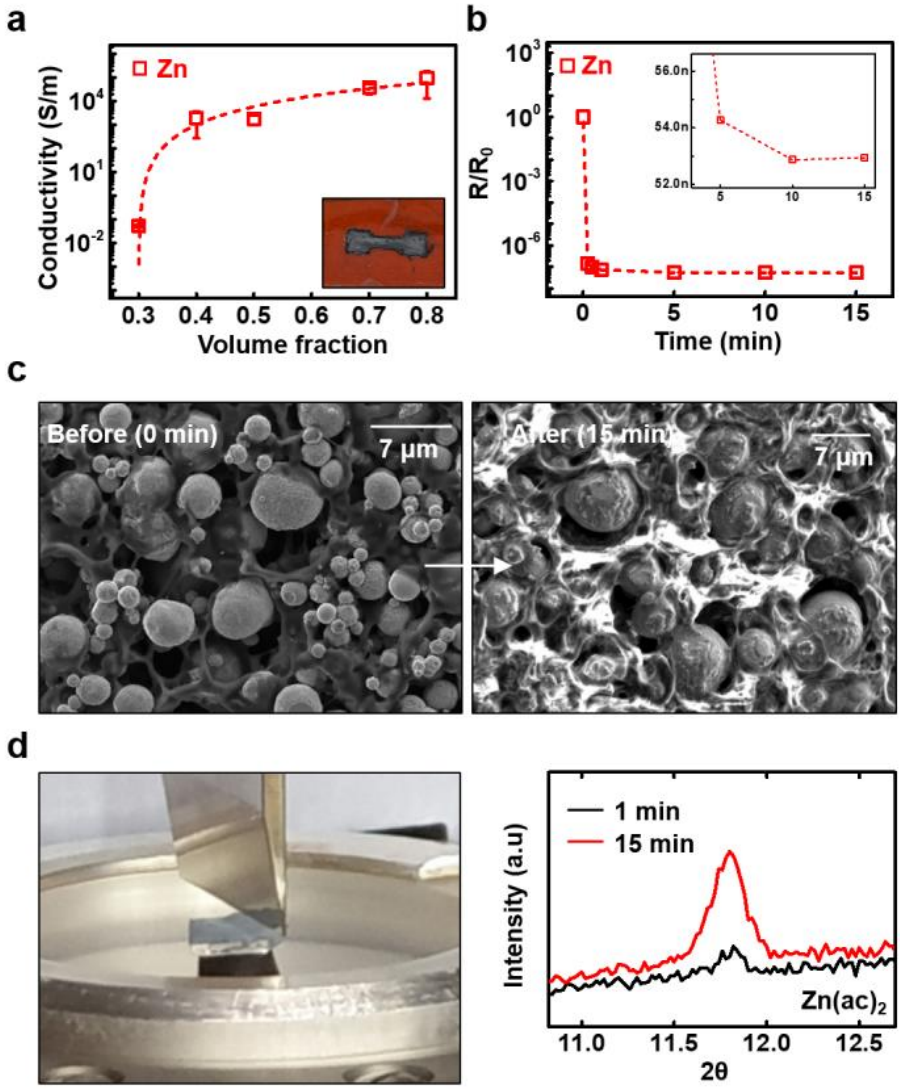

Figure 3. Characterization of room temperature sintering for Zn-PCL ink (a) Conductivity change by volume fraction in printed ink via stencil mask (b) Resistance change, (c) SEM image, and (d) XRD data of Zn-PCL by immersion time in acetic acid

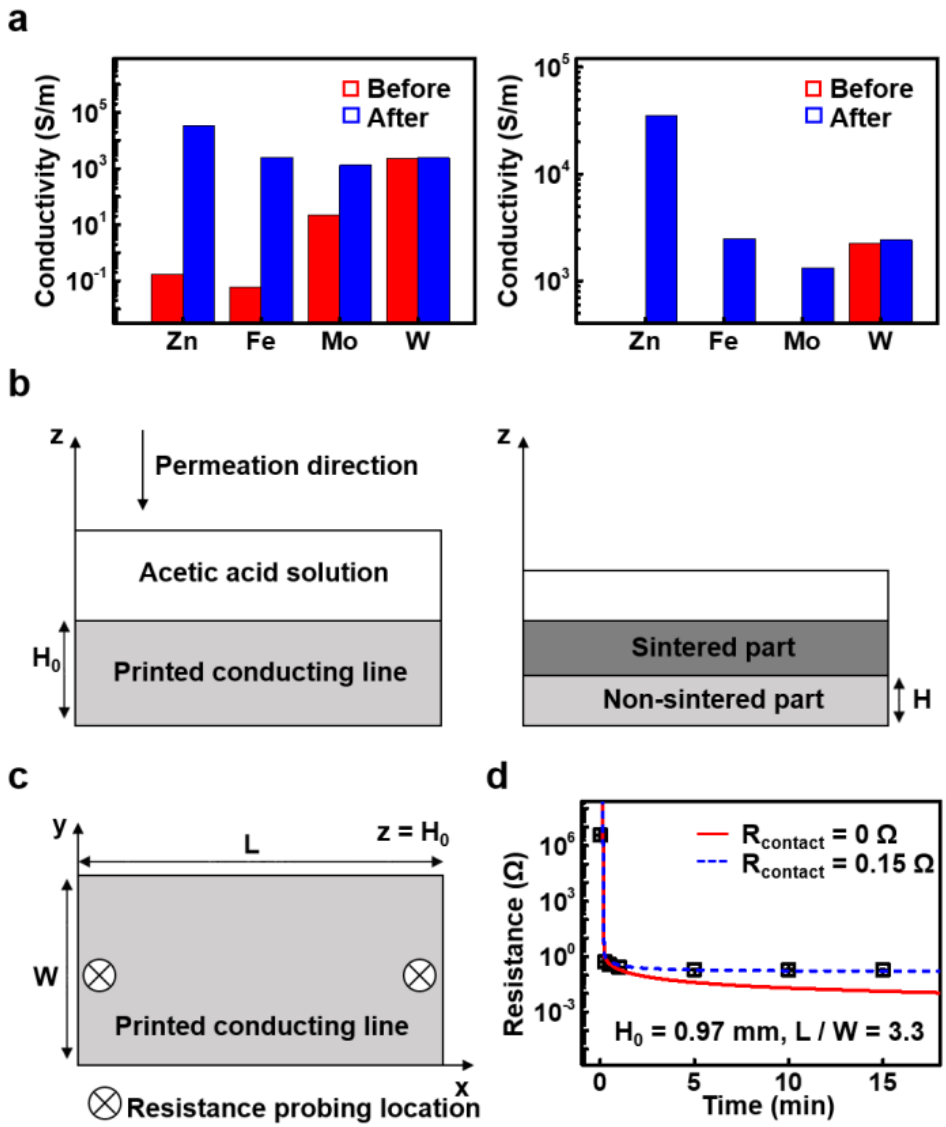

Figure 4. Acetic acid treatment effects and modeling of room-temperature sintering kinetics. (a) Conductivity change of various biodegradable metals with acetic acid treatment (b,c) Schematic illustration of reactive diffusion of acetic acid through printed conducting line (d) Reactive diffusion based modeling with experimental data of Zn-PCL ink.

2.3.1.1.2. Room-temperature grafting

For the semiconducting ink, we initially focused our research on biodegradable metal oxide, specifically ZnO. However, we observed minimal changes in conductivity with increasing volume fraction of fillers. Motivated by the idea of achieving a relay of wurtzite structure through sintering between Zn and Zn, forming connections between the fillers as Zn-Zn connections, we attempted previous sintering approach. However, the dissolving effect on ZnO resulted in the formation of Zn nanoparticles, which was confirmed through EDS analysis. Moreover, we found that this approach did not significantly alter the resistance. Then $Zn(Ac)_2$ in solution was considered for direct reduction. However, this presented challenges as the reduction process needed to be conducted in an aqueous environment and selectively targeted the ZnO component, interacting unfavorably with the native oxide on the Zn-based conductor surface, which is not favorable post-treatment for electronic components.

Therefore, we explored an indirect approach by blending conjugated molecules with metal oxides, as reported in the literature to enhance conductivity under high-pressure conditions. The conductivity of the ZnO ink was approximately 10^{-5} S/m, showing little dependence on the volume fraction. In the following section, for the optimization of rheological properties suitable for 3D printing, a ratio of humectant, binder, and solvent was considered. Although high-pressure couldn't be applied to ink, to achieve maximum filler condensation within the optimized matrix, a high volume fraction of ZnO (approximately 35%) was used. The humectant accounted for 50%, while the binder was around 13-15%. It was observed through cross-sectional SEM images of the printed ZnO ink and EDS analysis that the humectant formed its own miscelle structure, aiding in the aggregation of ZnO particles. In this situation, the addition of conjugated molecules was expected to provide an enhancing effect through grafting between ZnO surfaces,

although it may not reach the conductivity level of pure ZnO. In addition, intrinsic conductivity of a ZnO film with a thickness of approximately 460 nm is known to be around 674 S/m while our ZnO filler has diameter of ~500 nm[111].

Here, conjugated molecules significantly increased inter-granular conductivity by reducing the total potential barrier of the interphase between ZnO fillers. A suitable conjugated molecule is required to reduce the surface dipole of ZnO and align the HOMO level of conjugated molecule with Fermi-level of ZnO, known as Fermi-pinning. Biocompatible conjugated molecules, 2% volume fraction of BY and IND, enhanced the ZnO ink's conductivity 31.8 times and 2.87 times that of pure one. Interpretation of the phenomena is as followed.

For n-type semiconductor, electron at Fermi level tends to leak out to vacuum level and induces higher work function at particle surface (W_S) than bulk work function (W_B). In case of Ws higher than ionization energy of conjugated molecule, there is chance to transfer electron from conjugated molecule to N type semiconductor. Due to high surface dipole at N type semiconductor surface, conjugated molecule have physisorption interaction with it. When semiconducting nanoparticle and conjugated molecule get closer, orbitals leaked out from interior part of semiconductor pushes back inside and surface dipole get smaller and at some distance, HOMO level of conjugated molecule pinned to Fermi level of semiconductor. And conjugated molecule's band gap becomes potential barrier of electron conduction in semiconducting inks, which was verified with our case using Tauc plot obtained from UV-VIS that enhancement effects of conjugated molecule was Brilliant yellow (~32 times) > Indigo (~3 times) > Guanine (~1.1 times) while main direct band gap was Brilliant yellow (~2.66 eV) < Indigo (~3.59 eV). Although minor direct band gap of indigo has 1.67 eV, indigo assists less electron transfer than brilliant yellow for following hypothesized reasons. Molecular weight of brilliant

yellow is larger than indigo with high aspect ratio which can provide more intramolecular conductive networks (M(indigo) = 262.26 g/ml < M(brilliant yellow) 624.55 g/ml) while reducing intermolecular networks to reach intergranular distances.

Based on the previous study, we decided to explore p-type semiconductors and utilized boron-doped silicon, known for its degradability. In the case of n-type semiconductors, the surface charge was polarized negatively, inducing the physisorption of conjugated molecules. For p-type semiconductors, we expected surface polarization with a positive charge, leading to both physisorption of conjugated molecules and charge transfer, along with the occurrence of Fermi pinning. Experimental results indeed confirmed that it exhibited enhancement effects similar to ZnO.

However, two additional concerns arose. First, we questioned whether the conductivity was solely due to the percolation of conjugated molecules. Second, we investigated whether the significant increase in brilliant yellow was caused by the dissociation of Na^+ within the chemical structure. However, through experiments, we determined that increasing the volume fraction of conjugated molecules from 2% to 10% did not further increase the electrical conductivity, indicating that they only played a role in grafting. Additionally, when vacuum-dried under room temperature after complete drying of the ZnO ink containing brilliant yellow, there was no significant change observed in the I-V curve

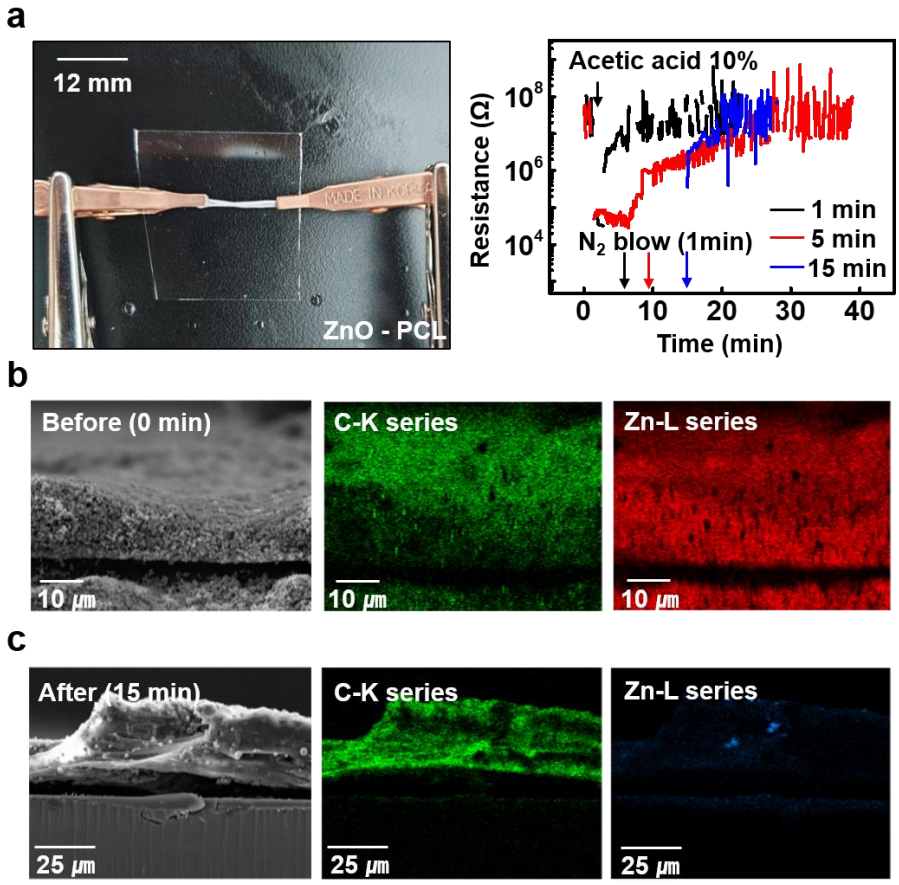

Figure 5. Acetic acid treatment effects on ZnO-PCL ink (a) Resistance change after acetic acid treatment (b) SEM, EDS image of ZnO before treatment (c) SEM, EDS image of ZnO after 15 min treatement

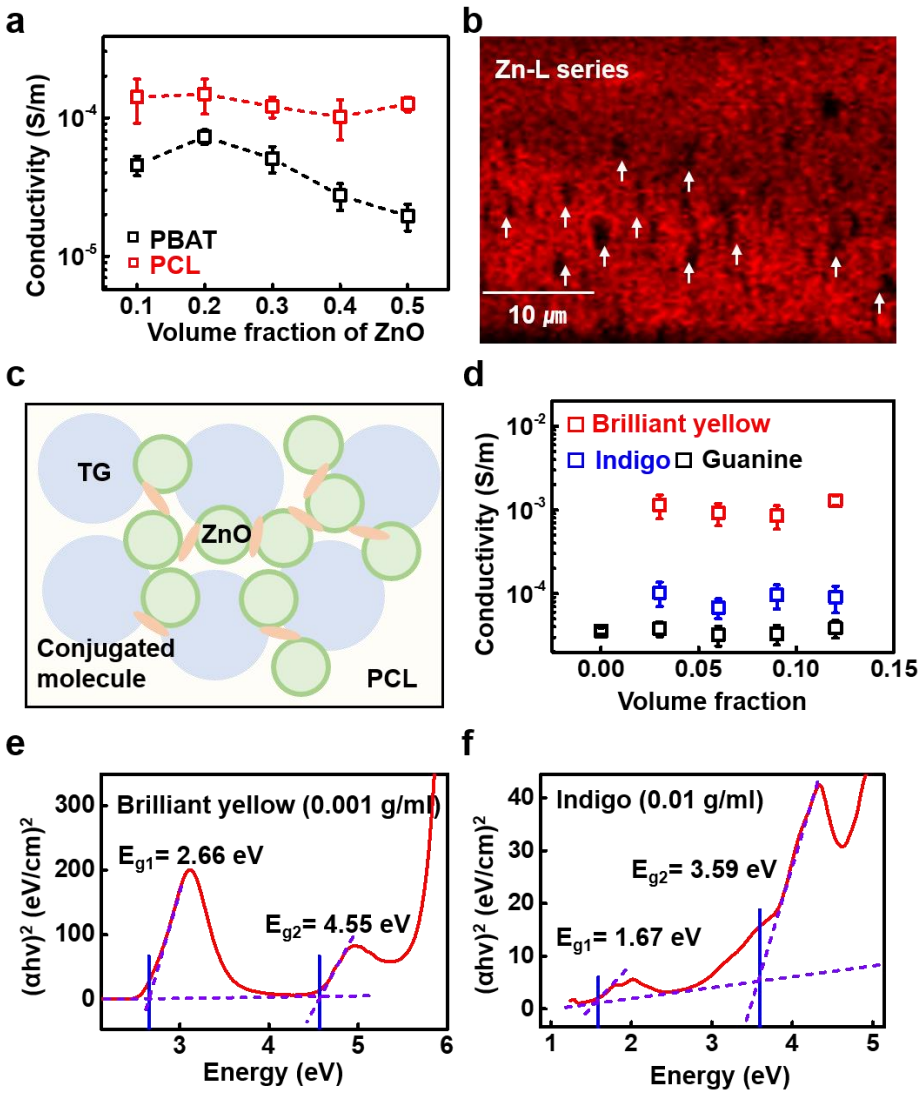

Figure 6. Conjugated molecule effects on ZnO-PCL ink (a) Conductivity change of ZnO in PCL or PBAT/TG ink (b) EDS image of Zn at cross sectional area of printed ZnO-PCL ink (c) Illustration of mechanism for ZnO conductivity enhancement (d) Conductivity change of ZnO-PCL ink by volume fraction of conjugate molecule (e,f) Tauc Plot for Direct band gap of brilliant yellow and indigo

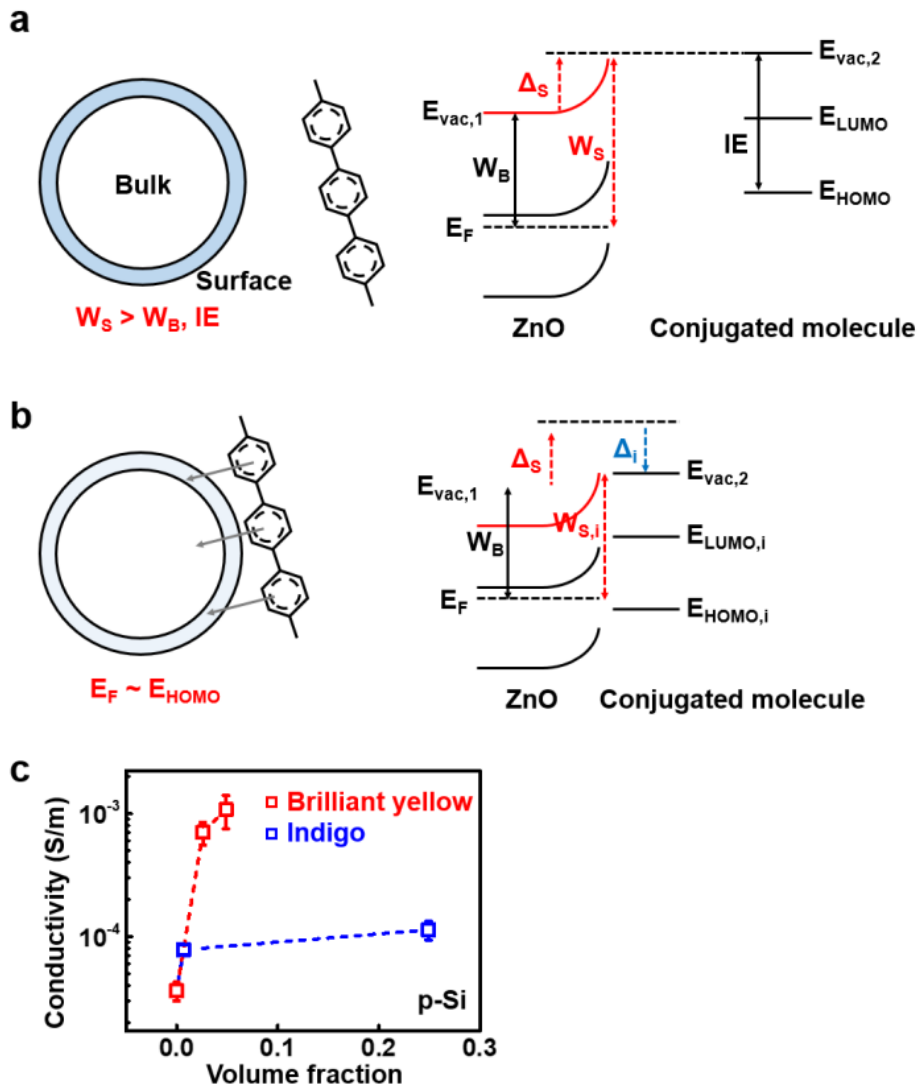

Figure 7. Mechanism of Fermi pinning of conjugate molecule to ZnO (a) Polarization (b) Physisorption with charge transfer (c) Conductivity change of p−Si with conjugated molecule

2.3.1.2. Dielectric properties of inks

Dielectric ink was available by blending the biodegradable oxides or nitride nanoparticles in polymeric matrix such as Si_3N_4 (50 nm) in PCL matrix. A small volume fraction increase of dielectric nanoparticles Si_3N_4 enhanced the DC capacitance of nanocomposite film. Regarding the phenomenon observed, there is a study on nanodielectrics, and the details are as follows. Since the interface of dielectric filler acts a dielectric properties enhancer, based on interphase power law model (IPL), nanodielectric phenomena can be modeled[112-115]. Considering interphase interaction, shape and orientation of filler, and air voids in predicting the dielectric constant of a composite material is

$$\epsilon_c^{\beta} = \varphi_f \epsilon_f^{\beta} + \varphi_i \epsilon_i^{\beta} + (1 - \varphi_f - \varphi_i)\epsilon_b^{\beta} \quad (Equation\ 1)$$

Where ϵ_c, ϵ_f, ϵ_i, ϵ_b are the dielectric constants of nanocomposite, filler, interphase, binder, respectively. φ_f and φ_i is volume fraction of fillers and interphase in nanocomposite. β is filler geometrical factor, in this case 1/3 (spherical). The interphase volume fraction (φi) depends on the filler volume fraction and an interphase volume constant (k) and can be calculated by Eqn. 2. K is related to filler-binder interaction affected by surface energy at the interface of bulk and surface of materials originates from chemical interaction and physical orientation of particles.

$$\varphi_i = k\varphi_f \frac{(1 - \varphi_f)}{1 + k\varphi_f} \quad (Equation\ 2)$$

Since the air voids in the interphase region in the nanocomposite can be neglected as compared to nanofillers so that the interphase dielectric constant can be assumed to be function of matrix and filler dielectric constants.

$$\epsilon_i^\beta = \epsilon_b^\beta + \varphi_f(\epsilon_f^\beta - \epsilon_b^\beta) \quad (\textit{Equation 3})$$

Combining Eqn (1), (2), (3), with k measured from experimental data and we can model dielectric constant of nanocomposite as followed Eqn (4) :

$$\epsilon_c^\beta = (\epsilon_f^\beta - \epsilon_b^\beta)(\varphi_f + 1 - \frac{1+\varphi_f^2}{1+k\varphi_f}) + \epsilon_b^\beta \quad (\textit{Equation 4})$$

By modeling interphase volume fraction and dielectric constant, we could observe large k (~25) which implies that due to DC current measurement with DMM interphase volume fraction is maximized at each filler volume fraction resulting 10 times higher than filler volume fraction. Also pores or air bubble generated by solvent vaporization should be adjusted to fit experimental data while interphase power law model neglects air gap inside composites. However, the nanocomposite has dielectric loss in high frequency range. So we verified with 3D printed Si_3N_4–PCL infill based capacitor within 1 – 100 kHz frequency using LCR meter with two different capacitor type, 1 unit interdigitated (I) and parallel plated (P). Structural difference of capacitor affected in low, high frequency range where interdigitated capacitor secure larger capacitance than parallel capacitor in low, high frequency range (@ 1 kHz, 64.43 pF (I) > 56.62 pF(P), @ 100 kHz, 11.16 pF (I) > 10.62 pF (P)).

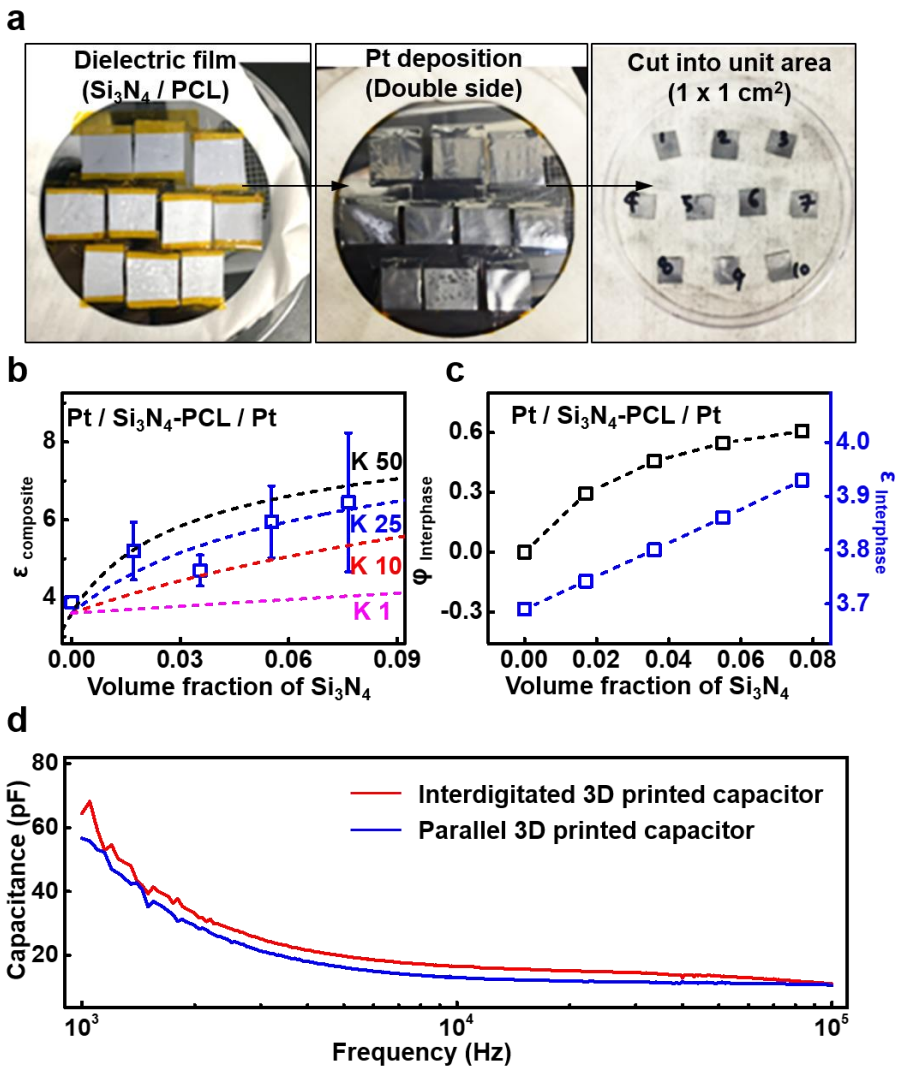

Figure 8. Characterization of dielectric ink (a) Thin film electrode fabrication for dielectrics measurement (b) Measured DC dielectric constant change by volume fraction change of Si_3N_4 in PCL matrix (c) Calculated dielectric constant and volume fraction of interphase by volume fraction change of Si_3N_4. (c) Measured AC capacitance by frequency change

2.3.2. Rheological properties of inks

In order to develop an ink suitable for 3D printing while maintaining optimized electrical properties, it was necessary to reduce the yield shear stress of the composite ink caused by friction during the interaction between the filler and the binder matrix, as well as to address the issue of stacking due to volume shrinkage resulting from solvent vaporization. To solve these two issues, a bioabsorbable humectant, such as tetraglycol (TG) or glycofurol, was introduced. TG is known to be bioabsorbable to the extent that it is used as a parental solvent for intravascular injection[116].

Another consideration was to make it compatible with commercially available bioprinters, which require printing within a relatively low dispensing pressure range (<200 kPa). Therefore, a strategy was needed to ensure that the ink could be printed under such conditions. The use of solvents with very low vapor pressure was necessary, so that they quickly evaporated as soon as they exited the nozzle. Additionally, the solvents needed to be relatively biocompatible and capable of dissolving biodegradable polymers. Therefore, tetrahydrofuran and chloroform were used. It should be noted that chloroform is known to be toxic, but in this case, complete drying was conducted under vacuum after printing.

Three factors had a significant impact on the rheological properties: the humectant, the volume fraction of the filler, and the particle size.

2.3.2.1. Humectant

Although it is helpful for reducing yield shear stress of inks and improve volume shrinkage after printing, excessive humectant lowers storage modulus after printing which fails stacking of inks. Therefore, appropriate humectant/solvent ratio is important. Based

on the determined filler-to-binder ratio that can exhibit electrical properties and the ratio of binder to solvent within a range that can exhibit the film formation based on solvent casting, different ratios of humectant to solvent were used. Continuous storage modulus measurements were conducted as solvents evaporated between two flat plates. In our case, measuring storage modulus at angular frequency 10 rad/s, shear strain 1 %, with certain filler volume fraction, over 10^4 Pa was possible to stack. Therefore, ratio of TG and binder/solvent was determined as near 1:2.

2.3.2.2. Volume fraction of fillers

Volume fraction of fillers in ink is defined as below. Volume fraction range for fillers were examined in range of securing electrical properties from pervious characterizations, while binder/solvent fraction was optimized to certain concentration for robust film formation by solvent casting.

$$\rho_{filler} = \frac{V_{filler}}{V_{filler} + V_{binder} + V_{humectant} + V_{solvent}} = \frac{\frac{M}{d}_{filler}}{\frac{M}{d}_{filler} + \frac{M}{d}_{binder} + V_{humectant} + V_{solvent}}$$

When the shear yield stress was measured based on the volume fraction of the filler within the range that allowed for electrical properties, using the fixed ratio between the humectant and the solvent, it was found that a range of approximately 30-150 Pa was achievable within the pressure range of 0-200 kPa of the printing system.

2.3.2.3. Filler size

Regarding filler size for printability, volume fraction needed for 3D printability securing range of electrical performances were less for smaller diameter particle. Since interaction between fillers and binder/solvent/humectant is affecting viscosity and shear yield

stress, it seemed log scale of diameter was proportional to volume fraction needed for printability by observation.

Under these extrusion conditions, it was possible to achieve a feature size of 0.4 mm. The printing parameters used were as follows: printing speed (1–5 mm/s), pressure (50–200 kPa), nozzle shape (22G conical, needle), nozzle height (0–0.4 mm), print head temperature (25–140℃), and bed temperature (4–35℃).

Furthermore, it was observed that by increasing the pressure to the range of 1000–3000 kPa and reducing the amount of solvent, even higher resolutions of as low as 0.05 mm – 0.1 mm could be achieved via inner diameter of 0.1 mm, 0.2 mm needle. 0.0727 mm (Fe_3O_4–PCL with 1379 kPa), 0.0833 mm (ZnO–PCL with 1379 kPa), 0.105 mm (Si_3N_4–PCL with 1379 kPa), 0.124 mm (Mo–PBAT with 1379 kPa), 0.143 mm (Zn–PCL with 2413 kPa)

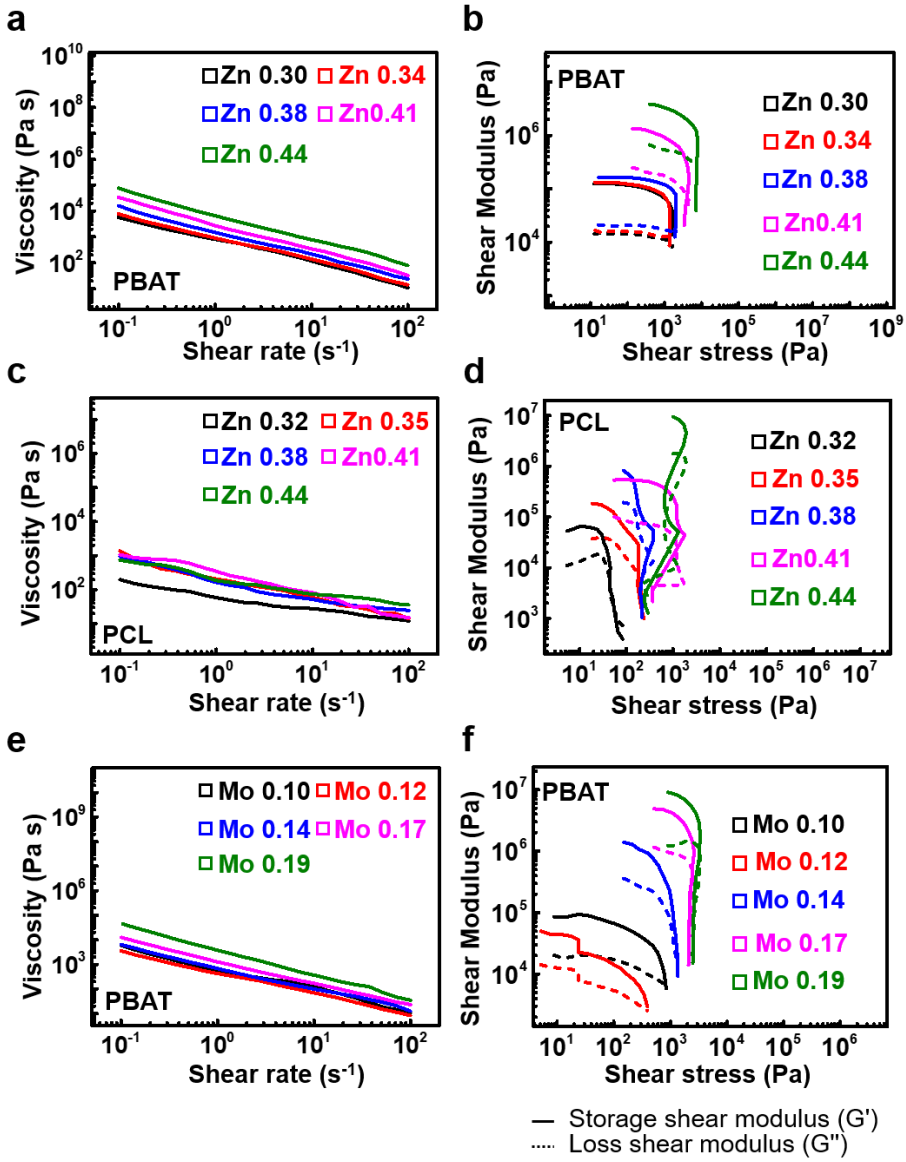

Figure 9. Rheological properties of conducting inks such as (a,b) Zn−PBAT ink, (c,d) Zn−PCL ink, (e,f) Mo−PBAT ink by various filler volume fraction

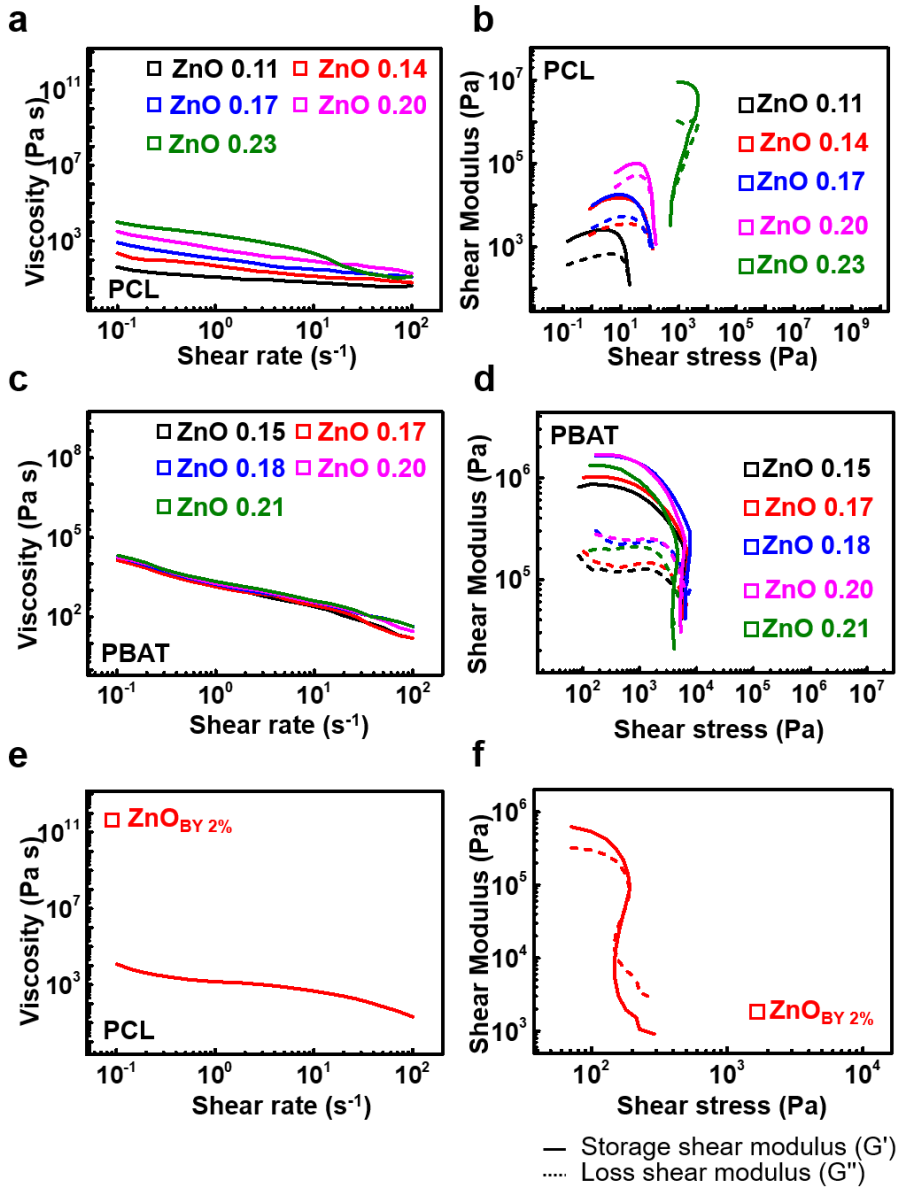

Figure 10. Rheological properties of semiconducting inks such as (a,b) ZnO–PCL ink, (c,d) ZnO–PBAT ink by various filler volume fraction, and (e,f) $ZnO_{BY2\%}$–PCL ink

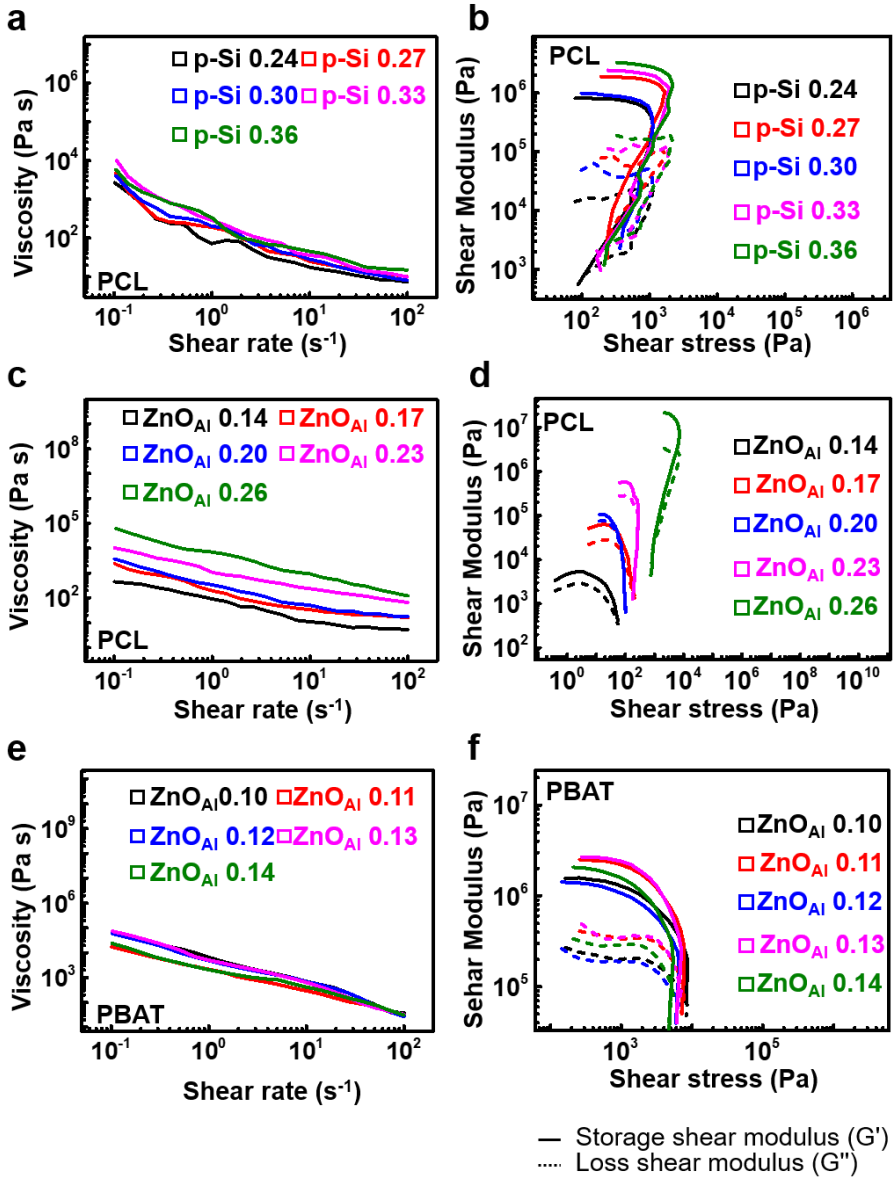

Figure 11. Rheological properties of semiconducting inks such as (a,b) p type Si–PCL ink, (c,d) ZnO_{Al}–PCL ink, (e,f) ZnO_{Al}–PBAT by various filler volume fraction.

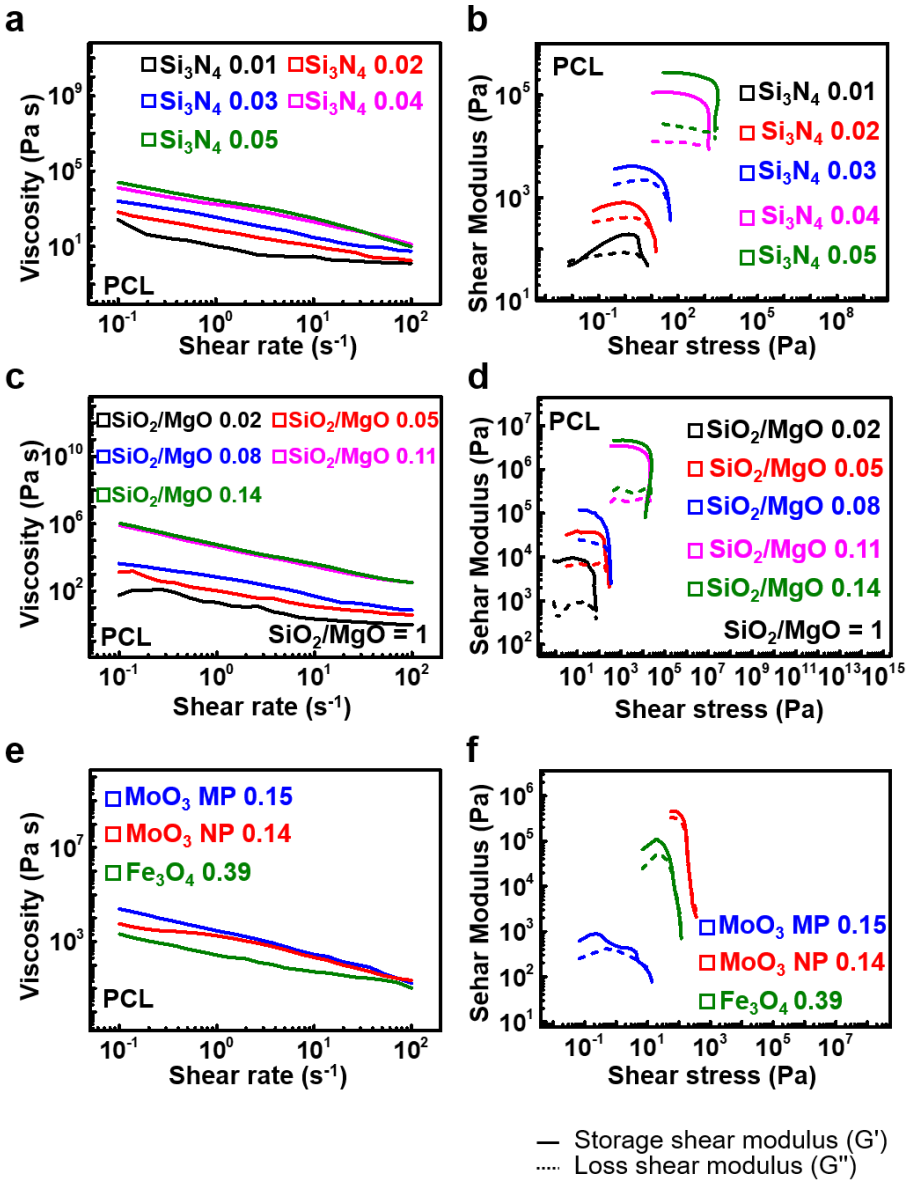

Figure 12. Rheological properties of dielectric / metal oxide inks such as (a,b) Si_3N_4–PCL ink, (c,d) SiO_2/MgO–PCL ink by various filler volume fraction and (e,f) MoO_3–PCL, Fe_3O_4–PCL ink.

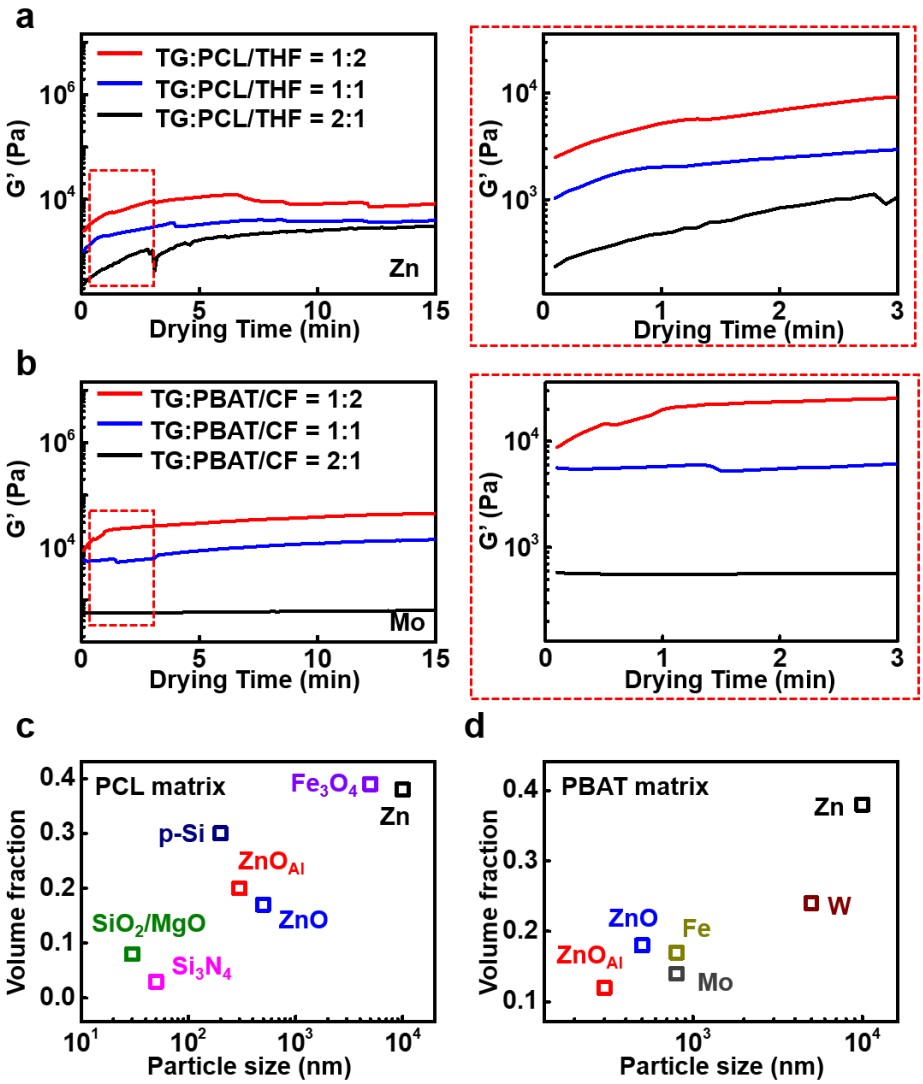

Figure 13. Effects of humectants and particle size on rheological properties (a) Shear storage modulus by drying time with various ratio between TG and THF (b) Shear storage modulus by drying time with various ratio between TG and CF (c,f) Apparent volume fraction optimal for extrusion and stacking of inks by different particle size in PCL or PBAT matrix.

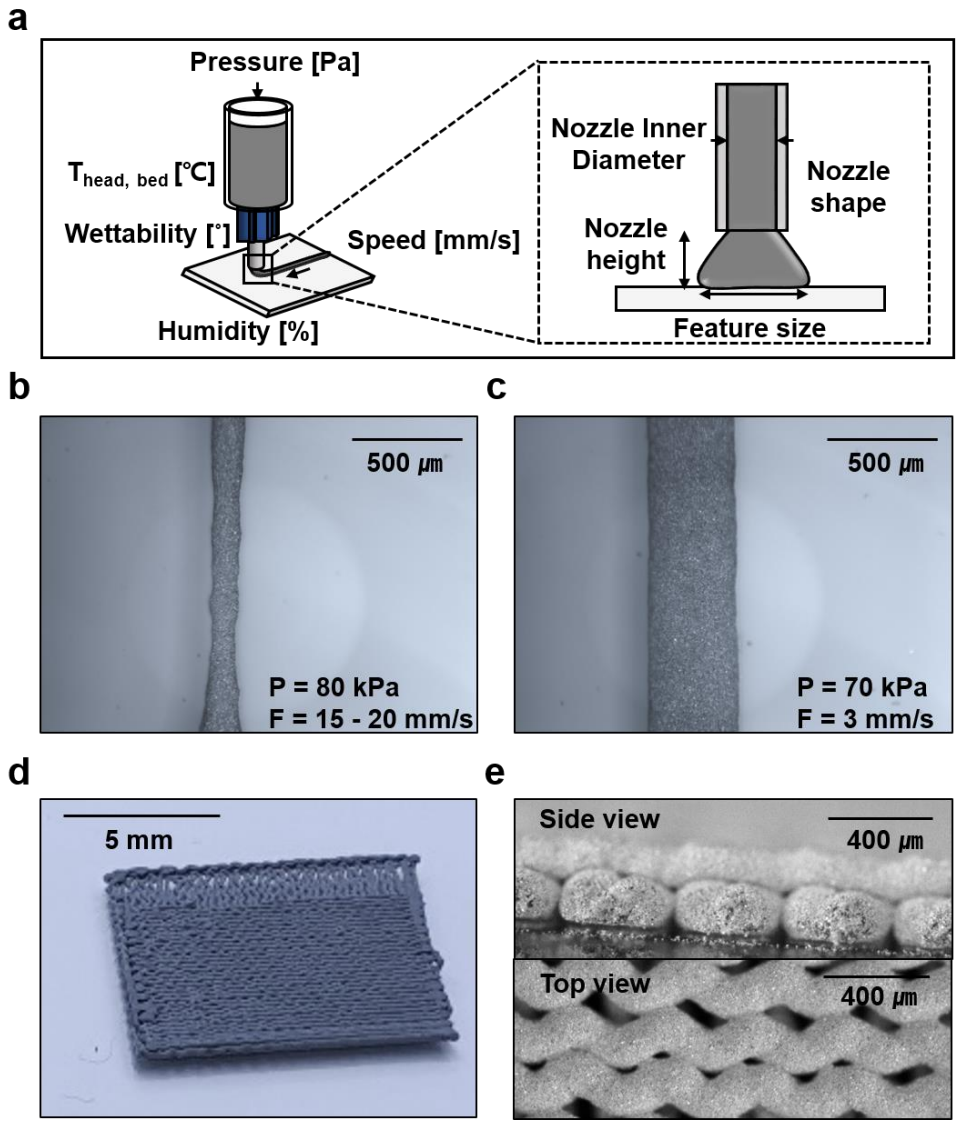

Figure 14. Printing representative conductive ink (Zn-PCL). (a) Printing parameters for affecting feature size of inks (b,c) Image of printed line in different pressure/speed. (d) Printed 1 cm x 1 cm film with 27 GA nozzle. (e) Side and top view for printed structure in (d)

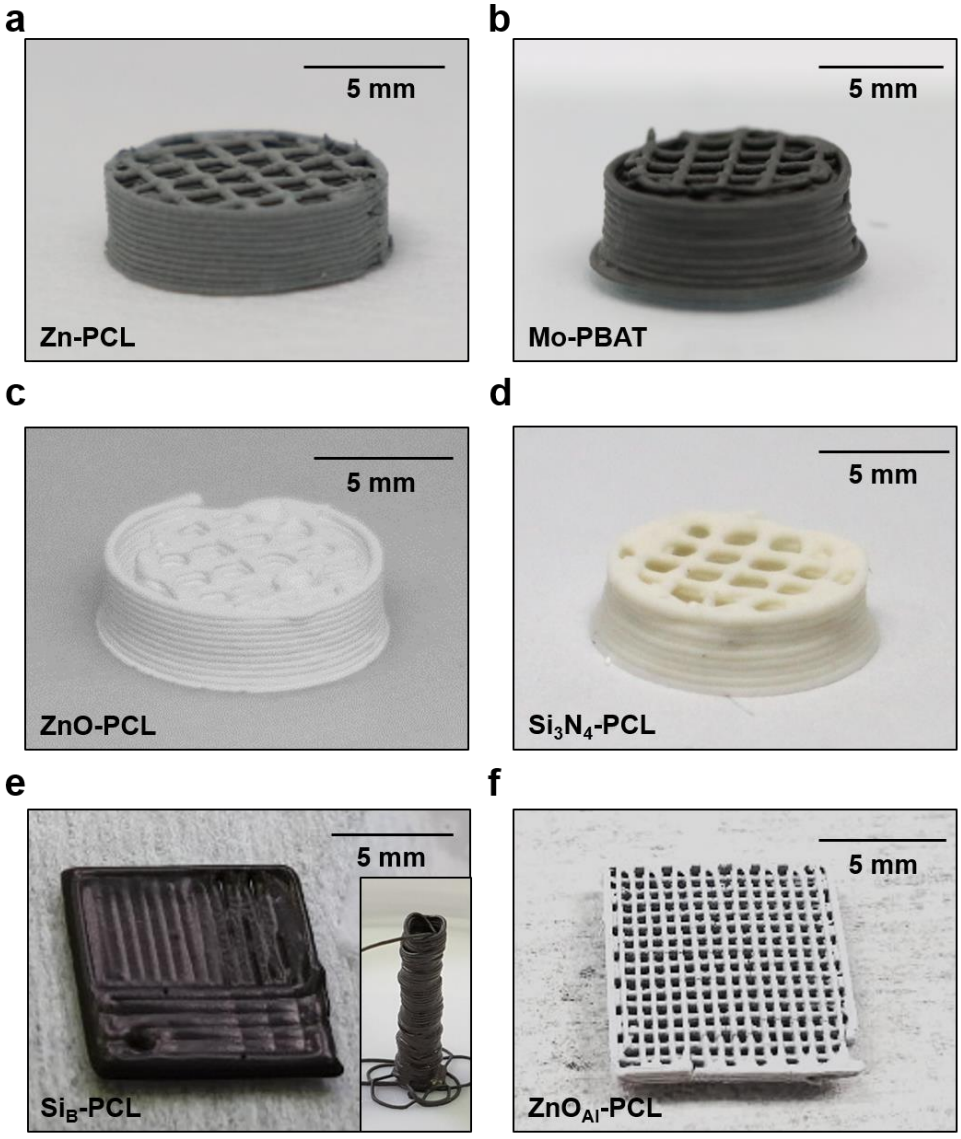

Figure 15. Printed scaffolds or box with various inks (a) Zn-PCL, (b) Mo-PBAT, (c) ZnO-PCL, (d) Si_3N_4-PCL, (e) p type Si-PCL, (f) ZnO_{Al}-PCL.

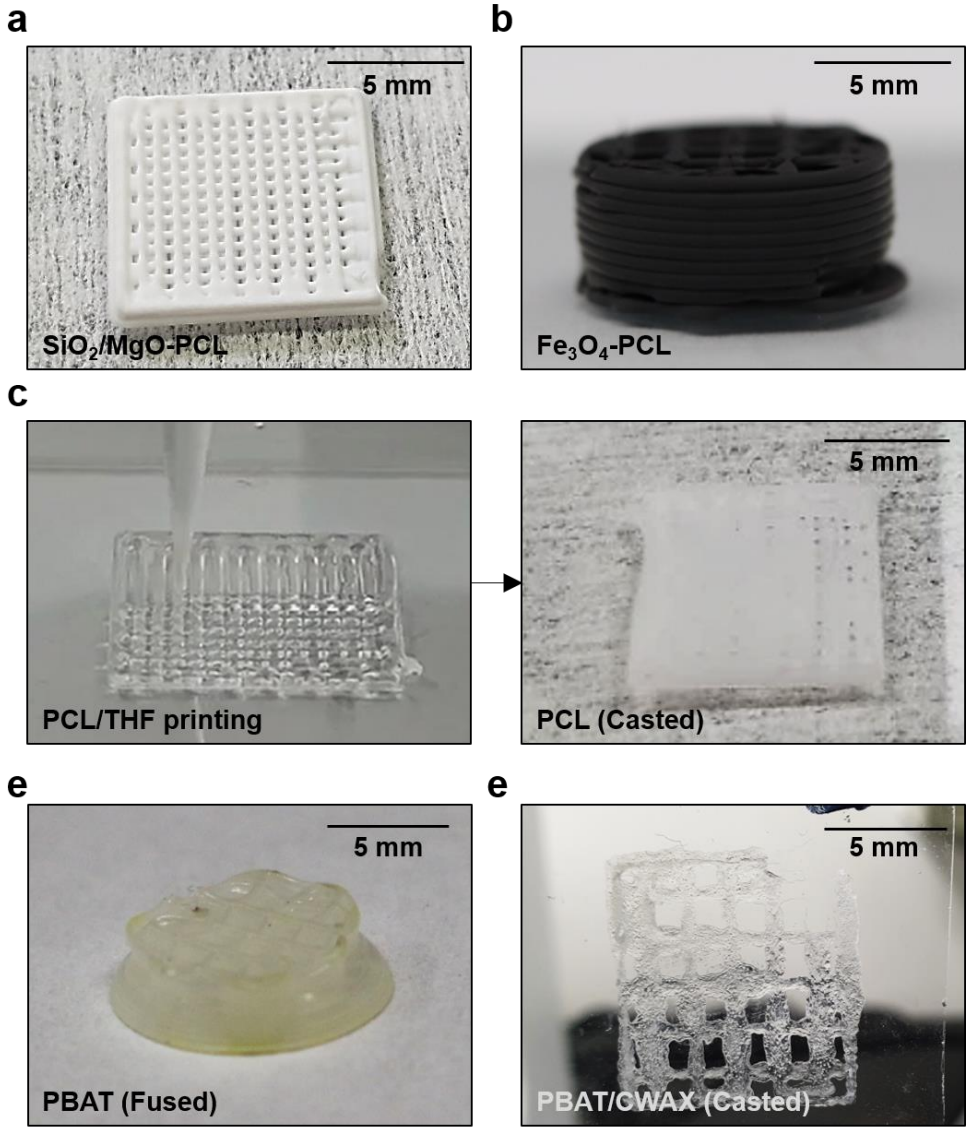

Figure 16. Printed scaffolds or box with various inks (a) SiO_2/MgO−PCL, (b) Fe_3O_4−PCL (c) PCL with solvent casted printing, (d) PBAT with pellet fused printing, (e) PBAT/CWAX with solvent casted printing.

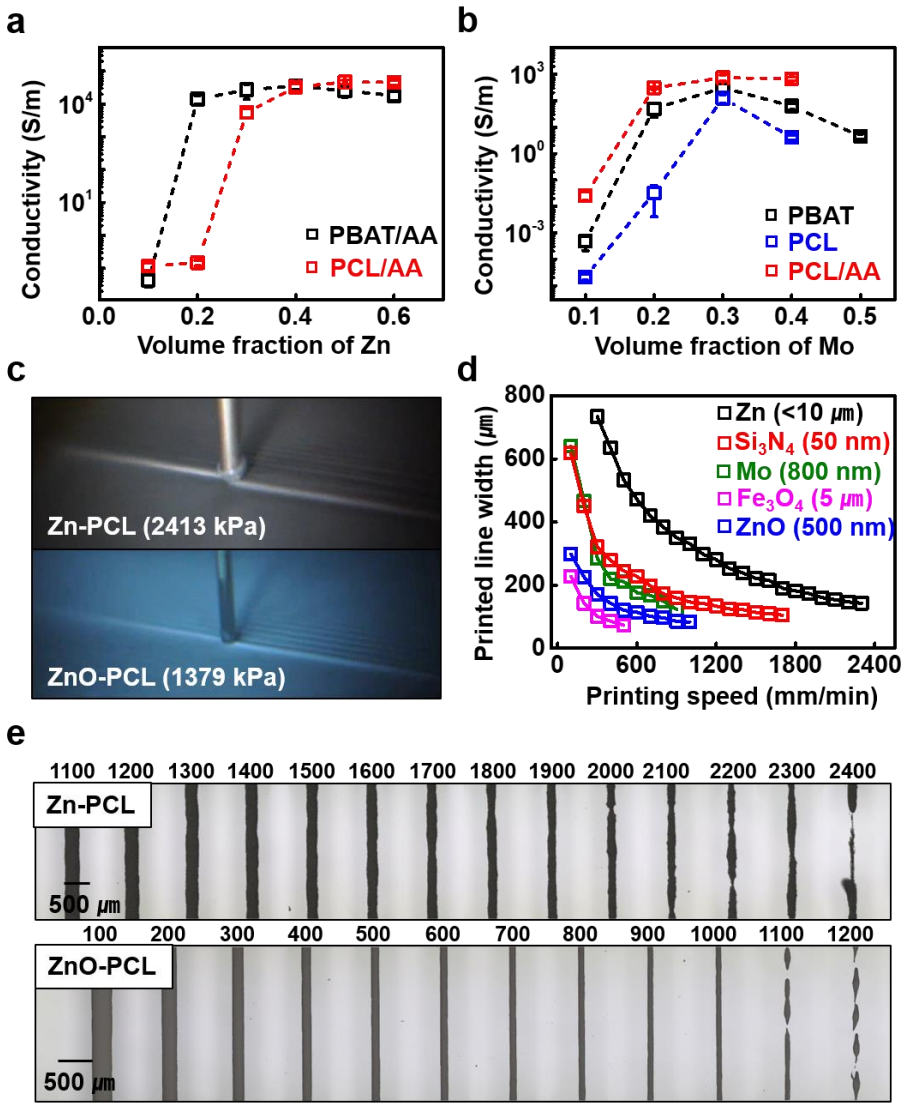

Figure 17. Verification of conductivity with humectants in inks and possibility for high resolution printing with biodegradable electronic inks. (a,b) Conductivity change of Zn or Mo based inks by volume fraction of fillers (Filler + binder + humectant + solvent). (c) Image of printing Zn, ZnO with high pressures (d) Change of printed width by printing speed with minimum pressure. (e) Feature size test for Zn−PCL, ZnO−PCL

2.3.3. Degradation properties of inks

The degradation of inks in a real biological environment was confirmed through SEM images. While the ink exhibited a dissolution property, indicating degradation, this paradoxically implies that the electrical properties also degrade within the body. Therefore, the presence of a biodegradable encapsulation layer is crucial in biodegradable electronics to protect water-soluble circuits from early dissolution and ensure stable operation over time. Candelean wax (CWAX), with linear hydrocarbon chains, provides an effective barrier against water permeation, but its mechanical properties (such as short flexural elongation of approximately 1%) are poor. To address this, blending CWAX with a relatively soft biodegradable polymer such as PBAT can create a robust encapsulant. It was possible to 3D print PBAT/CWAX encapsulant covering sintered Zn-PCL resistor traces on a glass substrate by controlling the polymer concentration and bed temperature (4℃). The resistance variation of encapsulated Zn-PCL traces, with different thicknesses of PBAT/CWAX and the relatively hydrophilic PBAT, during immersion in PBS at 37℃, was examined. The resistance of the Zn-PCL trace encapsulated with a PBAT monolayer (thickness of approximately 170 μm) initially reached double the resistance time (13 hours), while the PBAT/CWAX monolayer took approximately 46 hours. The bilayer of PBAT/CWAX further delayed the resistance doubling time to 150 hours.

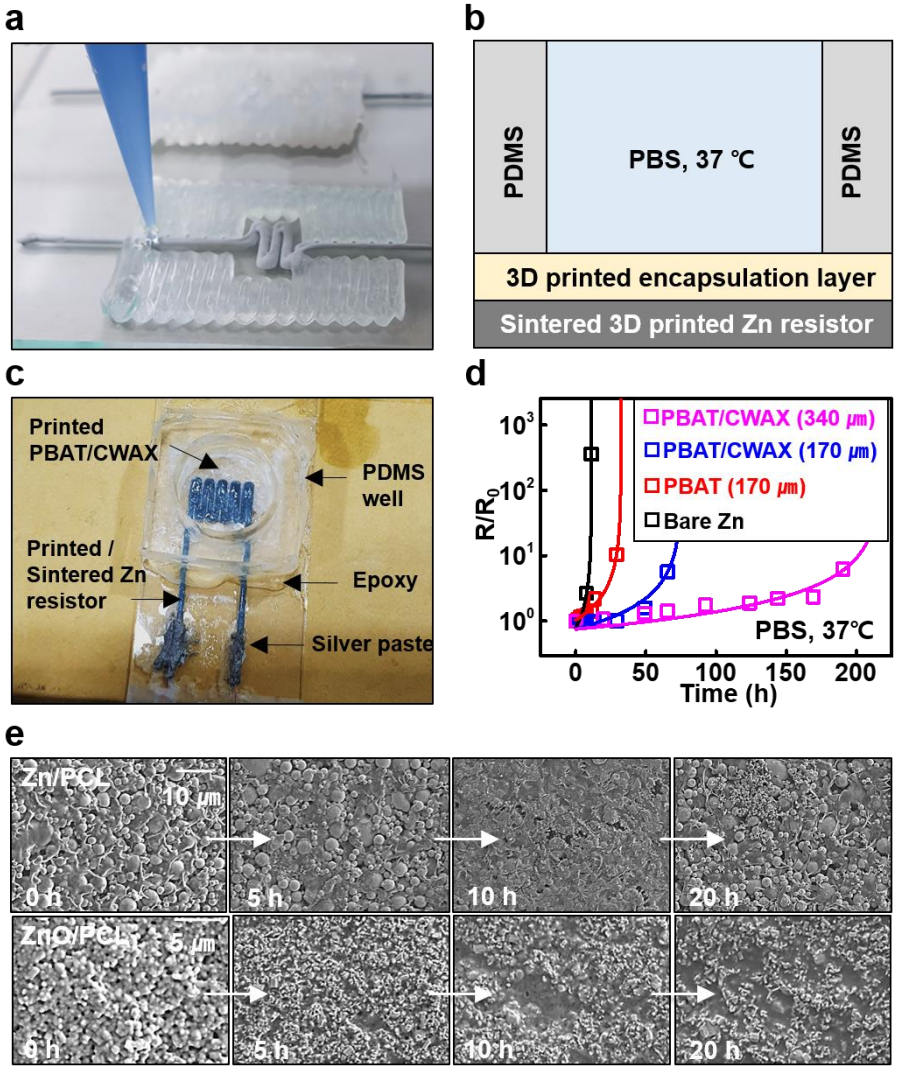

Figure 18. Degradation / Encapsulation properties of inks. (a) Printing process of encapsulation layer on sintered Zn printed resistor (b) Experimental set-up for examining encapsulation performance (c) Real image of the set-up (d) Resistance change of Zn resistor by time in PBS, 37℃ for various encapsulation layer. (e) Serial SEM images of surface morphology for Zn-PCL and ZnO-PCL immersed in PBS, 37℃ by time.

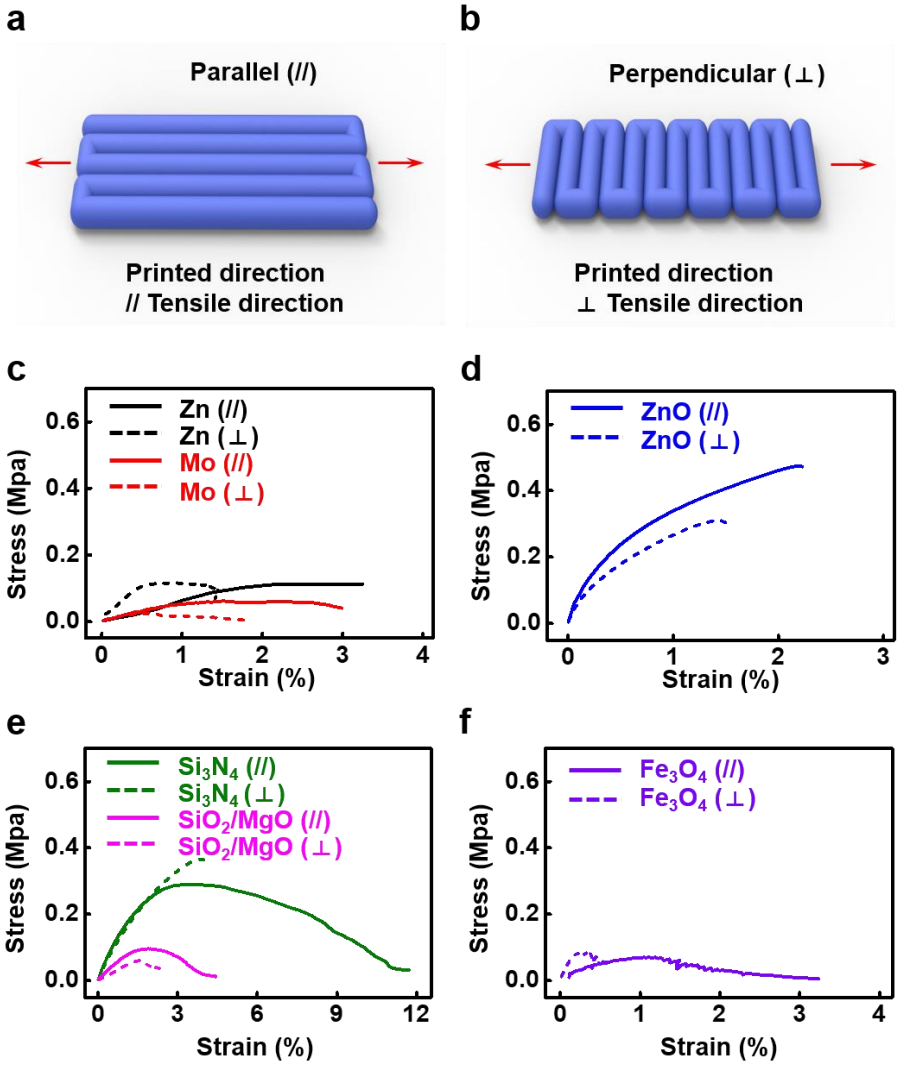

Figure 19. Mechanical properties of inks. (a,b) Schematics for illustrating symbols of printed direction and uniaxial tensile direction (c) Stress–strain (SS) curve of conducting ink (Zn–PCL, Mo–PBAT), (d) SS curve of semiconducting ink (ZnO–PCL), (e) SS curve of dielectric ink (Si_3N_4–PCL, SiO_2/MgO–PCL), (f) SS curve of magnetic ink (Fe_3O_4–PCL)

2.3.4. Mechanical properties of inks

Since composite forms were used, consisting of metal and ceramic-based inorganic fillers with a polymer having a modulus of a few MPa, the elongation of Zn-PCL, Mo-PBAT, ZnO-PCL, Si_3N_4-PCL, SiO_2/MgO-PCL, and Fe_3O_4-PCL was very short, ranging from 2% to 12% and the modulus ranged from 5 MPa to 10 MPa. One interesting observation was that the elongation varied depending on the printing direction relative to the uniaxial tensile direction, with a tendency for shorter elongation when they were parallel. This can be attributed to the rectilinear pattern used in printing, where the lines on the side tended to protrude slightly and create larger notches compared to the parallel direction, resulting in less uniformity. Therefore, careful consideration of these factors was necessary for precise design.

2.3.5. Multi-material printing rule

To fabricate electronic devices based on the optimized inks, designing rules need to be established for multi-material printing. Optimization was carried out for each material considering the following factors. For calibration, a long-distance focal microscope was used to ensure that all nozzles connected to the print heads could be aligned to a single position just before printing.

2.3.5.1. XY line gap

When coding the print path for printing, it may appear as a solid line. However, in actual printing, it is typically printed with a diameter approximately equal to the inner diameter of the nozzle. We required repetitive printing feature sizes, and in our case, it needed to be around 0.4 mm. This means that a minimum distance of 0.4 mm between two lines was necessary.

2.3.5.2. Z interconnection / periodicity

In the process of connecting in the Z-axis, our printing system lacked the ability to rotate the print bed or print head for 5-axis actuation. Therefore, a stacking method was employed. Even when stacking coils, it was not feasible to stack them in a one-voxel per layer manner. Instead, a fragment-based approach was adopted to achieve interconnection. When stacking fragments, if the G-code for each layer followed a circular or polygonal shape ($n \geq 5$), it would result in a complex structure. To simplify the process, we initially aimed to set a unit layer shape in a square form with $n = 4$, allowing for a simpler stacking pattern.

2.3.5.3. Z line gap

Since the ink we used had a low viscosity and quickly solidified, there were instances where slight flow occurred even during stacking. As a result, in the case of conductors, there were situations where the space between two lines should have been completely blocked but couldn't be achieved. Therefore, it was necessary to adjust the line gap. In our case, we found that a gap of approximately two layers provided sufficient insulation.

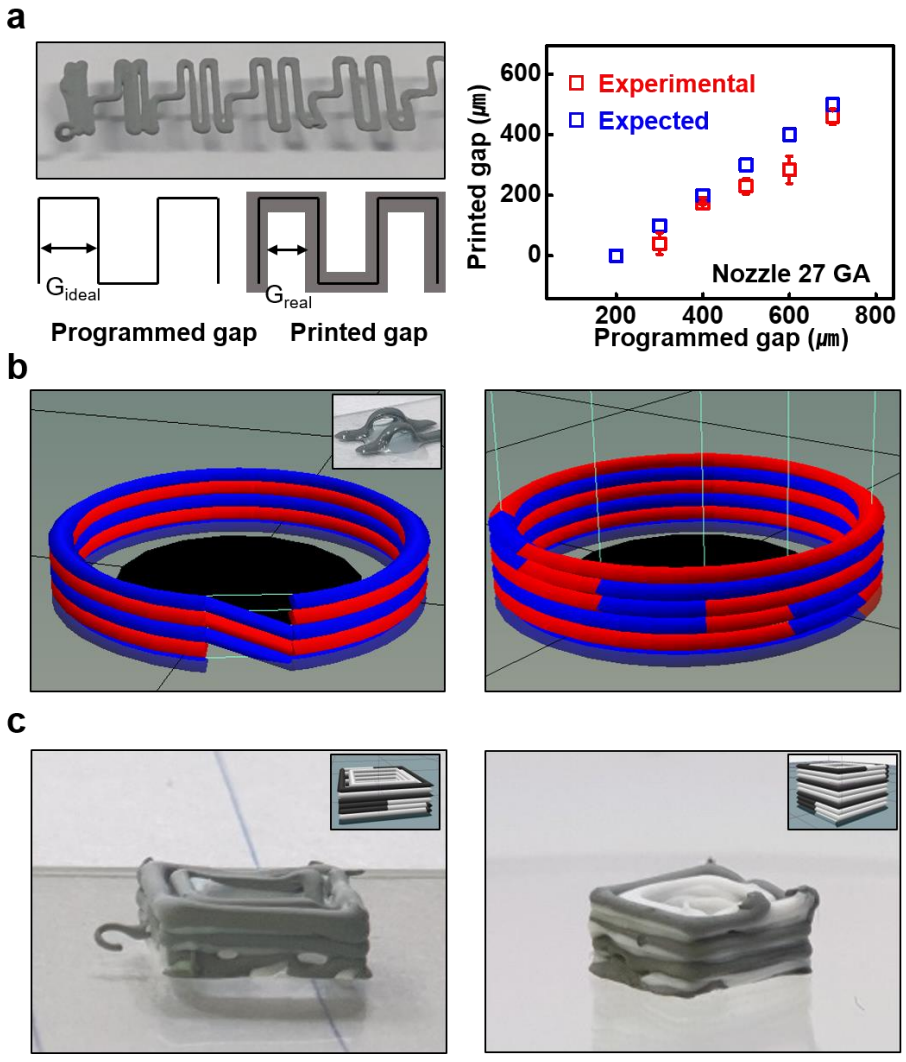

Figure 20. Design rule of printing in XYZ coordinate space. (a) Correlating printed gap and programmed gap for each inks (b) Z-interconnections via voxels or fragments. Inset shows the possibility of printing non-supported structure. (c) Z line gaps for conductors confinements.

2.3.6. Junctions between inks

To enable the functionality of printable electronic inks, passive components can be created in a 3D space using conductor, dielectric, and frame material as the basic elements. This allows the fabrication of resistors, capacitors, and inductors. In this case, there is no singularity regarding the choice of conductor element.

However, for active components, when arranging conductor, dielectric, semiconductor, and frame material as the basic elements, there are singularities at the conductor–semiconductor and semiconductor–semiconductor junctions. Junctions can be broadly categorized into three types: ohmic junction, Schottky junction, and PN junction.

2.3.6.1. Conducting inks – Semiconducting inks

The junctions that occur in this case are defined by the work function of the metal filler in the conductor ink and the electronegativity of the semiconductor. To determine this, it is necessary to know the work function of the conductor ink's surface and the electronegativity of the semiconductor ink's surface. The work function of the conductor is measured by the potential difference with the work function of a HOPG tip in a Kelvin probe. Mapping was conducted for a small area, and the average value was obtained. The measured work functions for each conductor surface were 3.83 eV for Fe, 3.49 eV for Zn, 4.47 eV for Mo, and 4.44 eV for W.

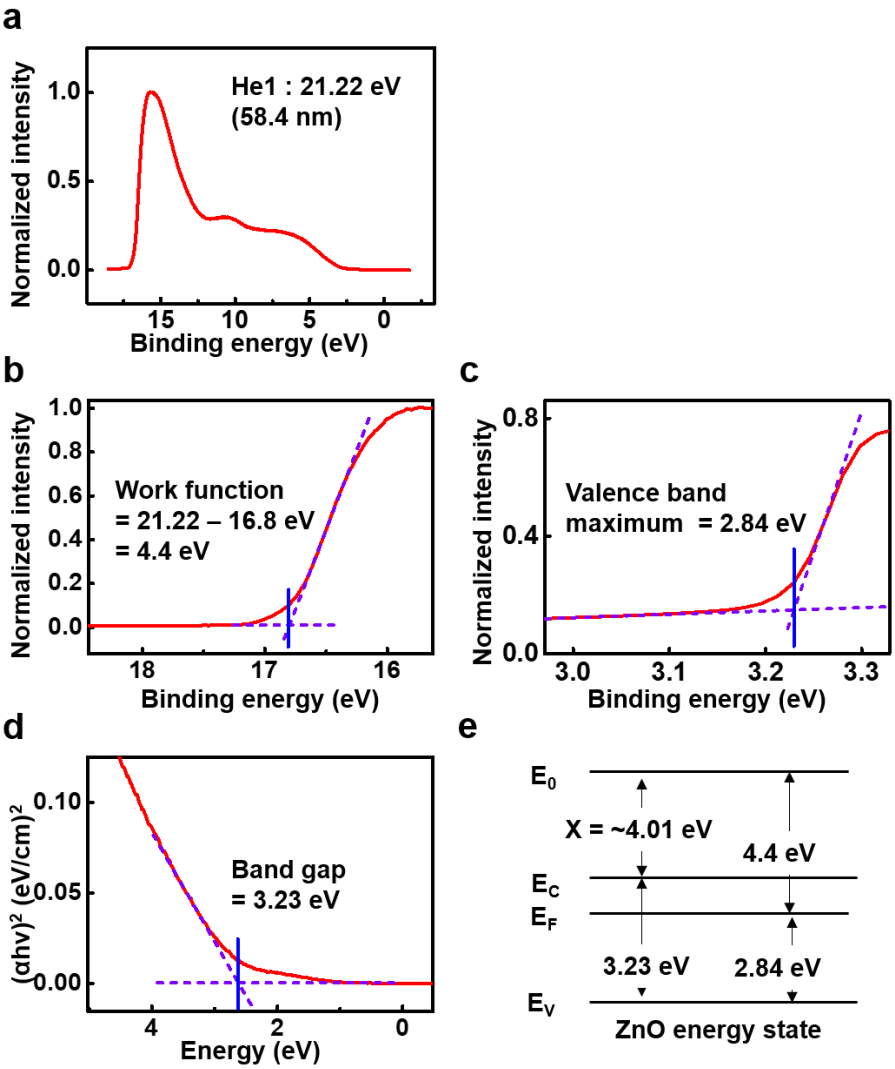

Figure 21. Measurements of ZnO energy state. (a) UPS data for ZnO in terms of binding energy. (b) Work function and (c) Valence band maximum estimation from UPS data (d) Direct band gap estimation from Tauc plot (e) Estimated energy state of the ZnO.

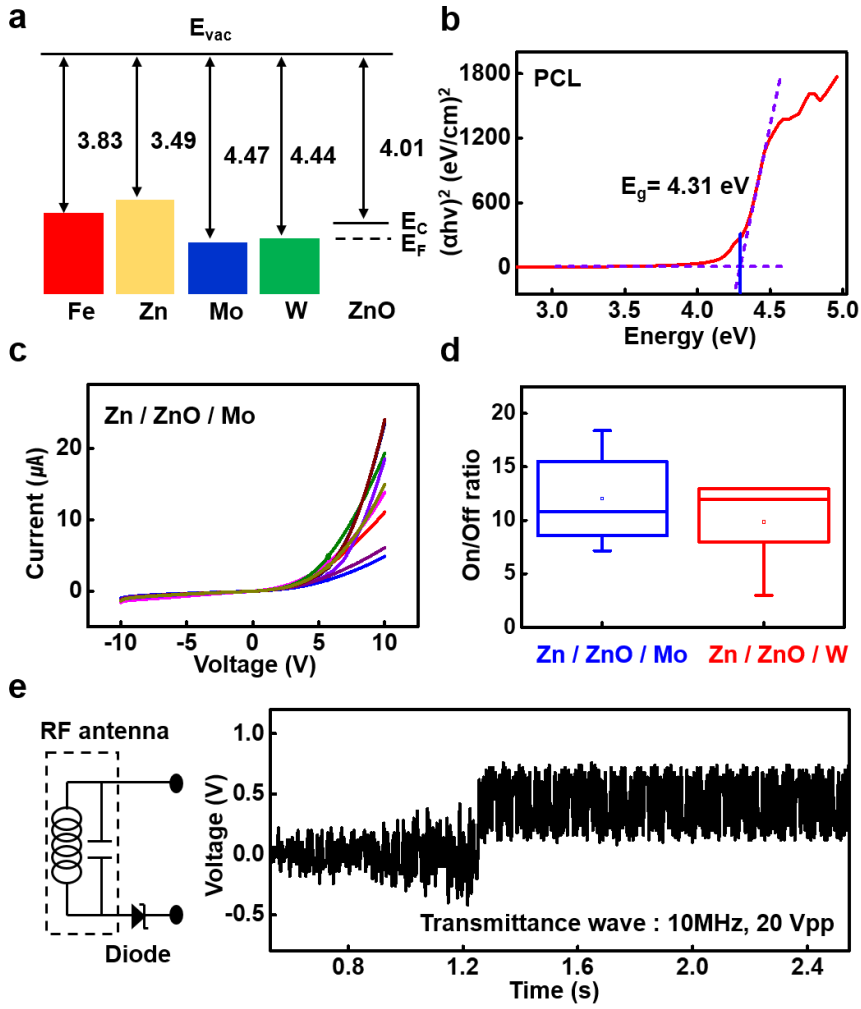

Figure 22. Conducting inks and semiconducting inks junctions (a) Estimated energy state of Fe, Zn, Mo, W, ZnO (b) Tauc plot of PCL (c) IV curve of Zn / ZnO / Mo with asymmetric junctions : Zn−ZnO for Ohmic, Mo−ZnO for Schottky. (d) On−Off ratio of Zn / ZnO / Mo and Zn / ZnO / W for 10 samples. (e) Output voltage of wirelessly powered device with wireless antenna with Zn / ZnO_{BY} / Mo.

For the semiconductor, the electronegativity was determined by measuring the work function and the difference between the valence band and Fermi level (valence band maximum), as well as the direct band gap, using UPS and UV/VIS techniques. As a result, it was found that ZnO had an electronegativity of approximately 4.01 eV. Based on the difference between the work function of the conductor and the electronegativity of ZnO, it was determined that Fe and Zn would form ohmic junctions, while Mo and W would have Schottky barriers of approximately 0.47 eV and 0.44 eV, respectively. Subsequently, the performance of four diodes, Zn/ZnO/Mo, Zn/ZnO/W, Fe/ZnO/Mo, and Fe/ZnO/W, was compared. Among them, Zn/ZnO/Mo exhibited reproducibility (n = 10) and a relatively high on/off ratio (~12). It was also confirmed that the same rectification occurred when brilliant yellow was mixed with the ZnO ink.

When examining the microscale situation of how each interface can occur, there can be two cases: (1) ZnO : conjugated molecule : conductor or (2) ZnO : conjugated molecule : binder : conductor. In the case of (1), Fermi alignment and the resulting Schottky barrier formation occur through the conjugated molecule. Additionally, the difference between the conjugated molecule's LUMO and ZnO's conduction band must be taken into account. In the case of (2), the interfacial layer formed by the binder requires consideration of the electron's tunneling effect. In such cases, an apparent Schottky barrier needs to be adjusted, and it can be expressed using the following equation [117-119]:

$$J' = J(M{:}S\ \textit{Current density}) * P(\textit{Probability of Tunneling})$$

$$= A^{*} T^{2} exp\left(-\frac{q\varphi_b}{kT}\right) exp(-a\sqrt{X}l) exp(\frac{qV}{\eta kT}) \left[1 - exp\left(-\frac{qV}{kT}\right)\right]$$

Here, A* represents the Richardson constant, Φ_b denotes the Schottky Barrier, η represents the Ideality Factor, and X signifies

the difference between the semiconductor electronegativity and the interfacial layer electronegativity in the M:I:S structure. In the current case, X can be estimated as the sum of the difference between ZnO's conduction band and the conjugated molecule's LUMO level, and the difference between the conjugated molecule's LUMO level and the binder's LUMO level. The variable l represents the thickness of the interfacial layer, which in this case consists of the conjugated molecule and the binder, m* denotes the effective mass of the electron, and $\boldsymbol{a} = \frac{4\pi\sqrt{2m^*}}{h}$.

As a result, the size of the apparent Schottky barrier is defined as follows, indicating its proportionality to l and X. Although we desired to determine these sizes through Density Functional Theory simulation, we will conclude this analysis due to technical limitations.

$$\boldsymbol{\varphi_{ap\_b}(Apparent\ Shottky\ Barrier) = \varphi b + \frac{(\alpha k T l\sqrt{X})}{q}}$$

2.3.6.2. Semiconducting inks – Semiconducting inks

The presence of a conjugated molecule not only enhanced the conductivity of ZnO–PCL inks but also facilitated Fermi level alignment with other inks. We observed the formation of a P–N junction, as verified by the asymmetric IV curve resulting from the heterojunction between p-type Si–PCL ink and ZnO–PCL ink. In the absence of a conjugated molecule, a symmetric IV curve was observed, indicating the absence of a depletion zone. However, in the configuration where a conjugated molecule was included with P-type Si and ZnO ink, an asymmetric IV curve was observed, with an on/off ratio of approximately 33 (−10 V to 10 V).

From a microscale perspective, in the absence of a conjugated molecule, the interface consists of ZnO : binder : SiO_2 : p-Si. SiO_2 has a high dielectric constant and a crystalline structure, while the binder polymer has a relatively low dielectric constant and an

amorphous structure, making it difficult to create a PIN junction due to the difficulty in Fermi-alignment by defects or trap sites. On the other hand, in the presence of a conjugated molecule, the HOMO level of the conjugated molecule is pinned to the Fermi level of ZnO fillers. Inter-molecular conduction occurs between conjugated molecules, reaching the native oxide layer of the Si filler through a quasi-Fermi-pinning state, and a PIN junction is formed among the aligned Fermi levels.

2.3.7. Passive / Active components

After understanding the junctions between biodegradable 3D printable electronic materials (conductor, semiconductor, dielectric), we were able to fabricate biodegradable structural passive/active components. Currently, it is difficult to discuss integration efficacy due to low resolution. However, if the resolution for bio-interfaced electronics becomes similar to conventional processing methods, the 3D spatial connectivity of inks can provide several benefits. This includes a high surface area electrode configuration for capacitors, high freedom of Z-axis design to maximize the effective closed-loop area of magnetic flux density for inductors, and the ability to deploy an active channel for electron conduction pathway in a 3D short path for active components.

For passive components, fabrication is possible through the printing of conductor, dielectric, and structural layers. As a demonstration, we created 3D structures based on Zn-PCL, SiO_2/MgO-PCL, and PBAT. Performance was evaluated based on structural variations. An interdigitating capacitor showed a change in AC capacitance (0.69 – 2.34 pF) by stacking a different number of layers (1 – 4) at a frequency of 1 MHz. A square-type solenoid exhibited an increase in inductance (68 – 262 nH) by adding turns (1 – 4) at a frequency of 1 MHz.

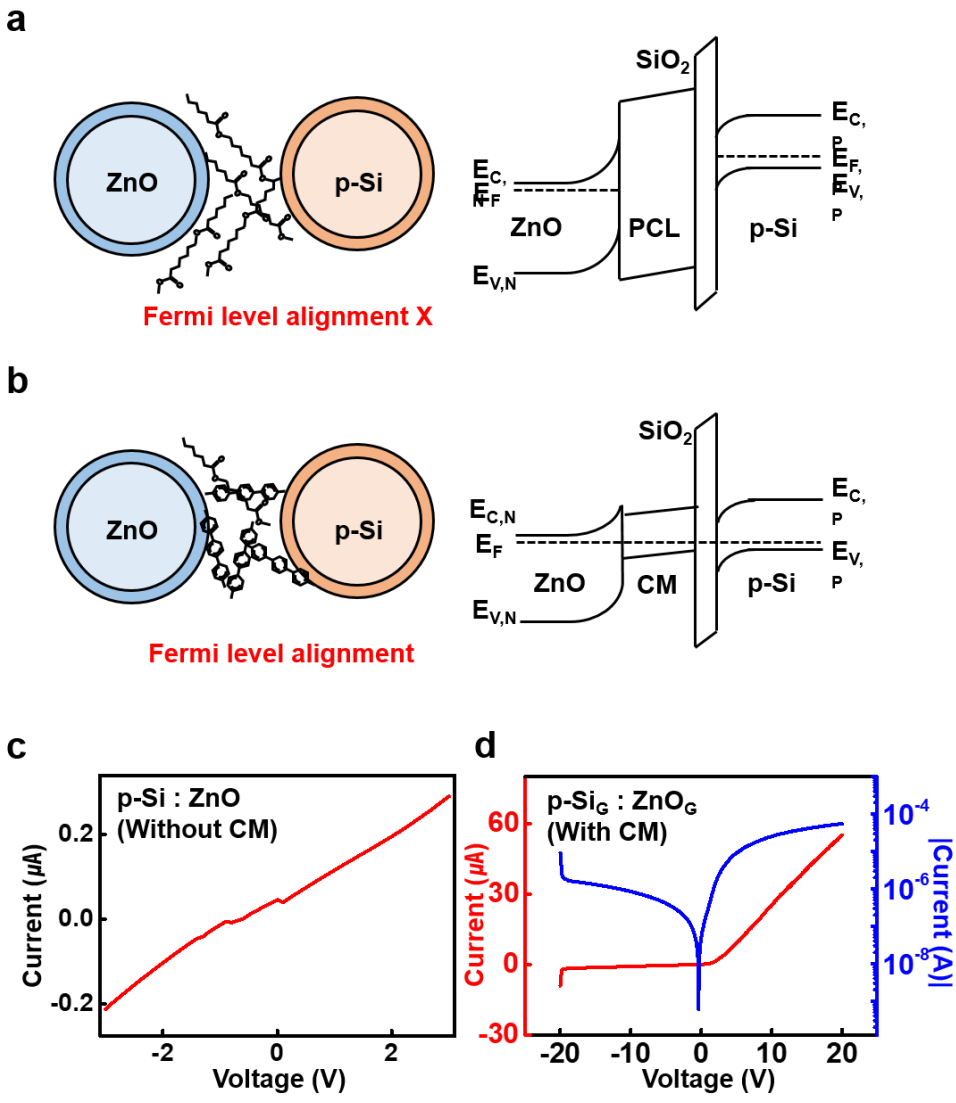

Figure 23. Semiconductor and semiconductor junctions (a) Schematic illustration when conjugated molecule is absence between ZnO and p-Si. (b) Schematic illustration when conjugate molecule is presence between ZnO and p-Si. (c) IV curve of p-Si / ZnO without conjugated molecule. (d) IV curve of p-Si / ZnO with conjugated molecule

For active components, printing was possible based on conductor, semiconductor, and solid-state electrolyte. In the case of a Schottky diode, we utilized Zn-PCL / ZnO_{BY}-PCL / Mo-PBAT. With a channel aspect ratio of Length/Height/Width = 28/3/1, we observed an on/off ratio of approximately 14 and a current output of around 0.1 mA at a forward bias of 1 V. Additionally, for a PN diode, we used Zn-PCL / ZnO_G-PCL / p type Si_G-PCL / Zn-PCL, which resulted in a relatively low current of about 0.03 mA at 10 V, but an on/off ratio of approximately 33. An NPN transistor was demonstrated, where the gate control depends on the width of the depletion zone on one side of the p-type Si and n-type ZnO ink junction, while the other side always remains in the forward direction without a depletion zone.

However, due to the current technology limitations with a Z-axis thickness of about 0.3 mm, it was challenging to create a field-effect transistor. Therefore, to exhibit thickness independency, we explored the use of a solid-state electrolyte, which allows the transfer of voltage to the cathodic and anodic parts through the movement of ions in the electrical double layer. We used a 1 mM NaCl-agarose electrolyte with a capacitance of approximately 6 uF/cm^2. The solid-state electrolyte was placed below, and the source, drain, channel, and gate were printed on top. The performance of the transistor was estimated using the saturation of the transistor formula[120, 121],

$$\mu_{Sat} = \frac{\left(\frac{d\sqrt{I_D}}{dV_G}\right)^2}{\frac{1}{2}C_i\frac{W}{L}}$$

where, W/L = 22.5, C_i = 6 μF/cm^2, $d(I_D)^{1/2}/dV_G$ = 0.01522 $A^{1/2}$ / V, $V_{threshold}$ = 1.14 V, resulting in a mobility of 0.533 cm^2/Vs and an on/off ratio of 1.68 x 10^4 (-4 V to 4 V). When a (+) voltage was applied to the side gate electrode, the solid-state electrolyte

prevented the permeation of ZnO_{Al} channels by ions due to global biasing. As a result, electron accumulation occurred in the channel in response to cations, forming a channel and increasing the population of transporting electrons.

Afterward, we were curious about the feasibility of creating a wireless antenna for communication with external devices using each component, with the possibility of eventually completing an NFC chip. To match the frequency of the phone's NFC, which is 13.56 MHz, we printed an inductor (~1030 nH). We integrated it with the capacitance of an NFC tag 213 (50 pF) and an additional SMD chip-based capacitor (~25 pF) to ensure resonance frequency alignment. We confirmed the matching resonance frequency through an S_{11} graph and verified actual communication with a mobile phone.

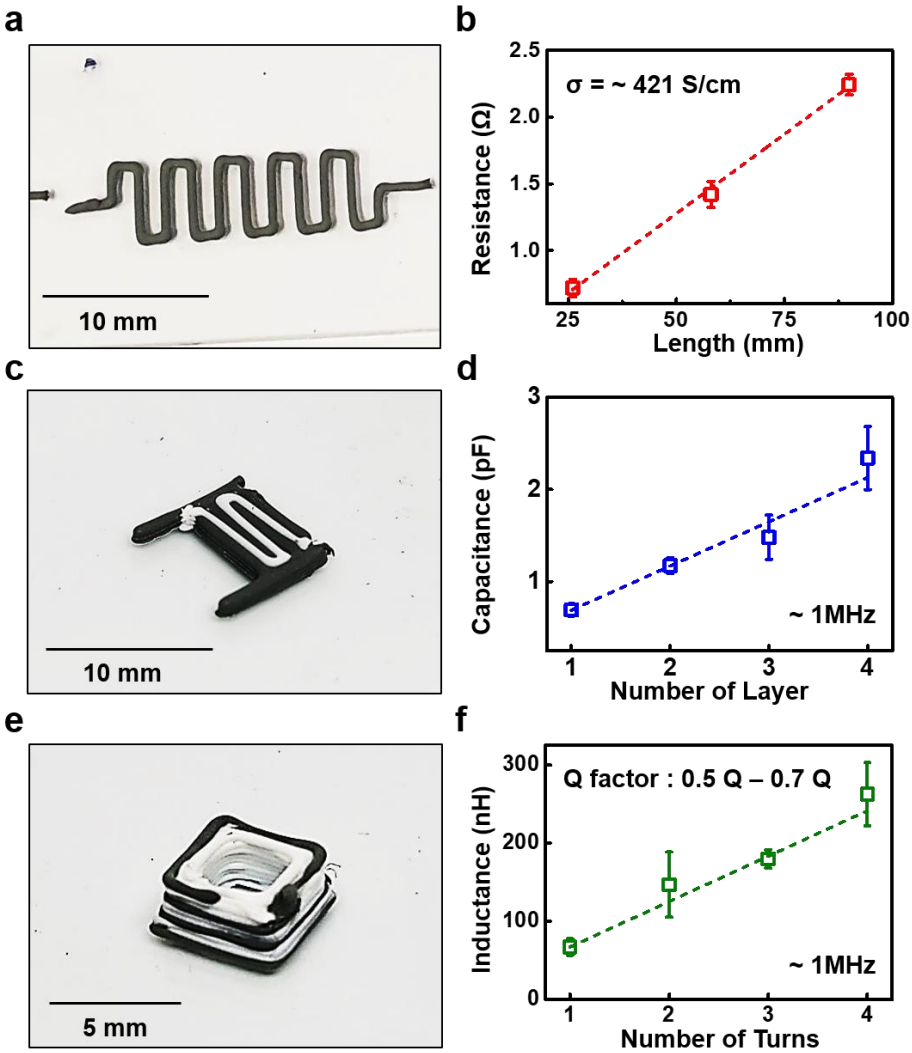

Figure 24. Image and performance of passive components. (a) Image of printed resistor (b) Resistance change by length of printed Zn resistor (c) Image of printed capacitor (d) Capacitance change by number of layer in printed Zn / SiO_2:MgO /Zn capacitor (e) Image of printed inductor (f) Inductance change by number of vertical turns of printed Zn inductor.

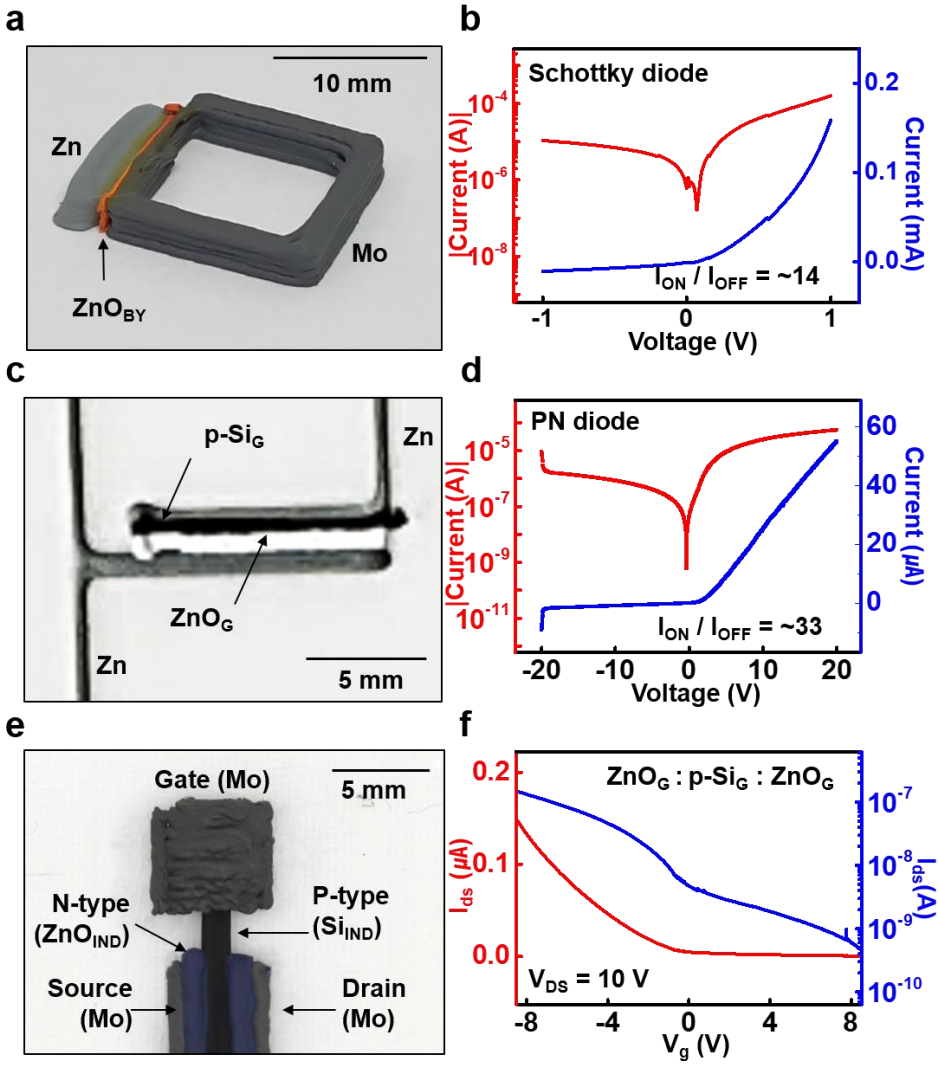

Figure 25. Image and performance of printed active components (a) Image of printed Schottky diode (b) IV curve of Schottky diode Zn / ZnO_{BY} / Mo (c) Image of printed PN diode (d) IV curve of PN diode Zn / ZnO_G / p−Si_G / Zn (e) Image of printed NPN transistor (f) IV curve of NPN transistor Mo for source, drain gate with ZnO_G / p−Si_G / ZnO_G.

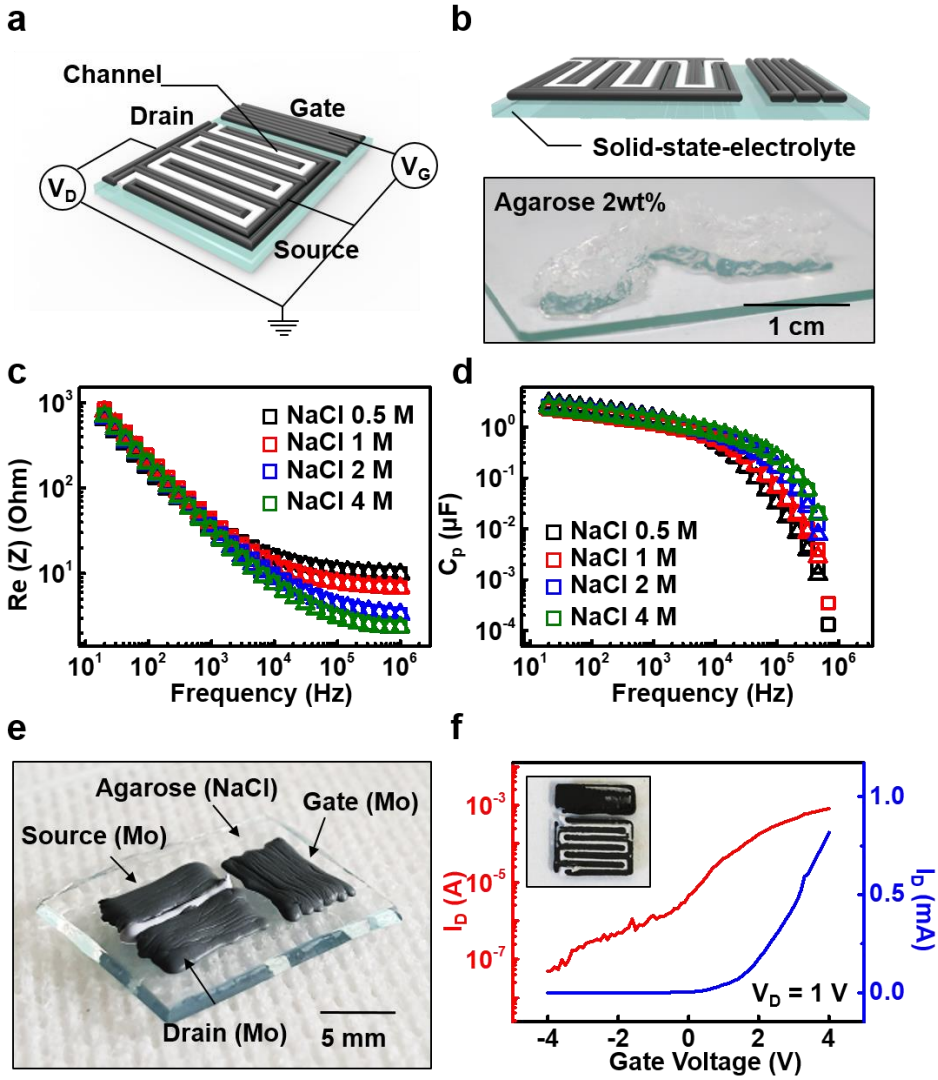

Figure 26. Image and performance of electrolyte gated transistor. (a) Schematic illustration of electrolyte gated transistor. Sided gate type transistor. (b) Image of printed soli-state electrolyte (c) Real part of impedance and (d) Real part of capacitance of solid-state electrolyte by frequency change. (e) Image of printed basic electrolyte gated transistor (f) Transfer curve of electrolyte gated transistor with interdigitated electrode.

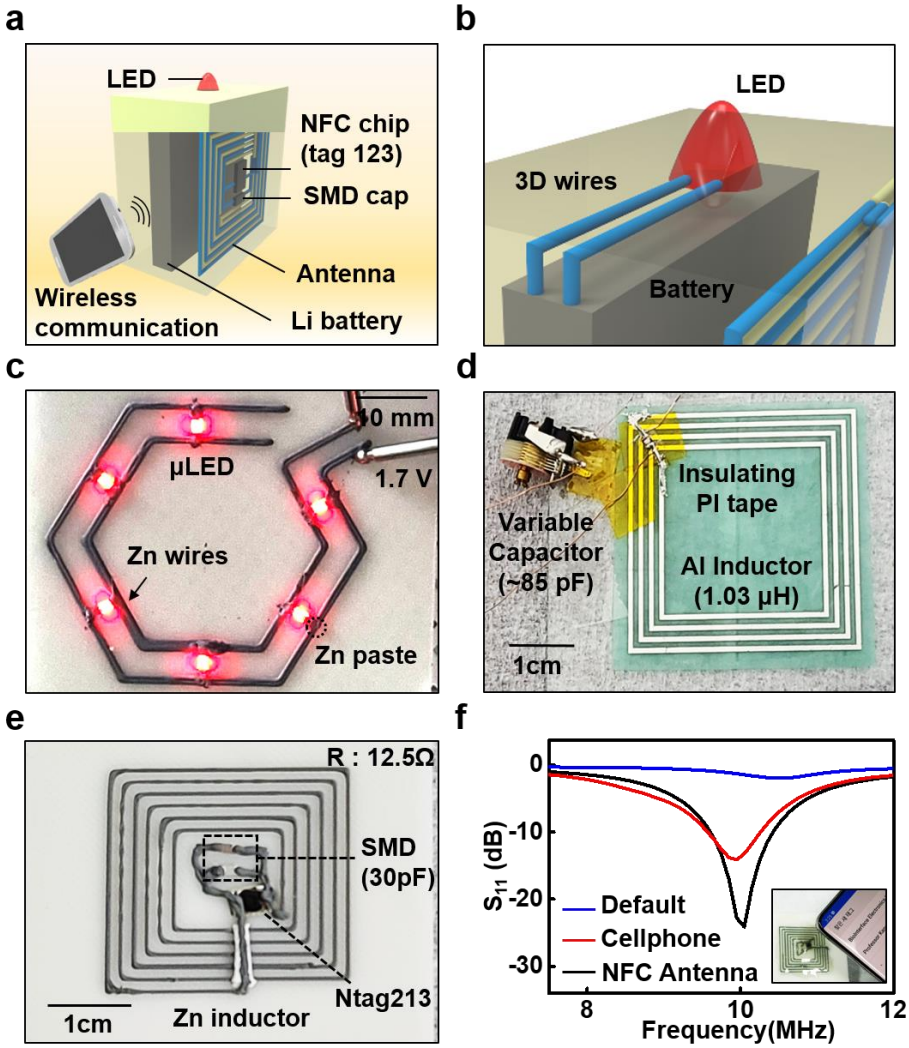

Figure 27. Wireless communication via printed inductors and wires. (a) Schematic illustration of wireless communicating device with commercial NFC chip and SMD capacitor (b) Illustration for possibility of 3D organized wires in devices (c) Image of 6 LED operation connected to Zn wires under 1.7 V. (d) Image of optimized NFC antenna with Al conductor and variable capacitor (e) Image of printed NFC antenna integrated with chips (f) Return loss (S_{11}) of printed wireless antenna and cellphone.

2.3.8. Physical / Chemical biosensors

In addition, the previous inks allowed for the creation of various sensors. One advantage of 3D printing is the ability to customize the placement or embedding of sensors according to the tailored structure, enabling production within a three-dimensional framework. Firstly, for physical sensors, we fabricated a temperature sensor based on Zn resistor, a UV sensor based on Mo / ZnO_{Al} / Mo photoresistor, and a pressure sensor in the form of a trench-printed PBAT with electrodes on both sides, resulting in a Mo/air/Mo capacitor structure. As for chemical sensors, we created a pH sensor by measuring the potential difference of a two-electrode system consisting of ZnO_{Al} / Zn protected with an encap layer and Ag/AgCl, and a glucose sensor by measuring the response current of a three-electrode system with a Pt electrode based on glucosidase, a redox mediator using MoO_3 with low redox potential, and Ag/AgCl electrodes.

Based on this, we conducted demonstrations involving the printing of sensors on static/dynamic structures to achieve conformal contact within a three-dimensional space. Initially, we generated G-code to print a 2 x 2 array of temperature sensors on a stair-like slope. When touching one part of the sensor, we observed a sharp increase in resistance, corresponding to an increase of approximately 7.0℃. We also created a shape-shifting structure using shape memory polymer known as PLA, allowing for programming and recovery. On a dome structure with a bow-tie shape metamaterial, we generated G-code to print an array of UV sensors. After programming, we continuously monitored the UV lamp while inducing shape shifting using a heat gun (~70℃). We observed that sensors closer to the UV lamp exhibited higher conductance during shape shifting.

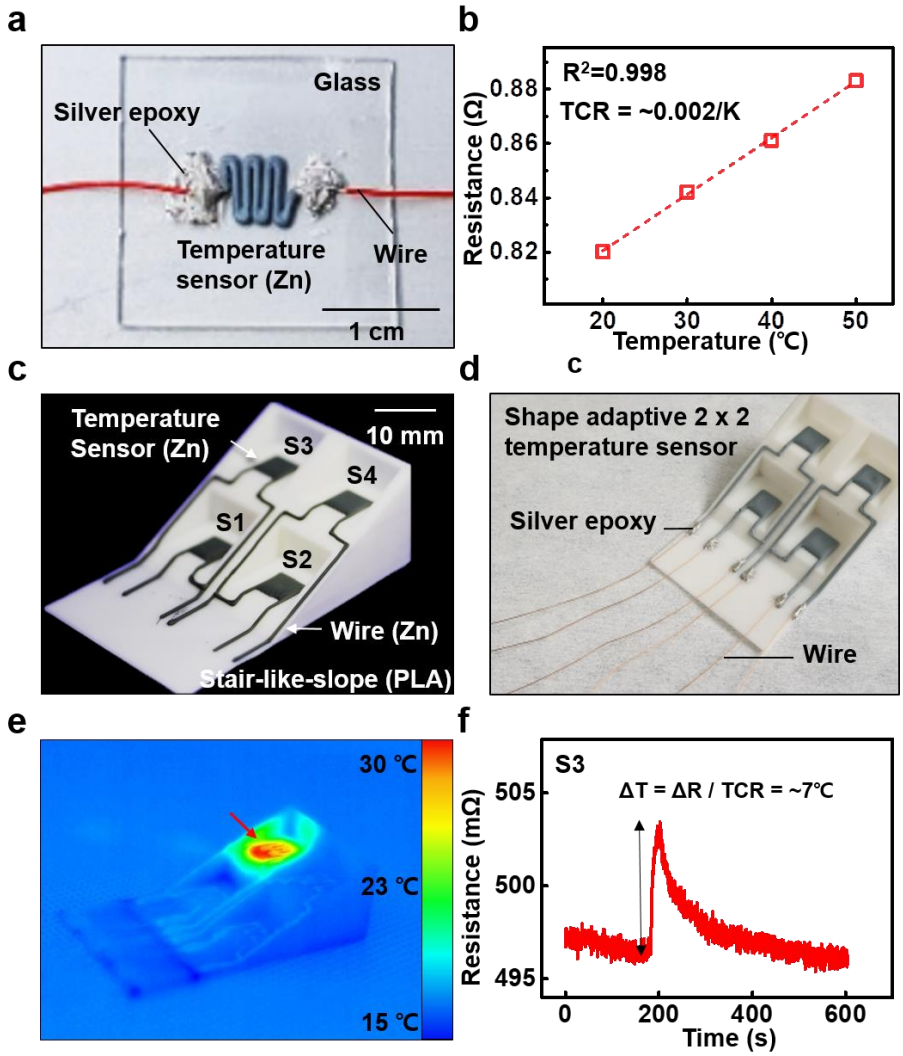

Figure 28. Image and performance of temperature sensor (a) Set-up for testing temperature sensitivity of Zn resistor (b) Resistance change by temperature of Zn resistor (c) Image of printed 2 x 2 temperature sensor array on complex plane (d) Image of wired temperature sensor array (e) IR image temperature sensor array with selectively heated S3 sensor (f) Resistance change by temperature change of sensor in real-time.

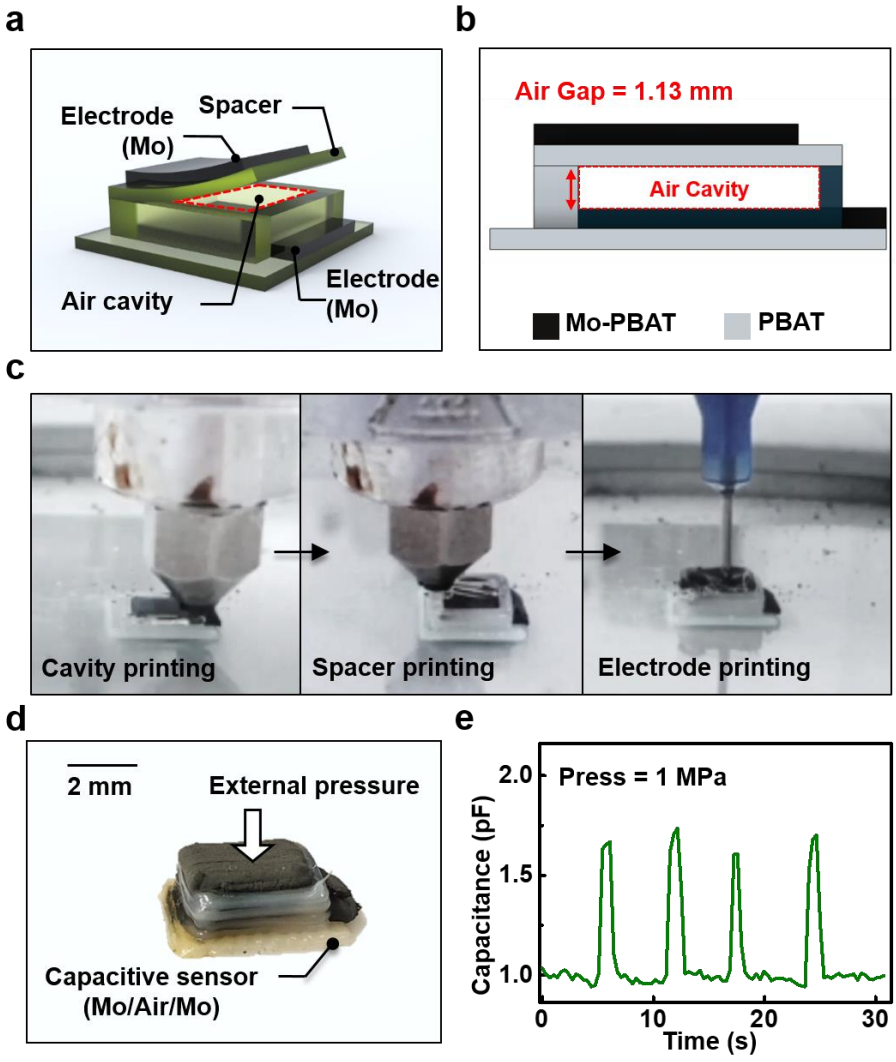

Figure 29. Image and performance of pressure sensor (a) Schematic illustration of trench structured capacitive pressure sensor (b) Side view of the sensor with air gap 1.13 mm (c) Serial images of printing process of sensor (d) Image of printed pressure sensor (e) Capacitance change of the sensor by repetitive external pressure in real-time.

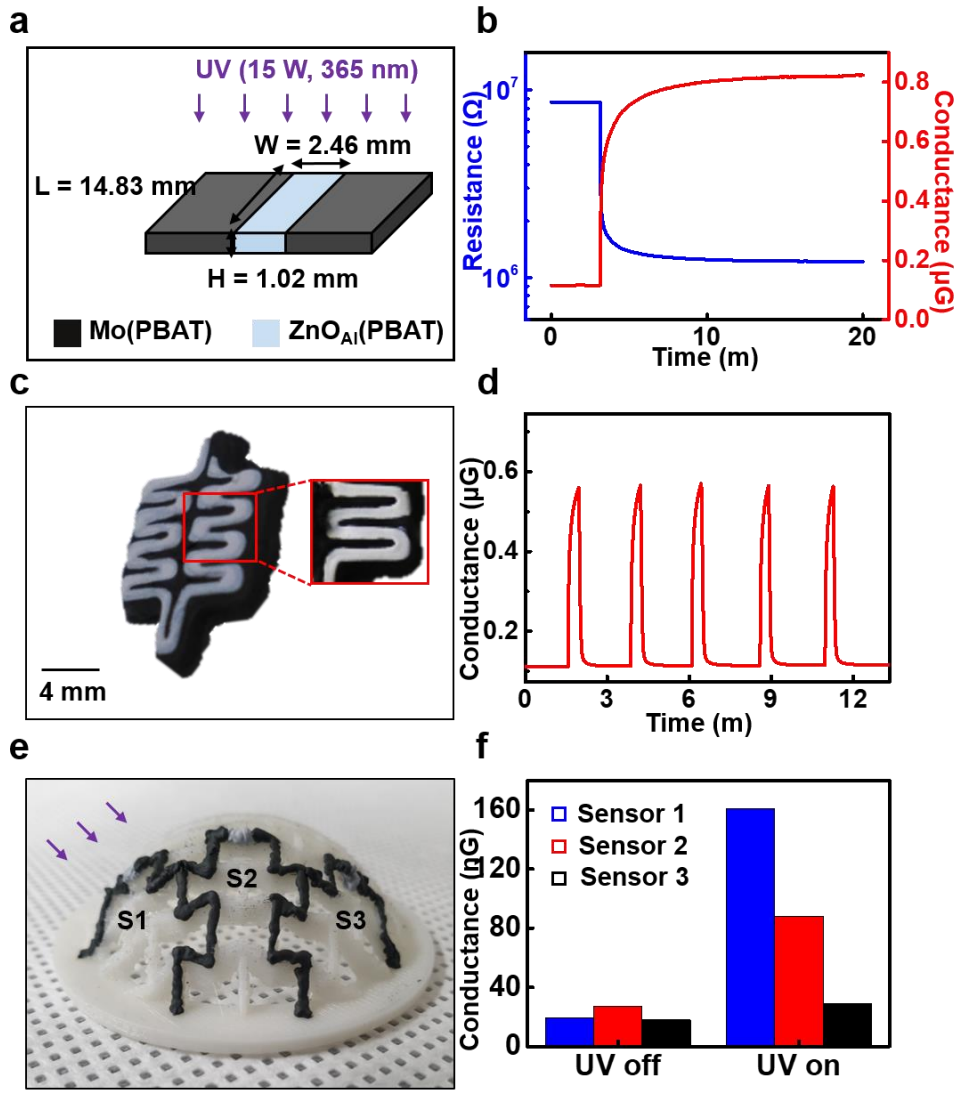

Figure 30. Image and performance of photodetector (a) Schematic illustration of UV sensing unit (b) Resistance and conductance change of UV sensing unit by time (c) Image of printed UV sensor with interdigitating electrodes (d) Conductance change of UV sensor with repetitive UV irradiation in real-time. (e) Image of printed UV sensor array on complex plane (f) Conductance change before and after UV irradiation within different distance from UV source.

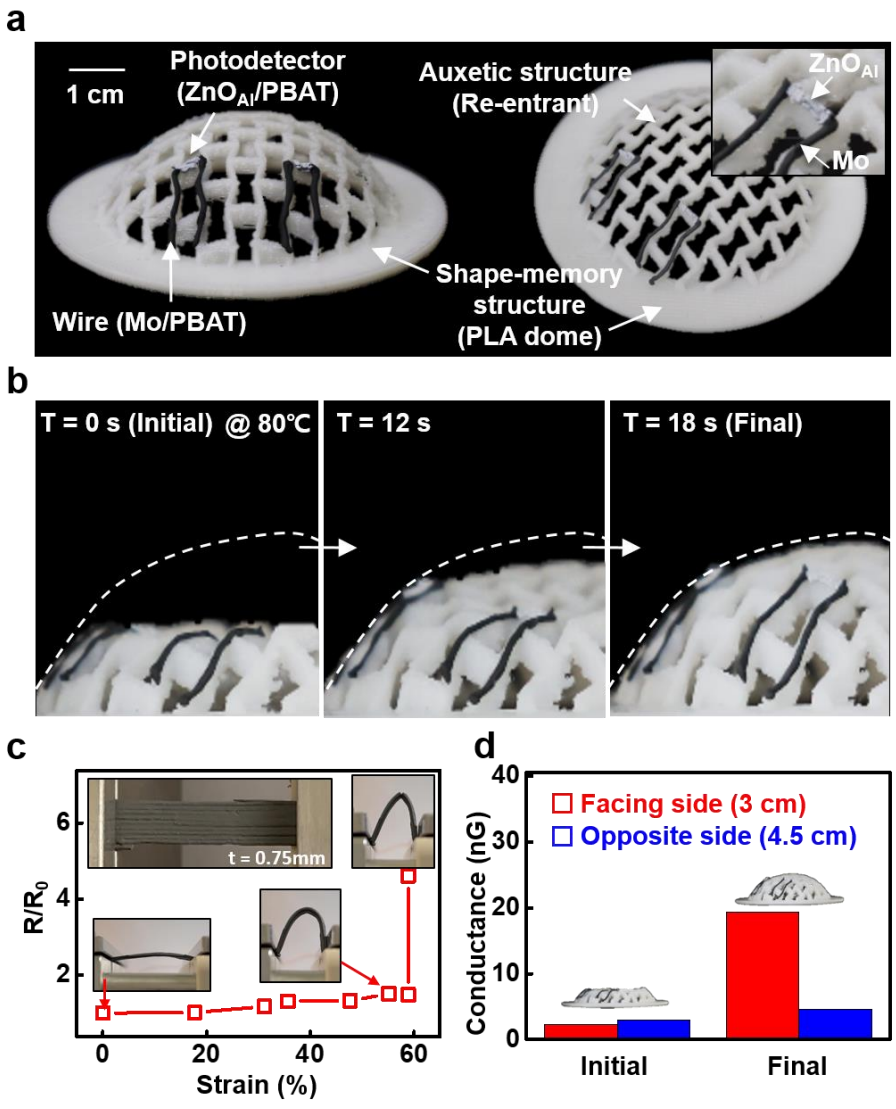

Figure 31. Image and performance of shape shifting photodetector (a) Image of printed UV sensor array on shape shifting complex structure (b) Serial images of shape shifting of UV sensors on the structure by shape recovery of PLA with external heat (c) Resistance change Mo trace by strain changes. Strain is defined as horizontal change of length which is gap between two jigs. (d) Conductance change of UV sensor before and after shape-shifting with different distance from continuous UV irradiating source.

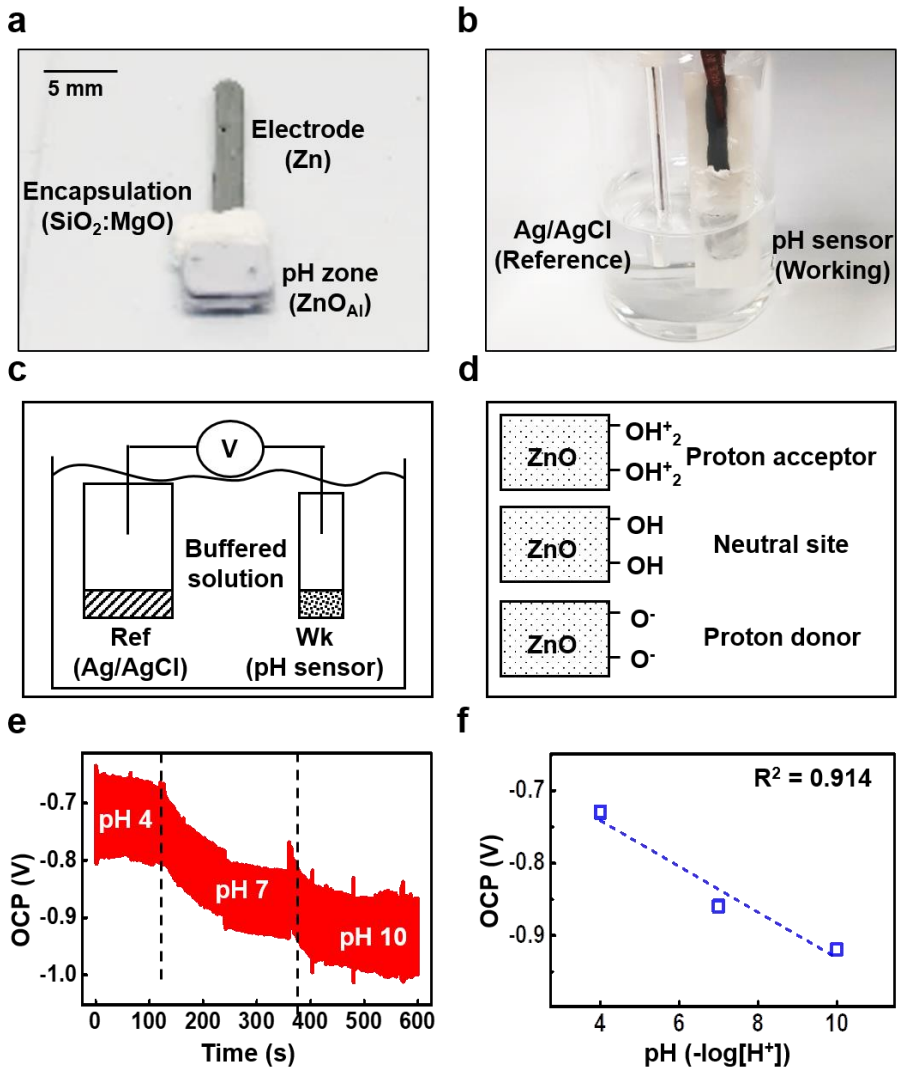

Figure 32. Image and performance of pH sensor (a) Image of printed pH sensor (b) Image of measurement set-up for pH sensor (c) Schematic diagram of two electrode system for operating pH sensor (d) Illustration of ZnO surface state by different pH of the interfacing solution. (e) Open circuit potential difference by various pH (4, 7, 10) in real-time. (f) Calibrated curve of OCP by pH.

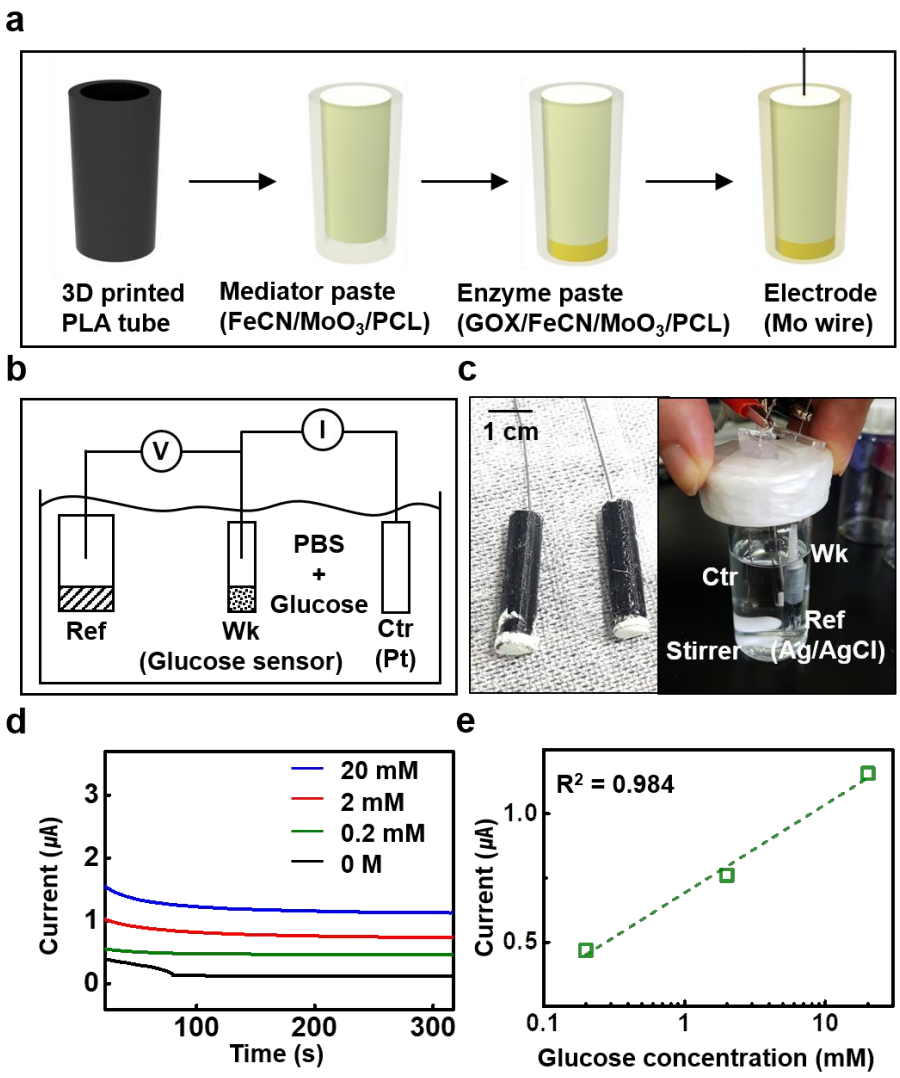

Figure 33. Image and performance of glucose sensor. (a) Fabrication process of glucose sensor (b) Schematic diagram of three electrode system for operating glucose sensor (c) Image of measurement set-up for glucose sensor (d) Response current change of glucose sensor by various glucose concentration in PBS in real-time (e) Calibrated curve of response current by glucose concentration

2.4. Conclusion

In Chapter 2, we developed biodegradable electronic inks suitable for 3D printing and created conductive, semiconductor, and dielectric inks. To enhance conductivity, we employed room temperature sintering for conductive inks and room temperature / normal pressure grafting for semiconductor inks. After conducting research on these materials, we investigated junctions between different inks, resulting in the fabrication of a Schottky diode based on Zn / ZnO_{BY} / Mo and a PN diode based on Zn / p type Si_G / ZnO_G / Zn. We were also able to create an NPN transistor. Furthermore, by introducing a solid-state electrolyte, we fabricated a side-gated field-effect transistor. Subsequently, we produced sensors that could read signals when in contact with a three-dimensional surface. These included temperature sensors, pressure sensors, UV sensors, pH sensors, and glucose sensors, which were validated for conformal application on both static and dynamic structures in three dimensions. Additionally, mean-time, we are developing methods to address porosity inside printed inks with porogen leeching methods, to utilize biodegradable gel bead for extremely soft biodegradable conductor and to synthesize 3D networking ZnO fillers to improve the mechanical and electrical properties of the printed components.

Chapter 3. 3D printed biodegradable electronic system for biomedical applications

3.1. Motivation

Implantable electronics interact with the human body through closed-loop operation, consisting of two systems. One system monitors vital electrophysiological signals such as blood pressure or cardiac mapping, as well as biomarkers like glucose and cortisol[3, 20]. The other system is designed for therapeutic purposes, involving stimulation or integration with cells to treat specific tissues or neuromodulation[14, 20]. For these systems to function within the body, wireless operation is necessary. The key components required for this purpose can be broadly categorized as follows [13]: (1) Power source: Wireless powering, battery, or energy harvester, (2) Wireless data communication, (3) Physical, chemical, and electrophysiological sensors, (4) Stimulation electrodes. To implement these components, we can leverage the passive and active components, as well as the sensors based on the 3D printable biodegradable electronic inks developed in Chapter 2. However, the challenge lies in seamlessly integrating these components into customized 3D structures.

Although the ultimate goal is to achieve conformal contact with complex targets exhibiting Riemann curvature, we started with considering the invasiveness of the target construct such as tissues or aritificial implants, then we devised three types of conformal contact: (1) Surrounding contact (non-destructive), (2) Penetration contact (semi-destructive), (3) Embedded contact (destructive). We aimed to demonstrate one example for each of these three cases. Thus, our objectives were to create a customized electronic conduit for wireless stimulation in peripheral nerve injury cases, a minimally invasive plug-in device for EcoG measurements with bundled wiring in a 3D structure, and a tailored electronic implant for monitoring internal pressure in bone defects.

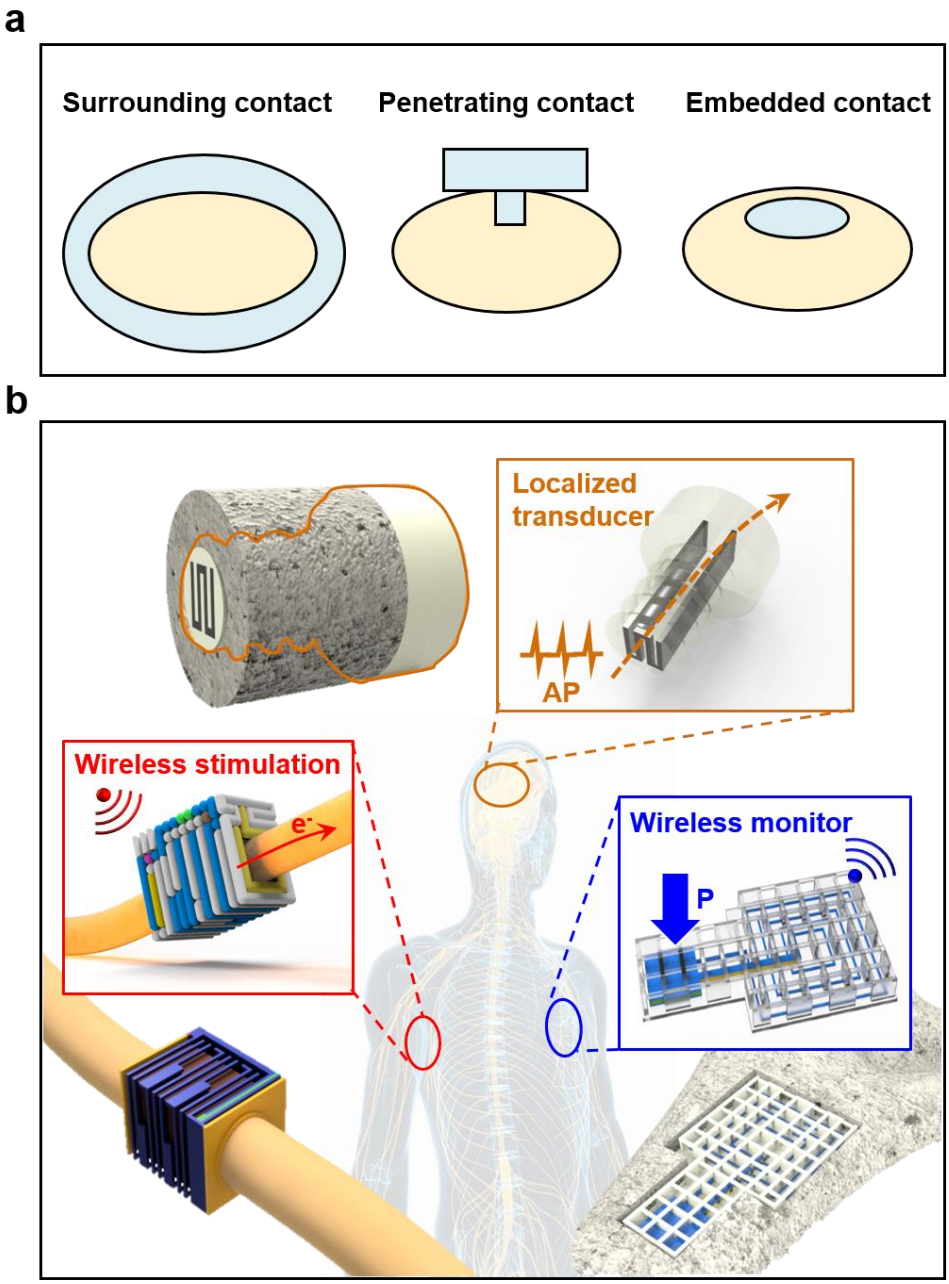

Figure 34. Various conformal contact modes and applications (a) Various conformal contacts : surrounding, penetrating, embedded (b) Biomedical applications with various contacts : wireless nerve stimulator, plug-in electrophysiological sensor, wireless bone monitoring sensor

3.2. Materials and methods

3.2.1. Small animal model

Sprague Dawley rats (male, 12 weeks old, weighing approximately 290-310 g) were used in the experiments. All animal care and surgical procedures were performed in compliance with the regulations of the Dankook University Animal Ethics Committee (approval number DKU-22-063). All experimental animals were individually housed in cages with sufficient food and water, and maintained at a temperature of 22-24℃ and a humidity of 45-50% in a specific pathogen-free facility. The complete sciatic nerve injury model was created in a total of 12 rats and divided into three groups: injury only, non-transient stimulator implantation, and stimulator implantation using a 3D printer. For the surgical procedure, anesthesia was induced with 5% isoflurane in a mixture of oxygen and nitrogen (1:3). The hair in the left thigh area was shaved with a razor and the incision site was sterilized with povidone-iodine. The skin and subcutaneous layer were incised with scissors and the muscle layer was separated along the muscle bundle to expose the sciatic nerve. The surgical site was located at the proximal 15 mm segment of the sciatic nerve, where the tibial and common peroneal nerves branch out from the sciatic nerve, and extended to the hip joint. The sciatic nerve was completely cut using microscissors and a stimulator made with a 3D printer was implanted into the injury site. The nerve was sutured using 10-0 Nylon, and the surrounding muscles and skin were sutured using 6-0 ethilon after nerve repair. In the control group, a non-transient stimulator was implanted into the same surgical site, and the nerve was sutured using the same method as the experimental group. After surgery, the rats were allowed free movement without any special fixation.

3.2.2. Large animal model

Six 6-month-old female beagles were used in the experiment under the following breeding conditions: temperature was maintained at 23±2°C, humidity was maintained at 50-60%, and ventilation was maintained at 10-20 times per hour. All animal care and surgical procedures were performed in compliance with the regulations of the KBIO institutional Animal Care and Use Committee (approval number KBIO-IACUC-2021-275). The animals were pre-anesthetized with Zoletil (5mg/kg) and xylazine (2mg/kg) and intubated for inhalation anesthesia with isoflurane (3%), while monitoring their anesthetic state using an ECG, Spo2, and EtCO2 monitoring system. Prior to skin incision, 2% lidocaine was administered at the incision site for local anesthesia. The skin, subcutaneous tissue, and muscles above the sciatic nerve were sequentially incised to expose the sciatic nerve. The sciatic nerve was cut approximately 2 cm from the distal end of the femoral joint, and a 3D printed electrical stimulator was connected and the incision was sutured. The operability of the 3D printed electrical stimulator was verified using EMG. We also confirmed the physical stability of the 3D-printed stimulator in vivo by C-arm imaging after its implantation.

3.2.3. Measurement of electrophysiology

All groups were anesthetized using the same method and underwent nerve conduction testing each week. For the sciatic nerve conduction test, the rats were positioned on their sides and the active electrode was attached to the rats' biceps femoris muscle, with the reference electrode attached to the Achilles tendon and the ground electrode attached to the tail. The distal part of the sciatic nerve was stimulated using a wireless stimulation electrode, with a interval 33.33 ms, pulse width 200 μs which has frequency of 30 Hz which is different from therapeutic stimulation. CMAP was measured with EMG measurement equipment (IX-RA-834 10+

Channel Recorder and Stimulator, iWorx co., ltd) and CNAP was measured with Neuropack S1, MEB-9400, Nihon Kohden co., ltd.

3.2.4. Tissue collection

To perform tissue collection and analysis, anesthesia was induced using isoflurane (5%) with a ratio of 1:3 oxygen to nitrogen for inhalation anesthesia, as in surgical procedures. The muscle tissue, which had undergone electrophysiological testing the last 8 weeks, was snap-frozen immediately, and the sciatic nerve tissue was fixed using 0.9% NaCl solution perfused throughout the model's body and fixed with 4% paraformaldehyde. The sciatic nerve tissue for axon counting was excised approximately 25-30mm and placed in the same fixative solution for approximately 4 hours at 4℃. The tissue was then treated with 30% sucrose to prevent damage to the tissue that could occur during freezing and sectioned into 16㎛ thickness using a cryostat microtome and mounted onto slides using the M1 compound (Thermo Fisher Scientific).

3.2.5. Immunohistochemistry

A sciatic nerve tissue that was fixed with M1 compound (Thermo Fisher Scientific) was sectioned into 16 ㎛ thickness in both sagittal and horizontal planes. The sectioned tissue was treated with 2% normal goat serum containing 0.2% triton X-100 to block non-specific binding, and to prevent non-specific staining with 2% normal goat serum. The primary antibodies used were Tuj1 and S-100 (mouse TUJ1 monoclonal antibodies, 1:1000, Abcam; rabbit S-100 polyclonal antibodies, 1:1000, Thermo Scientific, RP-75723) to stain nerve fibers, and CD68 (Invitrogen) and CD86 (Invitrogen) to stain M1 phenotype macrophages. The secondary antibodies used were FITC-conjugated goat anti-mouse IgG and Rhodamin-conjugated goat anti-rabbit IgG (Jackson Immuno-Research Laboratories), respectively. The number of regenerated axons and the number of M1 macrophages were

calculated by measuring the number of axons stained with TUJ1 and the number of co-localized cells stained with CD68 and CD86 in the horizontal plane using Image J.

3.2.6. Measurement of muscle atrophy and recovery

The gastrocnemius muscles of the experimental and control groups, which had undergone snap-freezing, were sectioned horizontally to a thickness of 10 μm using cryo-cutting, stained with hematoxylin-eosin, and morphologically observed for muscle atrophy. The observed tissues were measured for the surface area of muscle fibers according to each group using Image J.

3.2.7. Statistics

The SPSS 21.0 (IBM SPSS, Armonk, NY, USA) program was used for statistical analysis, and all statistics were performed using ANOVA.

3.3. Results and discussion

3.3.1. Wireless nerve stimulator

Peripheral nerve injury can lead to sensory and motor function impairment, muscle atrophy, and neurogenic pain[122]. Depending on the type of nerve damage, it can be classified as crushed, transected, short nerve, or long nerve gap injury[123]. Currently, autografts or artificial nerve conduits are used for such treatments[124-126], but it has been reported that functional recovery can be accelerated and improved through electrical stimulation[127]. There have been numerous attempts to develop wireless stimulators on a sub-millimeter scale. Various power sources have been explored, including the use of piezoelectricity generated by external ultrasound[128], photoelectricity through skin penetration by lasers[129], magnetoelectricity delivered

through percutaneous catheter[130], inductive voltage utilizing resonant frequency[131], and triboelectricity through self-powering within the body[132]. Additionally, different structural designs have been considered, such as clip-shaped[133], locking-shaped[134], vein-shaped based on shape memory[135], and conduit-shaped based on self-healing properties[136].

Recently, wireless nerve stimulators in biodegradable form have shown significantly improved long-term (1d, 3d, 5d) stimulation, leading to better functional recovery and enhanced growth at the neuromuscular junction, which was previously difficult to achieve[99, 137]. Therefore, the goal was to develop a conduit-like structure that embraces the nerve, allowing for 3D integration of all components inside. This approach aimed to minimize additional surgeries for installing extra electrodes or the main body and to enable biodegradation after wireless stimulation.

3.3.1.1. Design and fabrication

3.3.1.1.1. Electronic components

The electronic components required for the fabrication of the wireless electrical stimulator were an inductor, capacitor, wires, diode, and electrode. The choice of diode was a Schottky diode because: (1) PN diodes had poor conductivity due to the characteristics of the ink used. In in-vivo experiments, even at high voltages, it was observed that only the toes of small animals were stimulated, indicating that they may not be suitable for use in large animals with higher impedance. (2) Schottky diodes can rectify high-frequency AC voltage due to the Schottky barrier, eliminating the need for recovery time in the depletion zone, unlike PN diodes.

For the inductor, based on literature data and targeting the beagle nerve, it was estimated to be around 7-10 mm. It was calculated that a stacked square inductor with approximately N = 10 turns would be required to generate enough power for wireless

powering, following common sense that a 1 μH inductor is needed. However, the quality factor varied significantly with resistance, so a biodegradable high-permeability material was introduced inside the inductor to increase the magnetic flux density. Fe_3O_4 was optimized for 3D printing conditions and incorporated inside the inductor.

The capacitor was used to match the resonant frequency of the inductor. It was necessary to examine the selective absorption rate (SAR), which determines how much heat is generated when the frequency is absorbed by the human body. In the frequency range of 100 kHz to 6 GHz, it is reported that an average whole-body SAR of approximately 6 W/kg for 1 hour is required to cause a 1-degree increase in deep body temperature for adults. However, ICNIRP suggests a 30 minute exposure limit of 4 W/kg. For children, higher SAR values are needed due to their higher heat dissipation efficiency. Therefore, there was consideration about which specific resonant frequency to use in the MHz range. However, it was reported that stimulation of the nerves could also occur through induced electric fields within the range of 100 kHz to 10 MHz. To induce nerve stimulation solely through the stimulator, the minimum frequency possible above 10 MHz was chosen.

3.3.1.1.2. 3D integration

To integrate the components inside a conduit, the following strategies were employed. First, the circuit was designed and arranged within the customized conduit, considering equipotential points for manipulation. The design of the print head's path followed the algorithmic sequence outlined below:

(1) Determination of conduit structure

(2) Tree structuring of circuits with components and interactions

(3) Stereographic placement of components in the 3D structure, considering equipotential points

(4) Determination of each component's performance and shape

(5) Slicing integrated circuits by layer and setting grids at unit layers with a unit length corresponding to the printer's feature size

(6) Manipulation of the print head's path into a Hamiltonian path for each material to minimize nozzle movements

Secondly, an algorithm was devised to determine how components should be integrated based on the size of the nerve. The algorithm proceeded as follows:

(1) Scanning the injured peripheral nerve and determining its size

(2) Setting the unit layer

(3) Designing the inductor with a boundary condition of achieving a certain inductance

(4) Designing the capacitor with a boundary condition of achieving a certain frequency

(5) Designing the diode with a boundary condition of generating the required current based on a certain channel ratio

(6) Designing the electrode and internal wires according to the manipulated circuit diagram

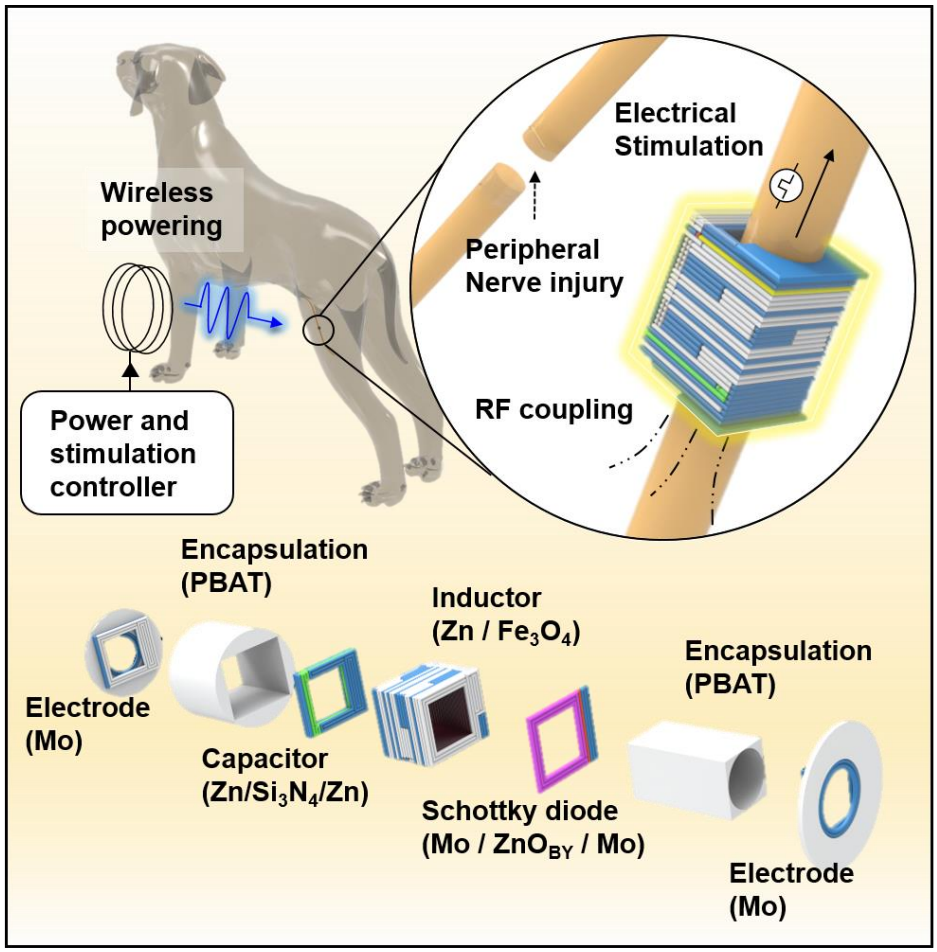

Figure 35. Illustration of wireless nerve stimulator customized for peripheral nerve injury (Electroceutical tube or electronic conduit). Stimulator is powered by external wireless stimulation controller and deliver current to sciatic nerve for therapeutic effects. Wirelessly stimulating system is packaged in nerve embracing tube, conduit shape including electrode, capacitor, inductor, Schottky diode, encapsulation.

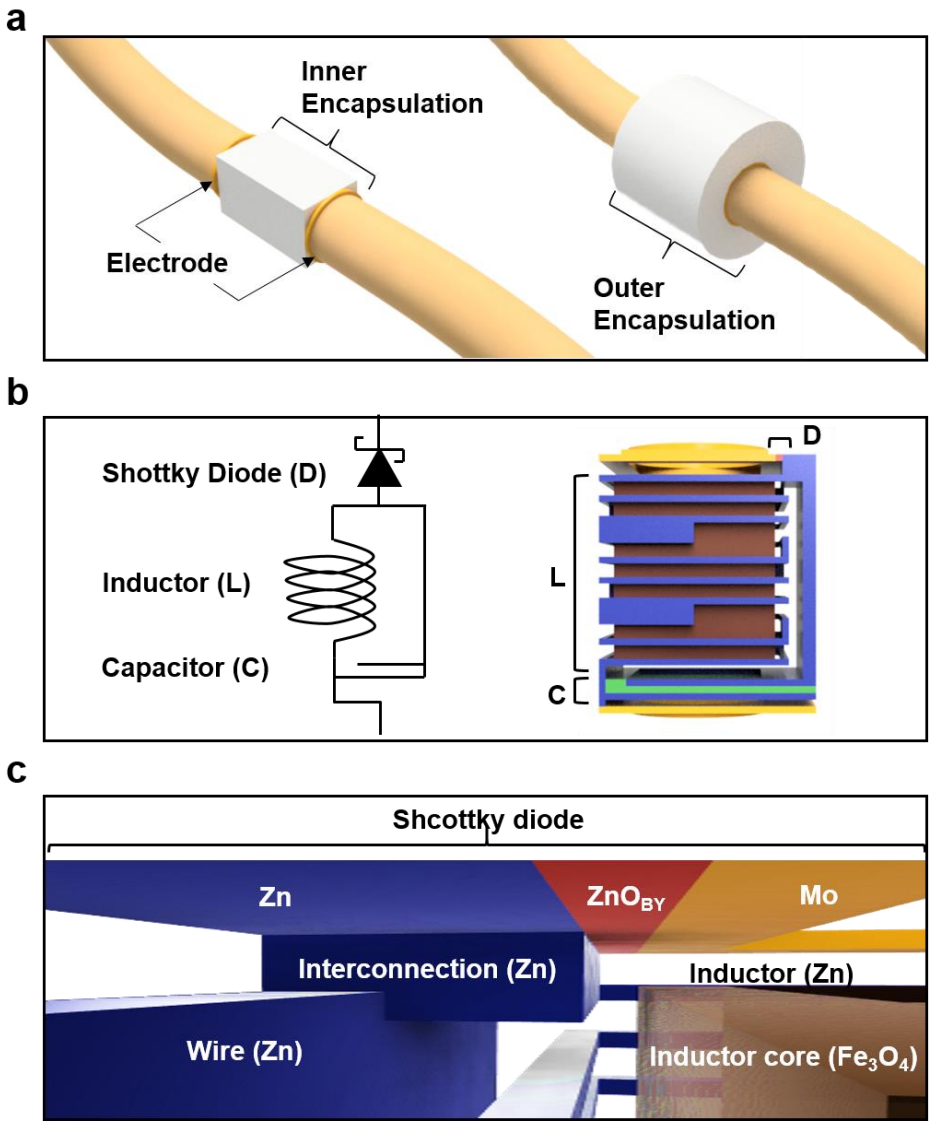

Figure 36. Structure of 3D wireless stimulator in conduit structure. (a) Structure of encapsulation and electrodes (b) Circuit diagram and structure of wireless stimulator (c) Internal 3D integration at interconnections of diodes, wires, inductors.

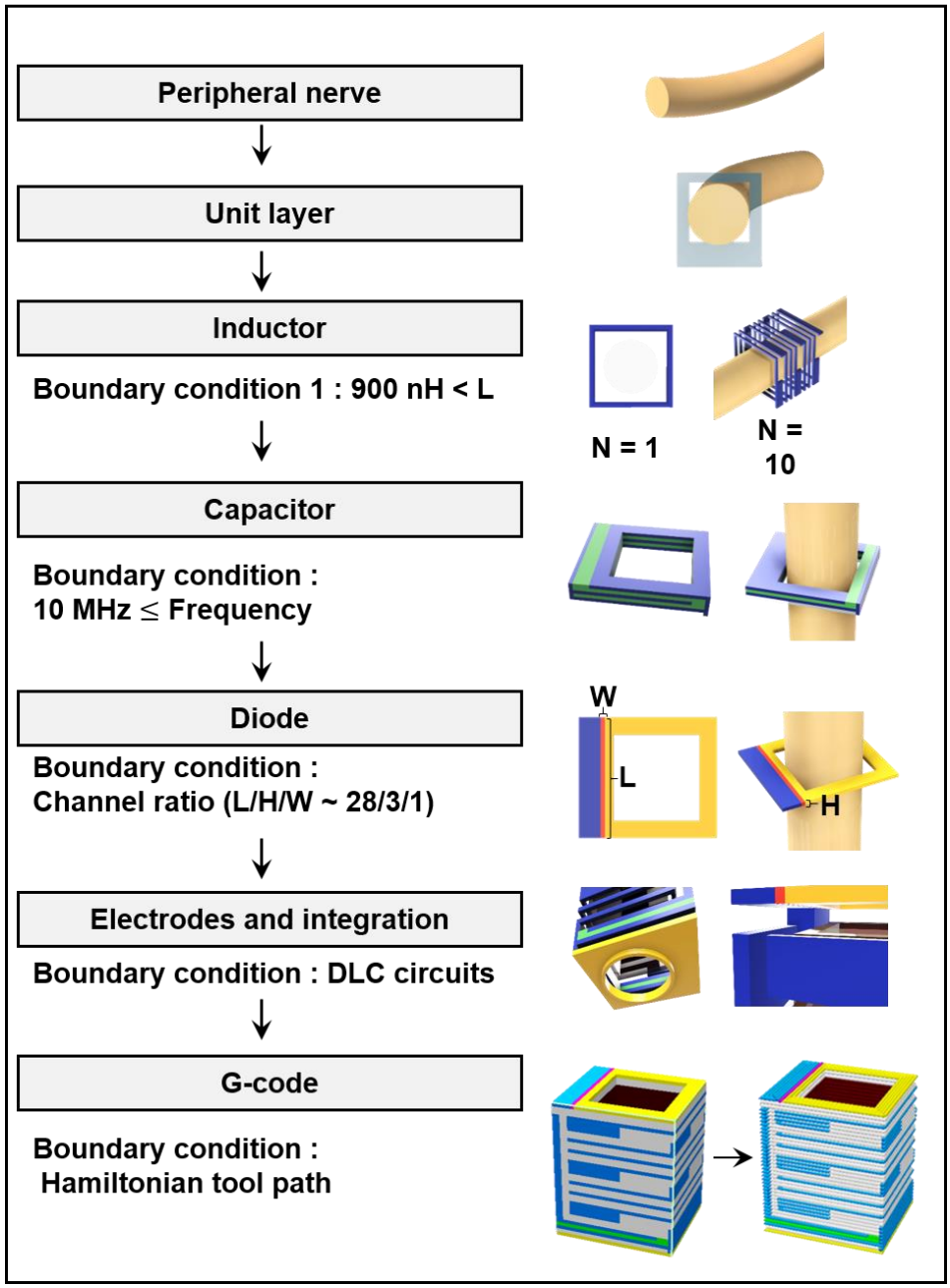

Figure 37. Design algorithm for wireless stimulator in conduit structure for various nerve sizes.

Following this design approach, during the actual fabrication process, due to practical limitations with only three nozzles available, the components were assembled separately and then connected using Zn-PCL paste. Partial sintering was performed, and subsequently, encapsulation was carried out using PBAT through dip coating. The selective exposure of only the electrode area was ensured by removing the protective coating after dip coating.

3.3.1.2. Performance

In terms of the performance of the fabricated stimulator, the individual components exhibited the following characteristics: The capacitor had a capacitance of 60-70 pF (@ 1 kHz), and the inductor had an inductance of 800-900 nH (@ 1 MHz). The internal resistance of the inductor was approximately 150-600 ohms. The resonant frequency, determined by observing the S_{11} graph, was around 10-25 MHz, with a return loss of approximately -6 dB at 10.5 MHz. Calculating the voltage standing wave ratio (VSWR) and reflection coefficient revealed values of 2.85 and 0.48, respectively, indicating that around 50% of the external RF energy was absorbed. While it was possible to increase this absorption through impedance matching with the external coil, it was challenging to achieve proper matching due to variations in the quality factor depending on the oxidized state of the fabricated stimulator and the use of a solution process, resulting in difficulty in matching frequencies with various capacitance values of the capacitor. To overcome this limitation, the external power transmission was increased, and conductive gel was utilized at the interface to enhance current injection. Regarding the output voltage, rectification was observed up to 32 MHz. When stimulated in burst mode with a frequency of 10 MHz, using a burst mode of 200 μs (pulse) and 50 ms (interval) with a 60 Vpp amplitude, a pulse of approximately 1 V was generated when loaded with 1 kohm.

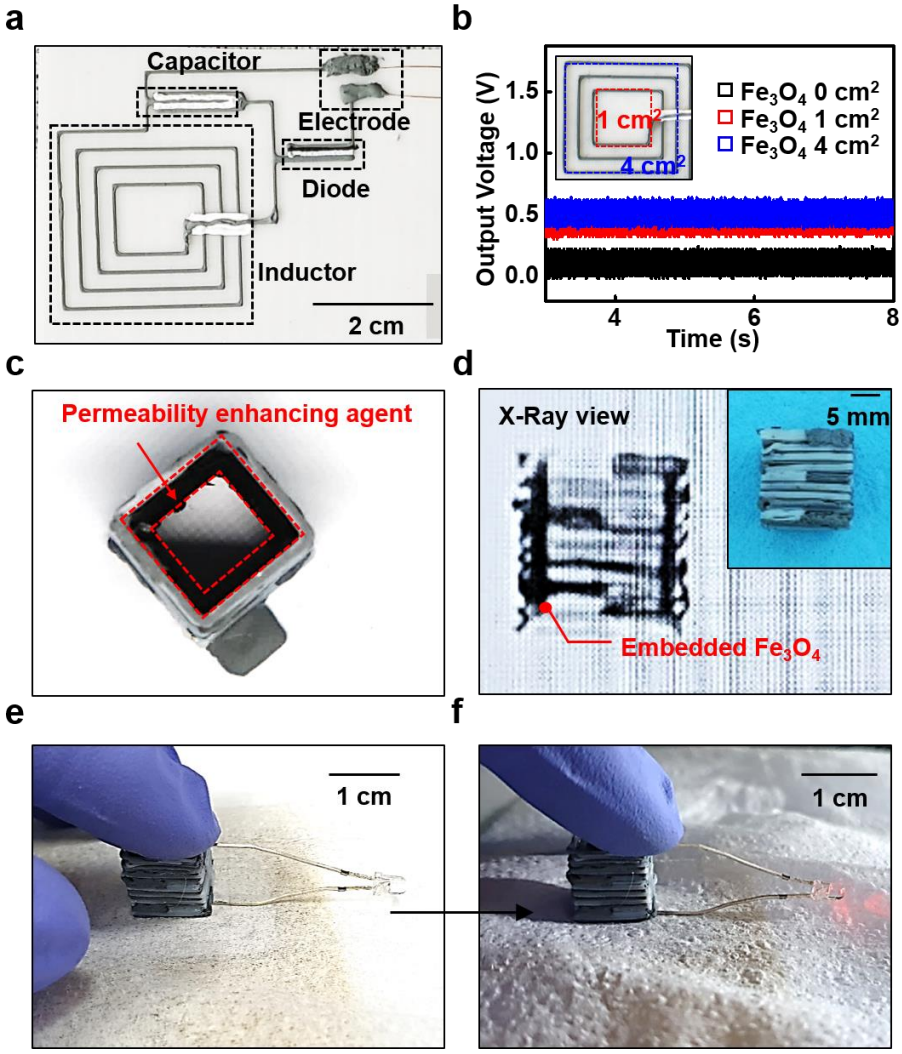

Figure 38. Ferrite effects on wireless powering system. (a) Image of printed planar wireless stimulator (b) Output voltage of the planar stimulator with different Fe_3O_4 area in the core of the inductor. (c) Optical image and (d) X-ray image of Fe_3O_4 embedded in inductor. (e,f) Wireless powering of LED with the printed inductor by inductive coupling

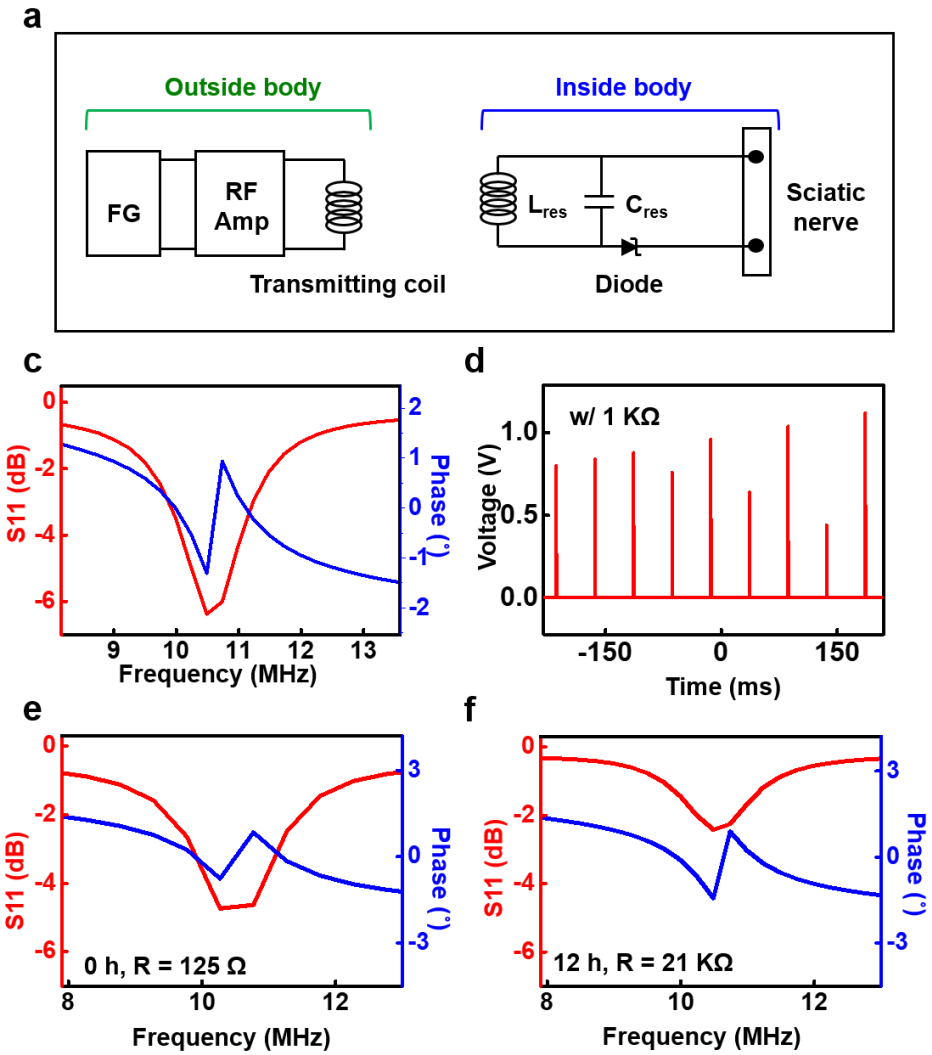

Figure 39. Performance of printed wireless stimulator (a) Circuit diagram of wireless powering system of the stimulator (b) Return loss (S11) of stimulator by frequency (c) Output voltage with pursatile transmission wave connected with 1 kohm(d,f) Return loss (S11) of non-encapsulated stimulator by incubation time in ambient condition.

3.3.1.3. In-vivo stimulaton in small / large animal

Using the previously fabricated stimulator, we first attempted to stimulate a small animal, specifically a rat. However, it was challenging to insert the stimulator into the rat's sciatic nerve due to its diameter being smaller than 3mm. To overcome this issue, we created wires by laser cutting Mo foil (thickness of 125 μm) and used them to connect the stimulator to the nerve. We confirmed that stimulation was successful, and the crucial factor at this point was the amount of current flowing through the Schottky diode. The true objective of enhancing conductivity of ZnO using conjugated molecule was aimed at improving component performance for this application. Past literature suggested that a current flow of around 25 μA was required for stimulation, which was the current amount with a load attached. As the actual tissue impedance varies significantly, ranging from 1 kohm to 10 kohms, the maximum current that could be obtained within the allowable induced voltage range had to be larger. Although there were often cases of slight trembling when the current within the diode was extremely low, a higher current was necessary for large animals with higher impedances to ensure a definite determination of stimulation presence. Consequently, we succeeded by achieving a higher current in Schottky diode.

Next, we attempted acute in-vivo wireless operation on the sciatic nerve of a large animal, specifically a canine. The surgical process involved placing the stimulator at the proximal site after transection, followed by suturing and stimulation, and then measuring electrophysiological signals. To align with the initial scenario, the external coil was designed in a shape that could be inserted into the limb, ensuring that the magnetic flux generated by the coil was parallel to the direction of the stimulator. When the external stimulation was applied at approximately 110 Vpp, with a distance of 1.5 cm from the external coil to the stimulator, at

frequencies of 10–25 MHz, and pulse durations of 200 μs with an interval of 50 ms, it was unclear whether stimulation occurred based on the measurement of compound muscle action potential (cMAP). When external stimulation was applied using a function generator at low pressures, it was observed that stimulation occurred intermittently at approximately 0.6 Vpp. Thus, it was difficult to measure cMAP at very low voltages. Increasing the external transmission did not provide clear confirmation, so compound nerve action potential (cNAP) was measured instead. When stimulated in a wired form, cNAP was found to be 3–5 times larger than cMAP, with a magnitude of approximately 3 mV. In contrast, cMAP only reached around 1 mV, indicating that it was not well observable. Several practical issues were encountered during these experiments. The encapsulation we created was unable to prevent gas permeation, leading to faster–than–expected oxidation. Therefore, we transported the stimulator to the surgical room under an N_2 gas environment. Additionally, continuous muscle stimulation sometimes resulted in situations where the stimulation presence could not be confirmed due to hysteresis.

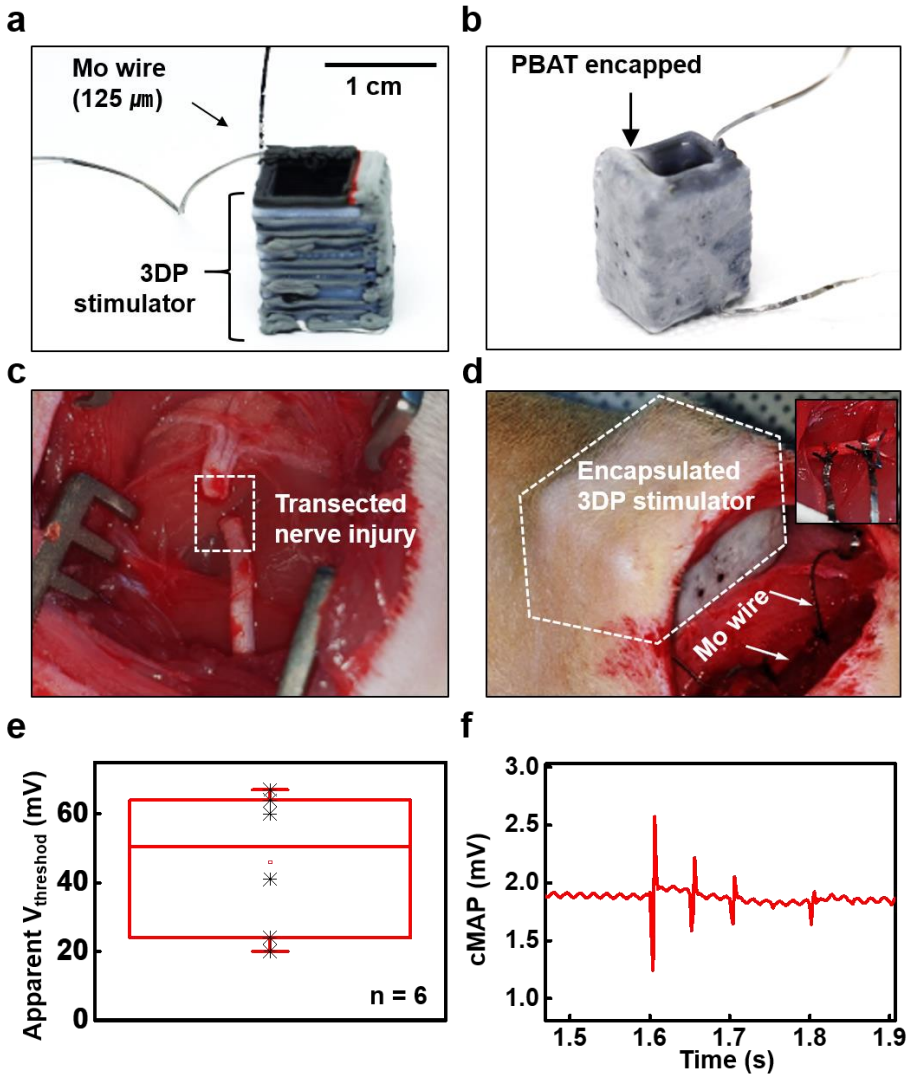

Figure 40. In-vivo wireless stimulation on small animal model (a) Printed wireless stimulator wired with biodegradable metal (Mo) wire. (b) PBAT encapsulated wired wireless stimulator (c) Image of transected sciatic nerve (d) Image of implanted stimulator interfacing sciatic nerve. Inset is nerve interfacing part with Mo wires (e) Apparent threshold voltage for stimulation on sciatic nerve (f) cMAP data by time in presence of wireless stimulation.

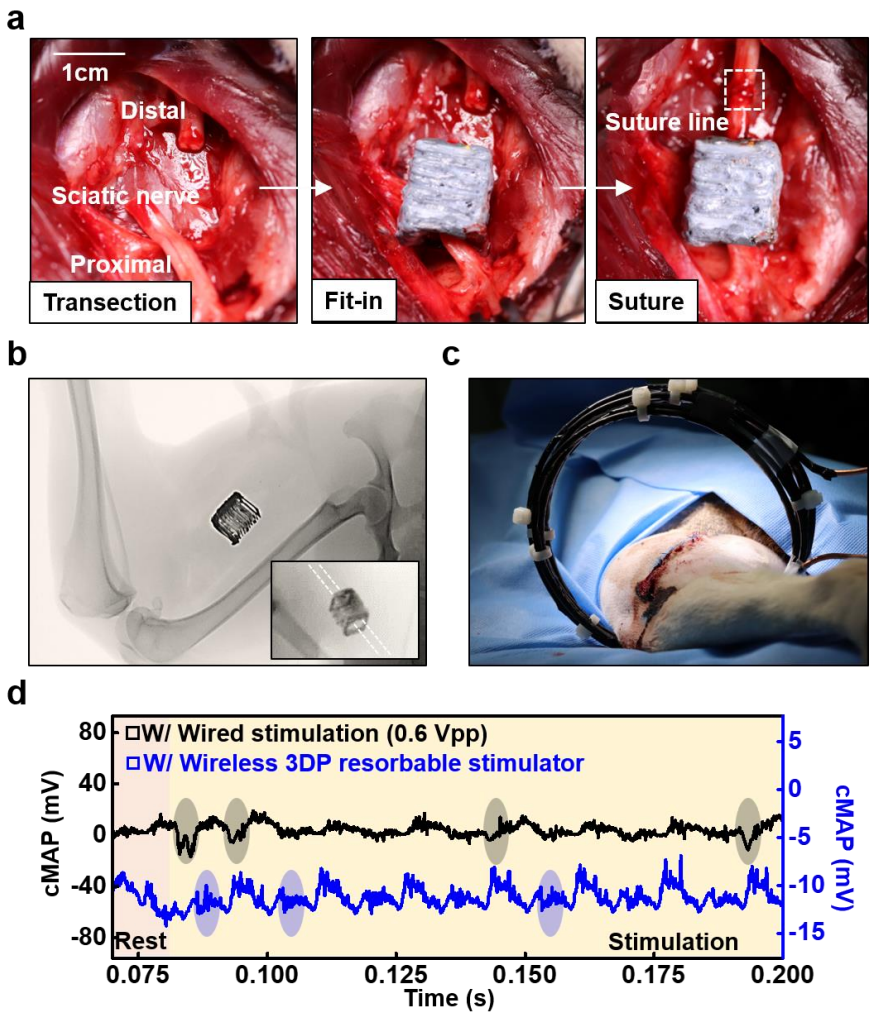

Figure 41. In-vivo wireless stimulation on large animal model (a) Serial image of surgical process of implantation of wireless stimulator to proximal site of sciatic nerve (b) C-ARM images of implanted wireless stimulator (c) Image of wireless operating system (d) cMAP data of wired stimulation and printed wireless stimulator.

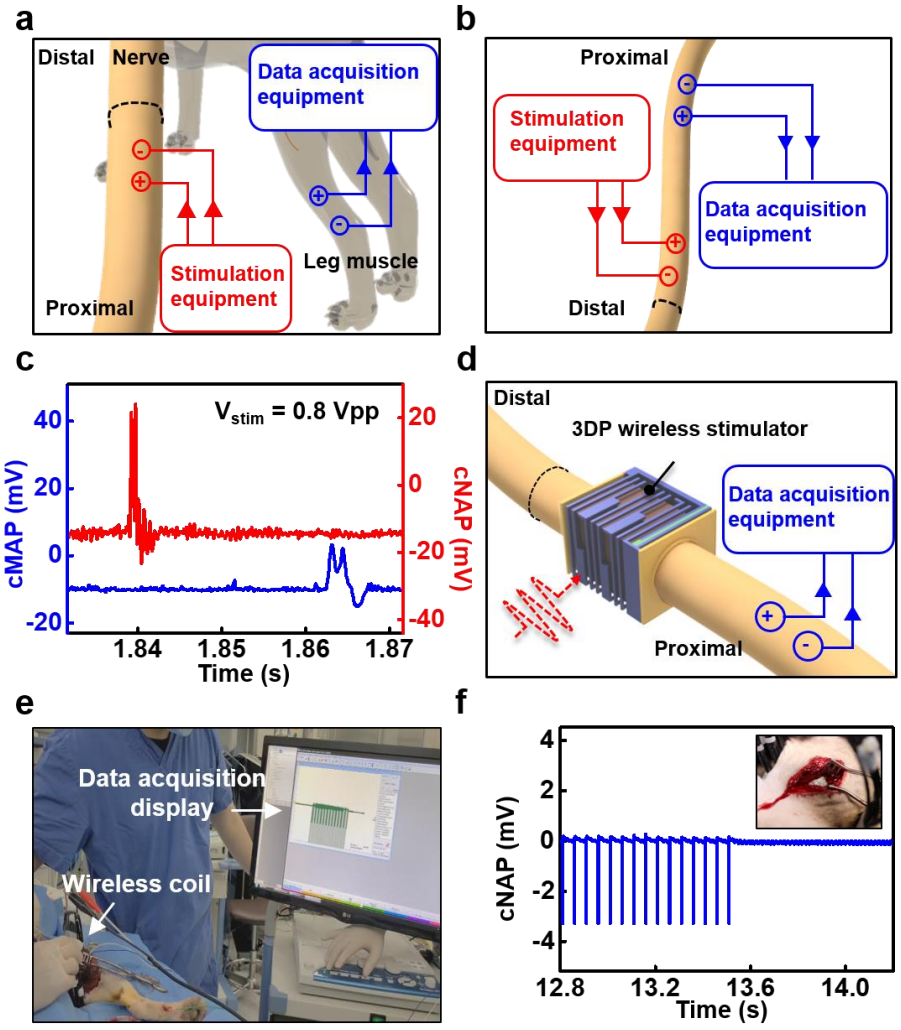

Figure 42. Verification of In-vivo wireless stimulation on large animal model. Illustration of (a) cMAP measurement (b) cNAP measurement set-up with wired stimulation. (c) cMAP, cNAP measurement with wired stimulation (d) Illustration of cNAP measurement set-up with wireless stimulation with printed stimulator (e) Image of cNAP measurement set-up with displayed detected cNAP signals. (f) cNAP data of wireless stimulation with the printed stimulator

3.3.1.4. Therapeutic effects in small animal

After confirming the applicability of wireless electrical stimulation in small and large animals, we also verified whether this wirelessly generated electrical stimulation played a significant role in nerve regeneration. We compared three groups: (1) the group where the nerve was transected and sutured, (2) the group where the transected nerve was stimulated for one hour using a non-resorbable stimulator, and (3) the group where the transected nerve was stimulated for one hour using a resorbable stimulator created through 3D printing. We examined the changes over eight weeks using cMAP and conducted a detailed analysis of the changes after eight weeks through biological tissue analysis.

Measurements were taken using immune-fluorescent staining of TUJ1 and ED1 to confirm the number of regenerated nerve fibers and immune cells in the −3mm, −1mm, 0mm, +1mm, and +3mm regions from the proximal end. The results showed no significant difference in the number of regenerated Tuj1-positive nerve fibers between the group that underwent electrical stimulation with the 3D-printed bioresorbable stimulator and the group that underwent electrical stimulation with a non-bioresorbable stimulator, indicating that the damage to the neural model was mild and already regenerated. However, staining results for CD68 (ED1) and CD86(M1 macrophage marker) showed statistically significant differences in the distribution of M1 macrophages among the transected only group(T), electrical stimulation with non-bioresorbable stimulator group(N), and electrical stimulation with 3DP-bioresorbable stimulator group(3R).

(1) −3 mm : 10.92 ± 9.34(T) ; 5.75 ± 3.59(N) ;
5.25 ± 2.99(3R),
(2) −1 mm : 52.33 ± 24.17(T) ; 39.50 ± 16.46 (N) ;
42.50 ± 23.87 (3R)
(3) 0 mm : 114.00 ± 33.95 (T) ; 106.50 ± 9.54 (N) ;

88.50 ± 32.21 (3R)
(4) +1 mm : 70.92 ± 35.02 (T) ; 51.25 ± 12.18 (N) ;
45.00 ± 8.60 (3R)
(5) +3 mm : 13.33 ± 8.23 (T) ; 8.75 ± 3.86 (N) ;
8.50 ± 3.42 (3R).

This suggests that modulation of the immune system through electrical stimulation may improve recovery outcomes more than neural regeneration alone.

To confirm functional improvement, cMAP measurement was performed each week in both the electrical stimulation conducted groups and transected-only groups, and a difference was observed at 8 weeks with primarily implanted stimulator for wireless cMAP measurements.

(1) Transected only : 3.48 ± 0.65 mV
(2) Non-bioresorbable stimulator : 6.73 ± 0.96 mV
(3) 3D printed bioresorbable stimulator : 5.70 ± 0.48 mV

There was no significant difference in cMAP measurement between the non-bioresorbable stimulator group and the 3D-printed bioresorbable stimulator group. The weight of the muscle at sacrifice immediately after 8 weeks was also significantly different among the transected only group, non-bioresorbable stimulator group, and 3D printed bioresorbable stimulator group, and the cross-sectional area of the muscle also showed a statistical difference.

Based on those biological results, we have confirmed that the stimulation from the 3D printed bioresorbable electrical stimulator can lead to a similar level of improvement in motor function recovery in cases of nerve injury compare to non-bioresorbable electrical stimulator.

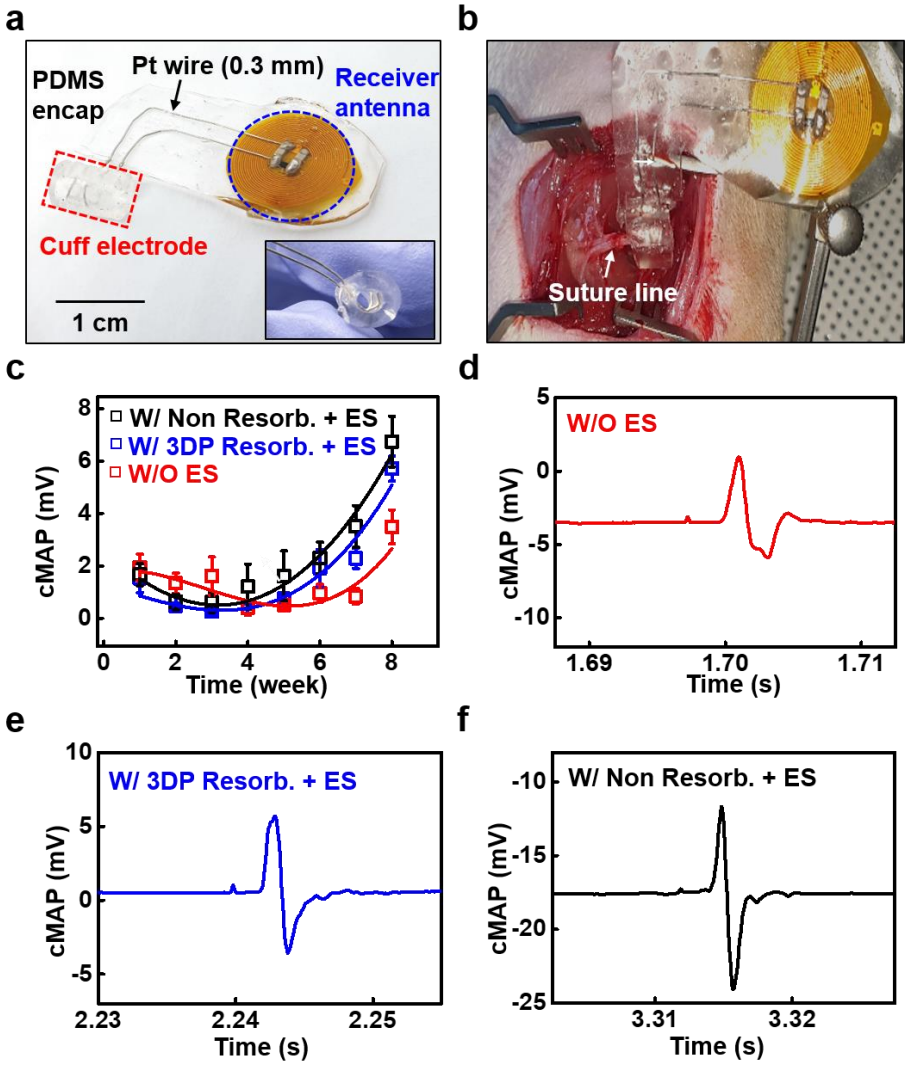

Figure 43. Therapeutic effects of printed wireless stimulator (a) Image of non resorbable Cu/PI PCB board with SMD chip based stimulator with Pt wires encapped with PDMS (b) Implantation of non resorbable wireless stimulator (c) cMAP change by weekly in 3 different groups. cMAP data of (d) transected only group (e) stimulation with printed resorbable stimulator (f) stimulation with non resorbable stimulator.

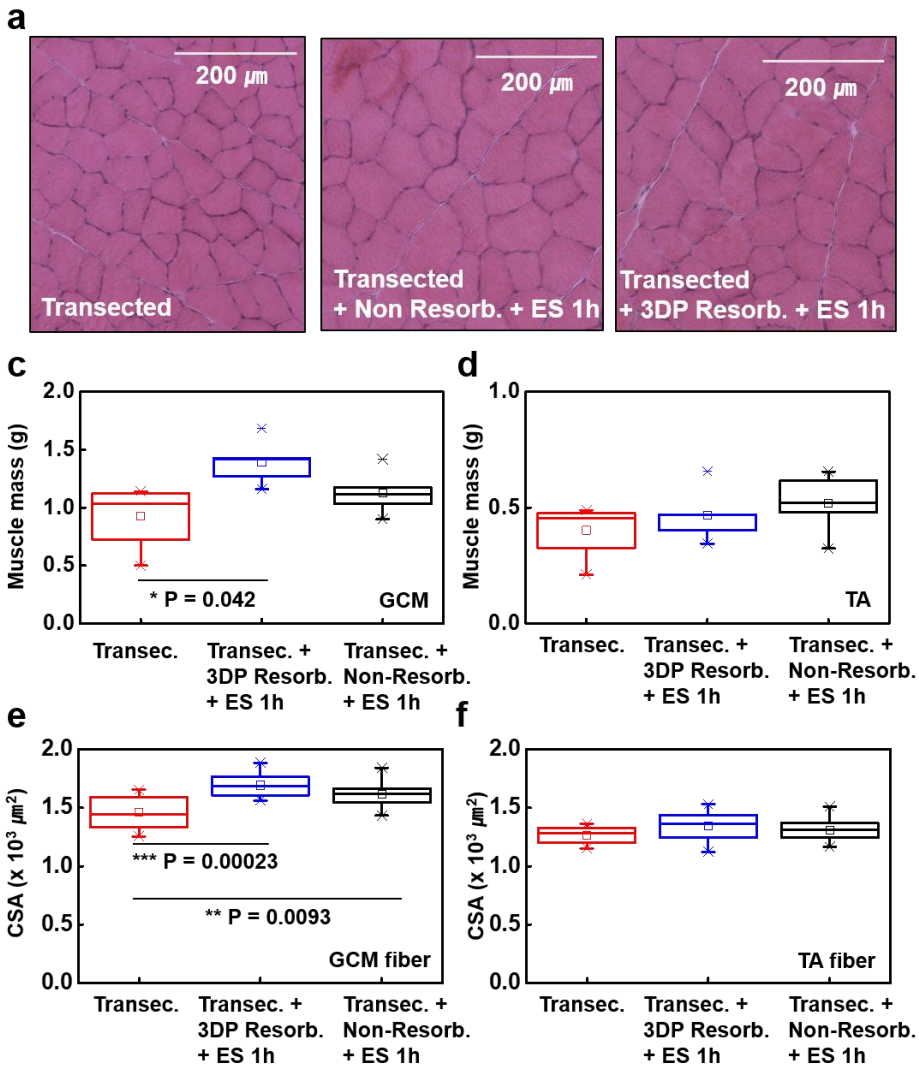

Figure 44. Muscle analysis after 8 weeks for 3 groups. (a) H&E stained cross section images of GCM fibers. Muscle mass of (c) GCM and (d) TA. Cross section area of (e) GCM fiber and (f) TA fiber (N = 4).

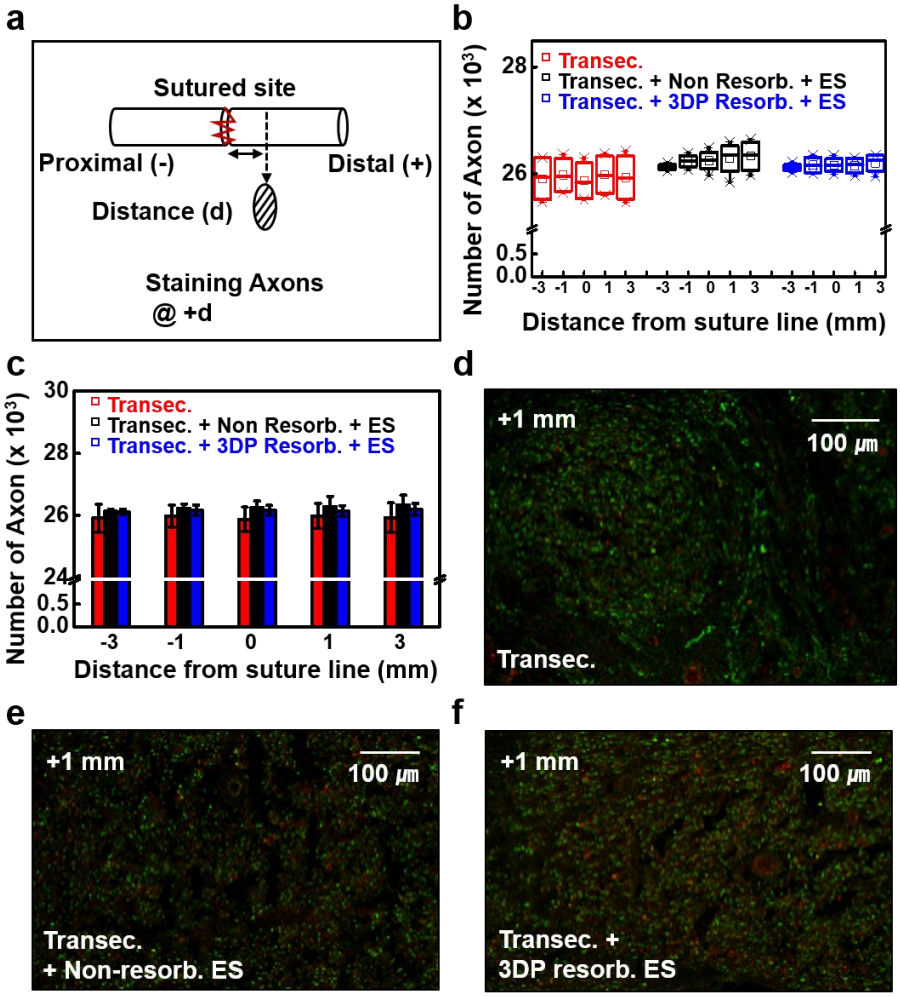

Figure 45. Nerve analysis in terms of axon regeneration after 8 weeks for 3 groups (a) Schematics of determination of distance of cross sectional images (b) Box chart for number of axons in 3 groups with box chart. Symbol 'x' is 1% and 99% of the group. (c) Histogram for number of axons in 3 groups. Stained images at +1 mm (d) transected only, (e) stimulation with printed resorbable stimulator (f) stimulation with non resorbable stimulator.

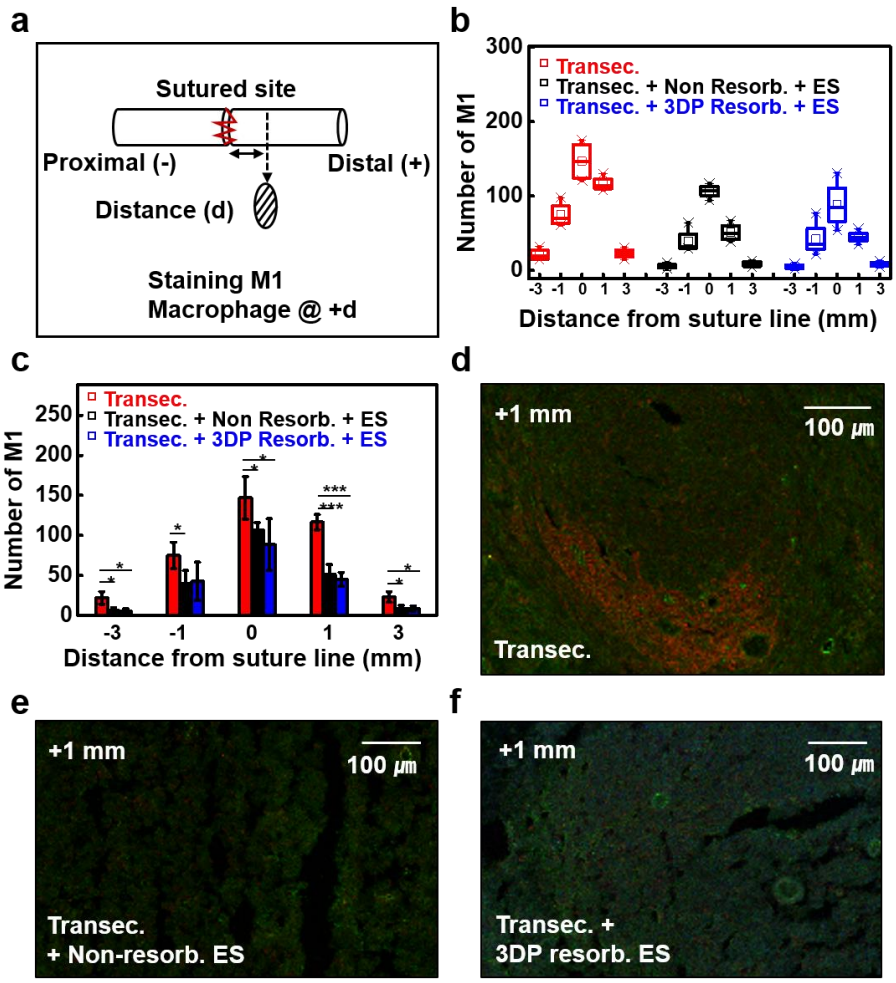

Figure 46. Nerve analysis in terms of inflammation by macrophage M1 after 8 weeks for 3 groups (a) Schematics of determination of distance of cross sectional images (b) Box chart for number of macrophage M1 in 3 groups with box chart. Symbol 'x' is 1% and 99% of the group. (c) Histogram for number of macrophage M1 in 3 groups. Stained images at +1 mm (d) transected only, (e) stimulation with printed resorbable stimulator (f) stimulation with non resorbable stimulator.

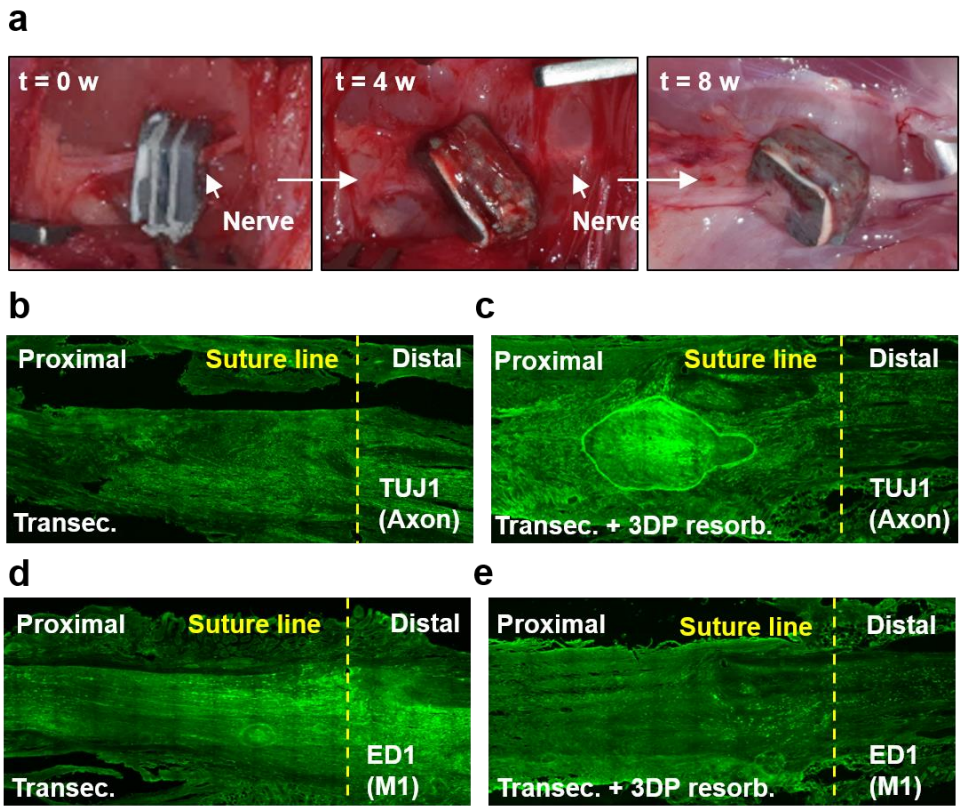

Figure 47. Biocompatibility test with stimulator interface at proximal site from suture to sciatic nerve after 8 weeks. (a) Serial images of stimulator implanted to sciatic nerve by 4 weeks (b) Sagital images of stained axons in nerve with transected only group and stimulator implanted group. (c) Sagital images of stained M1 macrophages in nerve with transected only group and stimulator implanted group

3.3.1.5. Accelerated / In-vivo degradation

Finally, we conducted evaluations to assess the degradation of the stimulator. Accelerated degradation tests and in-vivo degradation tests were performed. Each material is known to dissolve through the following mechanisms: filler materials (Zn, Mo, ZnO, Fe_3O_4, Si_3N_4) dissolve into soluble ions, hydroxides ($Zn(OH)_2$, H_2MoO_4, $Si(OH)_4$, $Fe(OH)_2$, and gases (H_2, NH_3). Matrix materials (PCL, PBAT) generate byproducts such as caproic acid, succinic acid, butyric acid, valeric acid, terephthalic acid, and adipic acids, which are excreted from the body through urine or feces. Conjugated molecules (Brilliant yellow, Indigo) directly absorb into bio-fluid or act as byproducts after being phagocytosed by macrophages. And humectants, tetraglycol or glycofurol is absorbed by body fluids [100, 116, 138-147].

The dissolution behavior of the 3D-printed stimulator (0.792 g, 3.75 cm^3) attached to a Pasteur pipette was observed in phosphate-buffered saline (PBS) under accelerated conditions (pH 6.8 – 7.8, Lipase, 45℃). The interface between the electronic ink layer and frame layers started to deteriorate at approximately 3 weeks, and the stacked layers broke down into fragments. The inorganic fillers dissolved within approximately 8 weeks, while all remaining materials disappeared after approximately 14 weeks.

For, in-vivo degradation of 3D printed stimulator was observed for 18 weeks with blood tests for verification of byproducts' biocompatibility. For pristine stimulator, it degraded slowly that still remained with main body after 18 weeks with no significant immune response while porosity addressed treated stimulator for acceleration test almost degraded after 18 weeks. Although treated stimulator showed relatively high neutrophils and low lymphocyte compared to non-implanted one, it returned to normal range after 12 weeks.

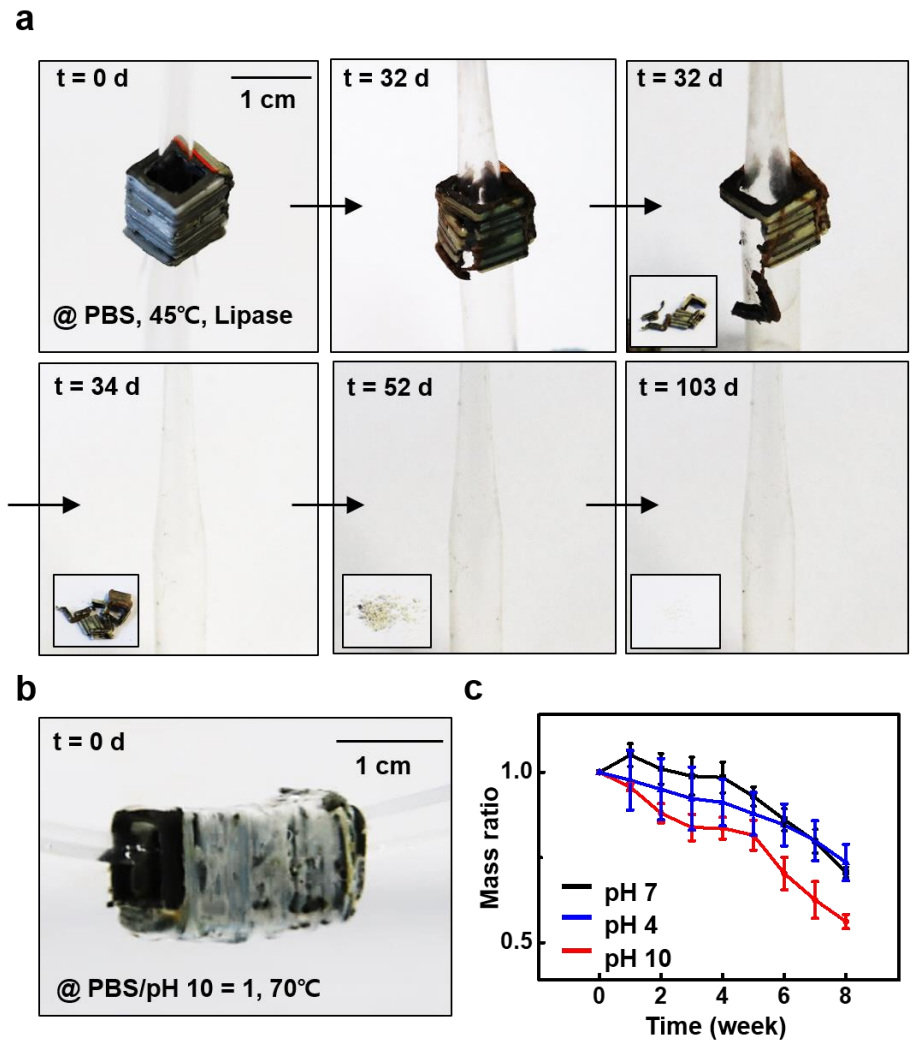

Figure 48. Accelerated degradation test for printed wireless stimulator (a) Serial images of degradation morphology of stimulator (Inner diameter 5.6 mm) fixed on Pasteur pipette in PBS, 45℃, lipase. (b) Image of encapsulated stimulator (Inner diameter 8.8 mm) fixed on PDMS structure in PBS/pH buffered solution 70℃. (c) Mass ratio of stimulator weekly by different pH in 8 weeks.

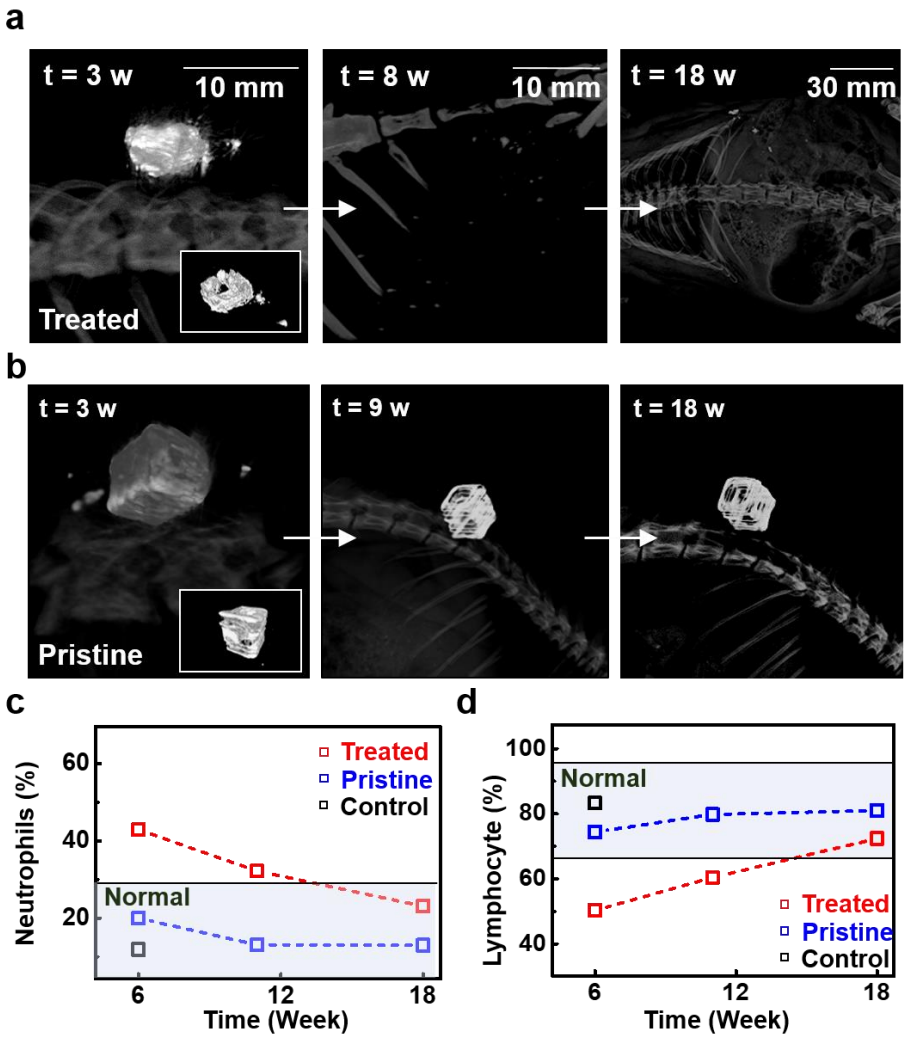

Figure 49. In-vivo degradation test for printed wireless stimulator (a) Micro CT / X-ray images of in vivo degradation of treated printed stimulator by 18 weeks (b) Micro CT / X-ray images of in vivo degradation of pristine printed stimulator by 18 weeks. Hematological test for inflammation (c) Neutrophils ratio (d) Lymphocyte ratio for treated stimulator, pristine stimulator, non-implanted control group.

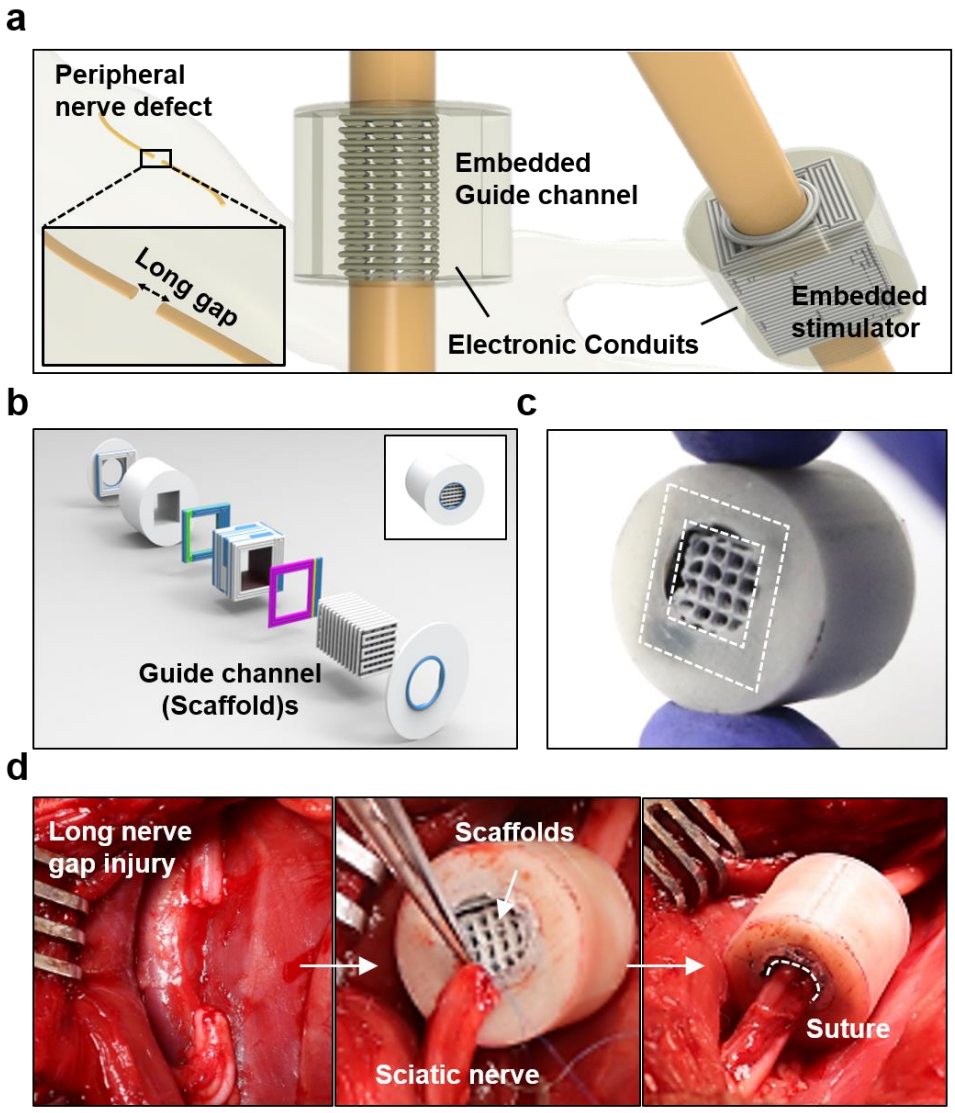

Figure 50. Extension model of stimulator to long-nerve gap injury. (a) Schematic illustration of electronic conduit including guidance channel and stimulator for long nerve gap injury (b) Exploded view of electronic conduit (c) Real image electronic conduit (d) Serial images of surgical process with electronic conduit.

Table 1. Biodegradation properties of filler and binders [100, 116, 138-148]

	Dissolution rate	Dissolution chemistry
Zn	70 ± 20 nm/h in DI 300 ± 200 nm/h in Hanks	$Zn + 2H_2O \rightarrow Zn(OH)_2 + H_2$ $Zn(OH)_2 \rightarrow Zn^{2+} + 2OH^-$
Mo	- 1±0.1 nm/h in DI 0.6 ± - 0.2 nm/h in Hanks pH 5 - 0.2 ± 0.03 nm/h in Hanks pH 7.4-8 - 0.7 ± 0.4 nm/h in Hanks pH 7.4 at 37℃	$2Mo + 2H_2O + 3O_2 \rightarrow 2H_2MoO_4$
Fe	- 1 nm/h in DI - 9 nm/h in Hanks pH 5 - 0.2 nm/h in Hanks pH 7.4-8 - 7 nm/h in Hanks pH7.4 at 37℃	$Fe + H_2O + 1/2O_2 \rightarrow Fe(OH)_2$
W	- 0.7 ± 0.2 nm/h in DI - 0.2 nm/h in Hanks pH 5 - 0.7 ± 0.2 nm/h in Hanks pH 7.4-8 - 2 nm/h in Hanks pH 7.4 at 37℃	$2W + 2H_2O + 3O_2 \rightarrow 2H_2WO_4$
Si	- 0.083 nm/h in PBS - 0.167 nm/h in PBS at 37℃	$Si + 4H_2O \rightarrow Si(OH)_4 + 2H_2$
ZnO	4.167 nm/h in PBS at 37℃	$ZnO + H_2O \rightarrow Zn(OH)_2$

SiO_2	− tg−dry $4x10^{-4}$ nm/h − tg−wet $1.2x10^{-4}$ nm/h − PECVD $4x10^{-3}$ nm/h − e−beam 0.4 nm/h In PBS at 37 ℃	$SiO_2 + 2H_2O \rightarrow Si(OH)_4$
MgO	~ 133 nm/h in DI	$MgO + H_2O \rightarrow Mg(OH)_2$
Si_3N_4	− LPCVD $6.7x10^{-3}$ nm/h − PECVD 0.035 nm/h in PBS at 37℃	$Si_3N_4 + 12H_2O \rightarrow 3Si(OH)_4 + 4NH_3$
Fe_3O_4	− 30 μm long − Gelatin methacryloyl composite in 4 μg/mL MMP−2, took 5h.	$Fe_3O_4 + 3H_2O + 1/2O_2 \rightarrow 3Fe(OH)_2$
PBAT	Remaining weight 0.8125 % / day in DI at 70℃	Ester bond hydrolysis
PCL	Molecular weight degradation rate 0.001 / day in PBS at 37℃	Ester bond hydrolysis

Table 2. Biocompatibility of conjugated molecules [142-147]

	LC50
Tetraglycol	Hematological analysis RBC: 103% viability WBC: 74% viability PLT: 67% viability at 70 μl / 5-7 ml after 30 days
Curcumin	NIH3T3 cell 35% cytotoxicity 40 nmol/ml after 24h
Indigo	Keratinocytes 52.94% cell viability at 500 μg/ml after 24h
β-Carotene	HEK 293 cell 67% cell viability at 80 μg/ml after 72h
Indigo carmine	Human foreskin fibroblasts 55% cell viability at 500 μg/ml after 24h
Brilliant yellow	PC12 cell > 90% cell viability at 300 μM after 36h 37℃
Solvent Green 3	MCTT HCE^{TM} model test by UPLC-UV 113.1 % cell viability at 44.4 mg/ml after 24h
Guanine	One of nucleobase materials in DNA / Nucleotide = Phosphate, Sugar, Base

3.3.2. Plug-in EcoG sensor

For cases involving penetration contact, we contemplated strategies for integrating sensors or transducers into the structure in a minimally invasive manner, allowing for high space utilization and integration. We considered approaches such as embedding them within the structure, similar to microneedles, which can be produced in a wearable form with low pain. However, we also explored the possibility of penetrating deep tissue areas to establish contact for measurements. Additionally, since the integration of degradable memory or processing units is still a challenge, we focused on sensors with 3D transducing situations as a potential solution. In the case of transcranial implants, we envisioned creating a portion within a specific area that could measure temporary changes and heal along with degradation, similar to how wound healing occurs.

3.3.2.1. Design and fabrication

The design allowed for the placement of electrode components for interfacing with the left and right motor cortex, as well as reference electrodes, in a plug-in structure that could make contact with the brain surface. Transducers were arranged in three-dimensional space to enable wiring of each electrode, forming a bundled configuration with intersecting pathways. Given that it was intended for application in small animals, the distance between the electrodes was set to be less than 5 mm, and the diameter of the electrodes was designed to be less than 3 mm. Zinc ink was used for the electrodes, while PLA was used as the external frame material. To ensure proper infiltration within PLA, sintering was carried out for 5 hours. The sintering time was empirically determined to achieve resistance under ~10^2 ohm, but it can be also determined through previous reactive diffusion modeling. Upon performing X-Ray imaging after fabrication, it was confirmed that the intersecting on the XY plane but separated along the Z-axis.

3.3.2.2. In-vivo sensing in small animal

To place the fabricated plug-in EcoG sensor on the surface of the rat's brain, the skull surface was carefully drilled to expose the dura or brain surface, allowing for precise positioning. Once the desired exposure was achieved, the EcoG sensor was plugged in on top. To ensure optimal contact, conductive gel was applied to the electrode surface. A nerve stimulation was performed on the left sciatic nerve, and the EcoG results were observed. It was found that there were changes only in the right motor cortex region during stimulation, confirming that the sensor and transducer could be used to read electrophysiological signals.

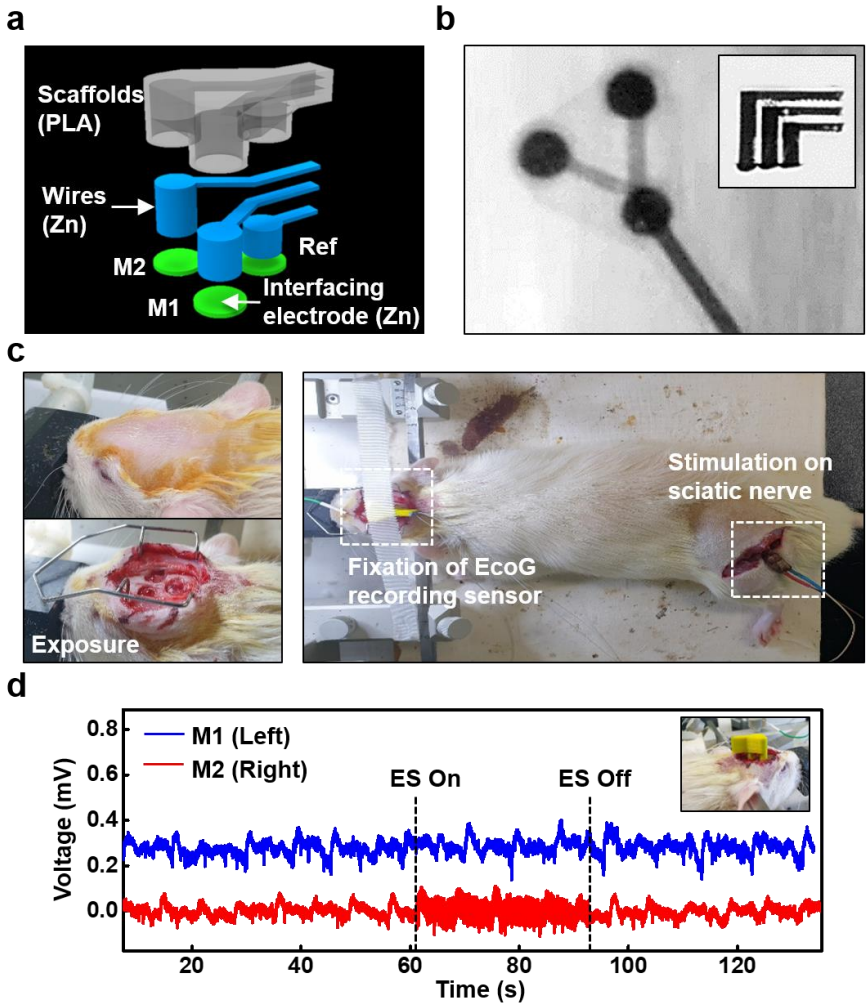

Figure 51. Structure and in-vivo experiments with plug-in type EcoG senor. (a) Exploded view of plug-in type EcoG sensor (b) X-ray images of the sensor from bottom view. Inset is side view of the sensor. (c) Images of surgical process of brain surface exposure (left) stimulation process (right) (d) EcoG signals measured from two electrodes M1, M2 on motor cortex under certain period of stimulation in real-time.

3.3.3. Wireless bone sensor

One of the advantages of 3D printing is the ability to contemplate contacting or penetrating complex surfaces of bio constructs to obtain internal information. Inspired by the idea of adding function to a structure that was previously used solely as a structural support implant, the concept of a smart implant emerged. This concept has recently been discussed in the context of bone implants with the aim of continuously monitoring mechanical properties and providing patient care through feedback[149, 150]. In this scenario, a wireless monitoring system could be designed to measure osseointegration, alignment, and other factors when biodegradable implants are placed in bone defect areas[151]. If measurements related to chemical and bioanalytes are also possible, it could enable monitoring of the initial bond between the implant and the bone. With this motivation, the implant was fabricated, and for future experiments, high-resolution production is planned to conduct in-vivo experiments.

3.3.1.1. Design and fabrication

There are various methods for wireless reading of pressure or strain. (1) Connecting a resistor and a wireless chip (RFID or Bluetooth)[152], or (2) connecting a chipless surface acoustic wave system based on piezoelectric materials for measurement[152], or (3) utilizing a chipless LC circuit-based variable capacitance method[152]. Among these methods, for chipless fabrication using the previously developed ink, an LC circuit-based monitoring approach was chosen. Therefore, a capacitive-type sensor capable of sensing pressure and an inductor capable of wirelessly reading the sensor were fabricated. All of these components were designed to be embedded within the scaffold, which serves as the framework of the bone implant, allowing simultaneous 3D printing. To enhance the sensitivity of the

capacitor, a trench structure was created, and polymer printing conditions were optimized to achieve self-supporting features. The distance between the electrodes was set to be around 1 mm. For the inductor, a core of Fe_3O_4 was used, and a double coil configuration was implemented. Since sintering was not feasible, a highly conductive ink without sintering, such as Mo ink, was utilized as the conductor.

3.3.1.2. Performance

It was observed that the trench structured capacitor exhibited a change in capacitance from approximately 1 pF to 1.5 pF when subjected to repetitive 1 MPa pressure at a frequency of 1 MHz. When connected to the inductor, a resonant frequency of around 610 MHz was confirmed. Placing weight on the sensor resulted in a shift towards lower frequencies in the resonant frequency spectrum. The rate of change in resonant frequency varied depending on the presence of the scaffold on top of the sensor. Without the scaffold, the rate of change was −0.192 MHz/g, whereas with the scaffold, it was significantly lower at −0.0135 MHz/g. The interpretation of these results suggests that energy dissipation occurs within the scaffold, resulting in minimal stress transmission and deflection on the capacitor, thereby leading to a smaller change in capacitance. Further quantification on the infill and thickness of the scaffold placed on top of the sensor will be conducted.

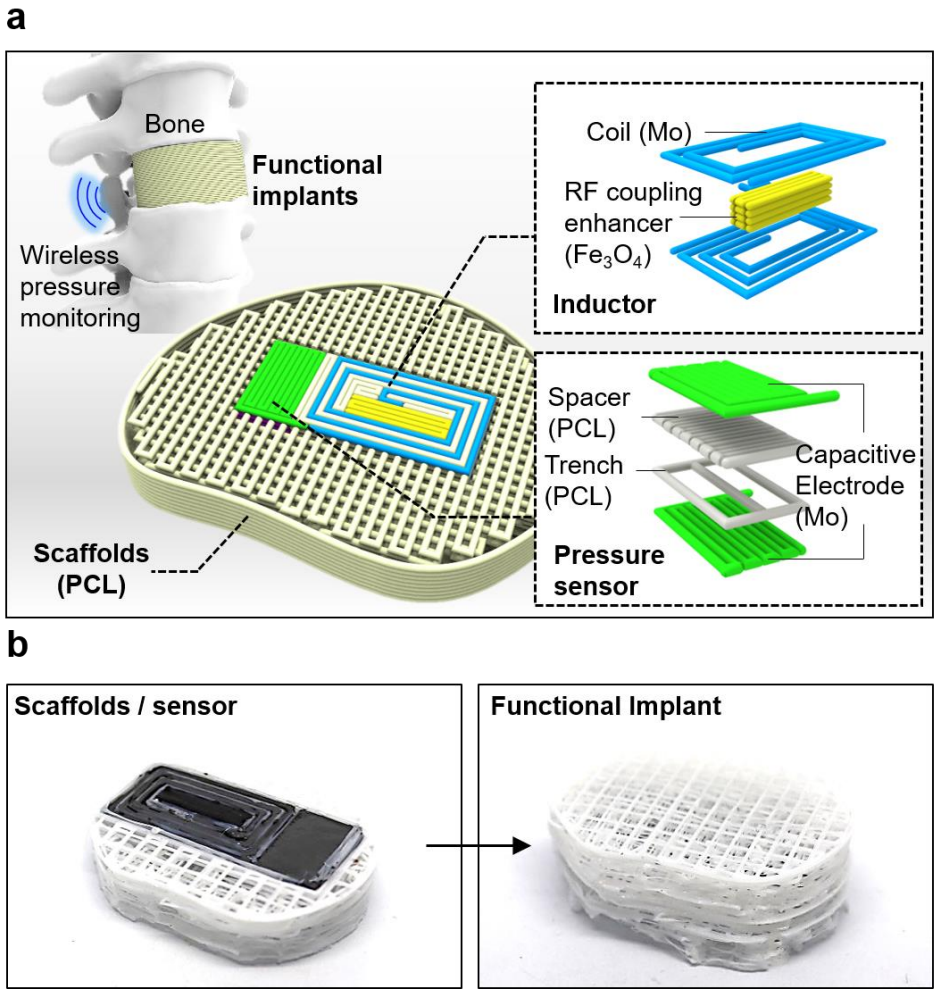

Figure 52. Concept and structure of wireless bone sensor (a) Schematic illustration of wireless bone sensor with embedded inductor and capacitive pressure sensor in scaffolds for bone defects. (b) Serial images of printing sensors and inductors monolithically in scaffolds.

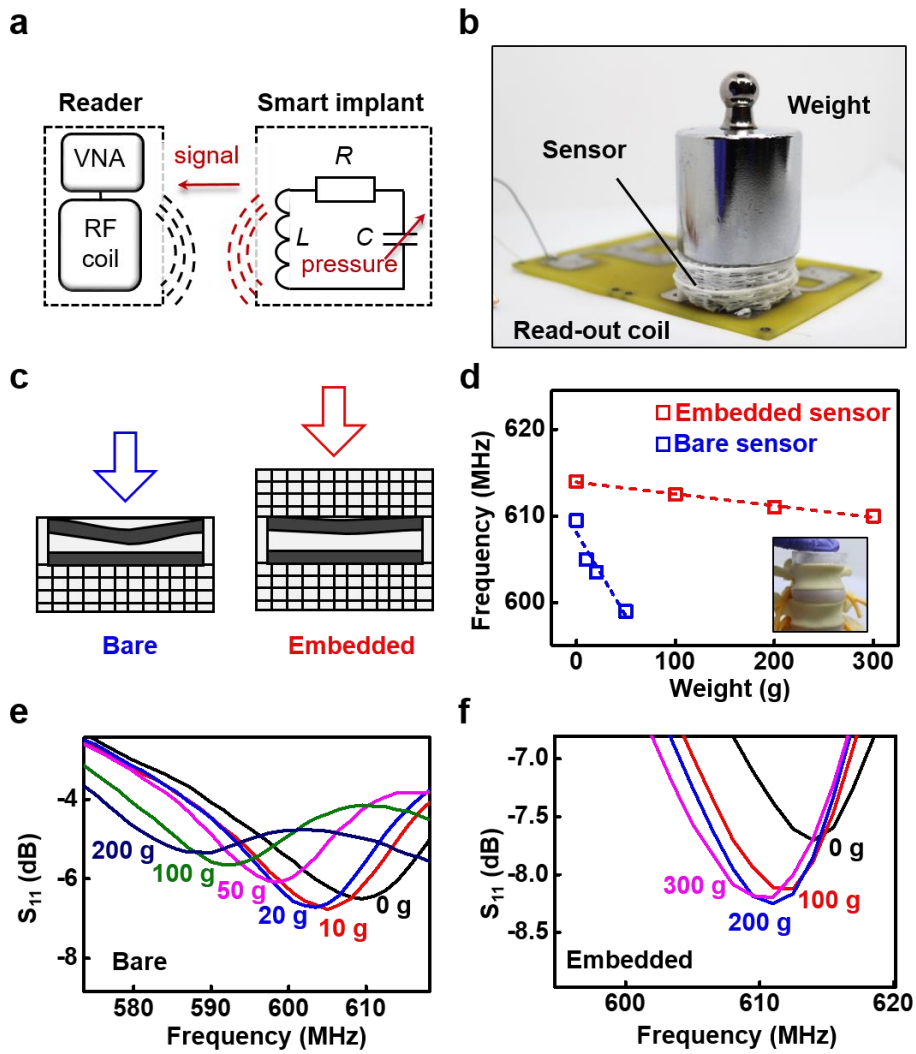

Figure 53. Performance of wireless bone sensor (a) Circuit diagram of wireless read-out system (b) Image of wireless read-out system with external load (c) Schematic differences to same loads with bare sensors and embedded sensors (d) Resonant frequency change by weight on bare and embedded sensors (e) S_{11} change by weight on bare sensor (f) S_{11} change by weight on embedded sensor

3.4. Conclusion

Based on the biodegradable electronic ink and components developed in Chapter 2, various devices capable of conformal contact such as surrounding contact, penetration contact, and embedded contact were developed, enabling the application of wireless electrical stimulation, 3D organized transducers, and wireless pressure monitoring. Animal experiments were conducted as part of translational studies. For the wireless electrical stimulator, a strategy was developed to customize the integration of RF rectifiers, antennas, and other components into conduit-like structures. Based on this strategy, fully printed devices were post-treated and validated for their stimulation capabilities through in-vivo experiments in small and large animals. The effectiveness of stimulation was verified through various biological validations, and the accelerated and in-vivo degradation scenarios were examined, confirming the biocompatibility of the decomposed byproducts. Additionally, plug-in form EcoG sensors were fabricated, demonstrating their feasibility for real-time measurements, and wireless pressure sensors were developed, allowing wireless readouts based on external pressure or force.

Chapter 4. 3D printed expandable electronic system

4.1. Motivation

In Chapters 2 and 3, we conducted research on 3D printing techniques for customized fabrication in three-dimensional space, and progressed to pre-clinical studies. While conformal contact and space utilization are important in the real world, stability in the face of multidimensional deformation, such as expanding scenarios, is also crucial. Therefore, we aimed to implement components that maintain stability even in custom situations with deformation by using elastomeric materials. We wanted to explore the use of biodegradable elastomers, but the known elastomer, PGS polymer, required complex processing and better to be fabricated in a photocurable form. We also considered using biodegradable hydrogels like gelatin, but the biodegradable fillers in the matrix degraded due to water molecules, so we aimed to develop components that exhibit stable electrical properties in a non-degradable version of an expanding structure.

During multidimensional deformation, the cross-sectional area of the wires decreases, resulting in increased resistance and decreased stability of the overall electronic components. This is a problem caused by the elastic limit of the material, requiring a structural solution. In order to achieve stability even in expanding scenarios, we considered using a meta-material with a negative Poisson's ratio[153-157]. There have been previous attempts to address this issue using negative Poisson's ratio, primarily through two methods: (1) molding or coating the entire auxetic structure with conducting materials[158-162], and (2) fabricating a substrate of an auxetic structure and patterning a conducting line on top[163-165]. However, method (1) lacks design freedom for conducting parts, while method (2) results in a volumetrically

inefficient architecture due to stacking electronics, and adhesion needs to be carefully considered. Therefore, we aimed to create substrateless expanding electronics by segregating structural and electronic components within a singular stereographic entity using multi-material printing. This novel approach can potentially offer greater possibilities for structural electronics.

For the 3D printable structural frame materials, we chose room-temperature vulcanizing (RTV) silicone, a widely commercialized silicone elastomer used for adhesive sealants. Various types of RTV silicone for specialized purposes are already available in the market, and it possesses viscoelastic properties suitable for 3D printing, with self-supporting characteristics[166]. As for the conducting fillers, we considered using Ag flakes due to their higher conductivity compared to non-noble metals like Cu or carbon-based conductors such as carbon nanotubes and carbon black. The planar structure of Ag flakes (2D) can create better percolation networks than spherical (0D) or wire-like (1D) structures[80, 162].

4.2. Materials and methods

4.2.1. Preparation of soft electronic ink

RTV silicone (Permatex, Illinois, USA), Ag flakes (4-8 μm, Alfa Aesar, Massachu-setts, USA), and 4-methyl-2-pentanone (TCI, Tokyo, Japan) were placed in a mixing container, based on the experimental conditions for the desired volume fractions. The mixture was placed in a mixer (ARE-310, THINKY, Tokyo, Japan) and evenly mixed, using the planetary centrifugal mixing mode, at a rotation speed of 2000 rpm for 4 min. The Ag-RTV mixture was used to fabricate the structure using a 3D printer (BIO X, Cellink, Gothenburg, Sweden). Thereafter, the resulting structure was placed in a 120 °C oven for 2 h to evaporate the lubricant. Finally, the production of the sample was completed by allowing the Ag-

RTV to cure overnight in ambient conditions (~25 ℃).

4.2.2. Characterization of electrical properties of ink

The samples for the conductivity measurements were also fabricated via a 3D printer as aforementioned for feature size measurements, while resistance was measured using a digital multimeter (DMM). The conductivity was calculated using the measured resistance value and the dimension of the sample.

4.2.3. Characterization of rheological properties of inks

MultiDrive rheometer (MCR 702e, AntonPaar, Graz, Austria) was used to discern the intricate rheological properties of the ink samples. The inks were carefully placed in a confined space between two plates with a precise gap of 0.5 mm. The sweep mode of the rheometer was used to accurately quantify the viscosity of the inks, covering a variety of shear rates from 0.1 to 100 s^{-1} at a constant temperature of 25℃. Additionally, the amplitude mode of the instrument was used to assess the storage and loss shear modulus, encompassing a broad range of shear strain from 0.01 to 10% and an angular frequency of 10 rad/s. Samples for the feature size measurements were pro-duced using a 3D printer (Cellink, BIO X, Sweden) and printing was performed at var-ious speeds ranging from 1 mm/s to 6 mm/s at 70 kPa (RTV) and 60 kPa (Ag-RTV).

4.2.4. Characterization of mechanical properties of inks

To analyze the mechanical properties of the RTV and Ag-RTV composites, uniaxial tensile tests were executed using an Instron 3343 universal testing machine (Instron, USA) at a fixed receding strain rate of 100%/min. For the electromechanical properties measurements, samples were prepared by placing 3D-printed Ag-RTV on a Cu tape fragment, followed by multiple layers (10 – 15)

of protection tape covering the Ag-RTV and Cu tape to prevent resistance changes in the contact area by jig. Then, cables were connected to both sides of the Cu tape and the cable was connected to the DMM. The strain changed from 0% to 100% in 5% intervals and resistance was measured at each fixed strain point with the DMM.

4.2.5. Design and multi-material printing of inks

The process of modeling the intricately shaped, bespoke components was meticu-lously executed using the computer aided design (CAD) software (Fusion 360, Autodesk, San Francisco, USA). Thereafter, the 3D models were sliced by slicer program (Repetier-Host, Hot-World GmbH & Co. KG, Willich, Germany) which enabled the genera-tion of a G-code that was customized to the specific shapes of the components. The G-code was carefully fine-tuned, which reduced the printing time. Furthermore, the finely tuned G-code was transferred to the 3D printer (BIOX, Cellink, Gothenburg, Sweden), which is equipped with three nozzles that are capable of simultaneously printing three different materials. The substrate was covered with polypropylene to prevent adhesion after curing. Speed and pressure were modified at various speeds ranging from 1 mm/s to 10 mm/s and at 60-100 kPa.

4.2.6. Measurement of electronic components performance

An LCR meter was used to measure the capacitance of the sensors and the inductance of the printed inductor. Also resistance measurement for pneumatic actuator integration was also done with real-time DMM (NI instruments). Capacitance data were smoothed using the Origin program, with a percentile filter (points of window = 5, boundary condition = none, percentile = 65).

4.3. Results and discussion

4.3.1. Strategy for expandable structural electronics

A hyperelastic RTV silicone elastomer was utilized as the frame material, especially rRTV for the control frame in the structural electronics and sRTV for pneumatic actuators. RTV silicones involve a condensation reaction between a base polymer with reactive groups and a curing agent that acts as a catalyst to promote cross-linking at room temperature after printing, resulting in a cured silicone rubber material[167-170]. A stretchable conductor was used for the electron conduction pathway and was composed of Ag flakes and sRTV, with 4-methyl-2-pentanone as a lubricant. Here, 4-methyl-2-pentanone provided excellent dispersion of the Ag flakes in the sRTV, allowing excellent electron current flow through a percolation path of well-dispersed Ag flakes and adequate viscoelastic properties for 3D printing. Using rRTV and Ag-RTV within microstructures having a negative Poisson's ratio can provides stable electrical performance under expanding deformation.

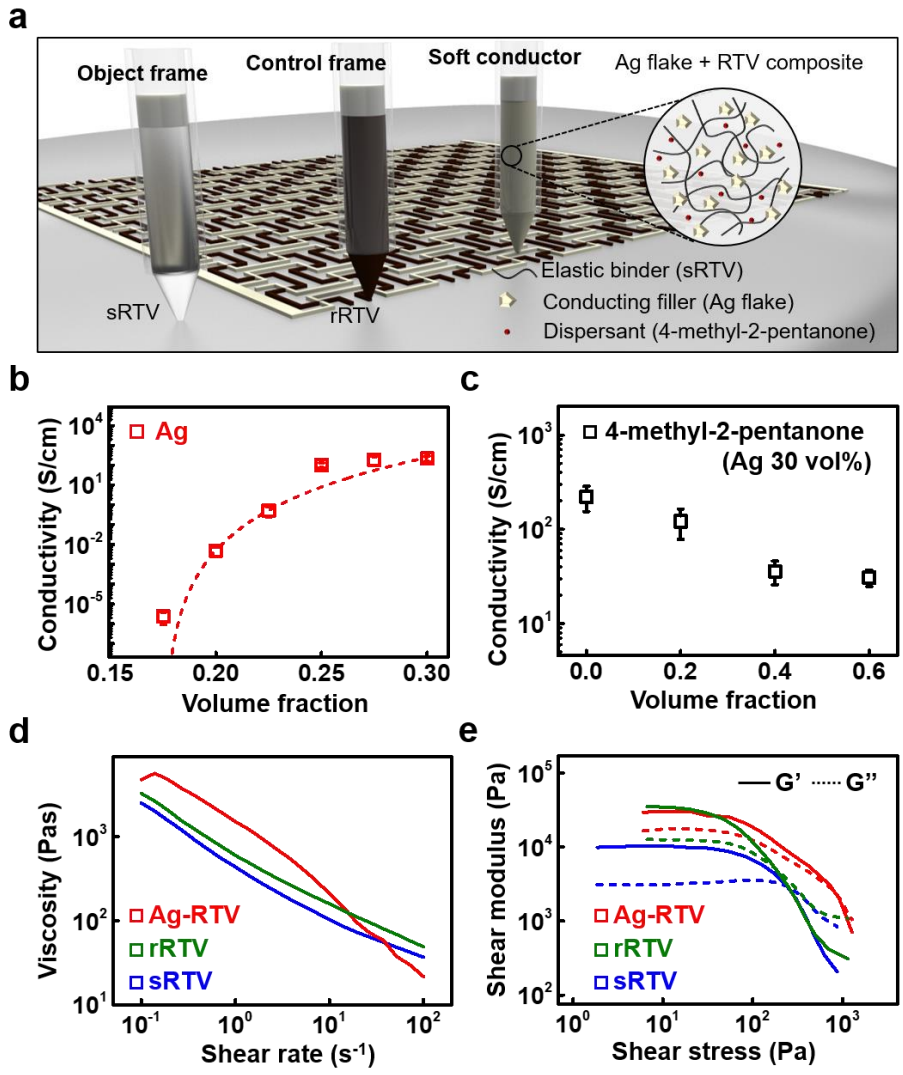

Figure 56. Concept of expandable electronic system and electrical, rheological properties of inks. (a) Schematic illustration of multi-material printed expandable electronic system with control frame (rRTV) soft conductor (Ag-RTV) with object frame (sRTV). (b) Conductivity of Ag-RTV by volume fraction of Ag flake (c) Conductivity of Ag-RTV by volume fraction of dispersant (4-methyl-2-pentanone) preserving Ag/RTV ratio (d) Viscosity by shear rate of Ag-RTV, rRTV, sRTV (e) Shear modulus of Ag-RTV, rRTV, sRTV by shear stress .

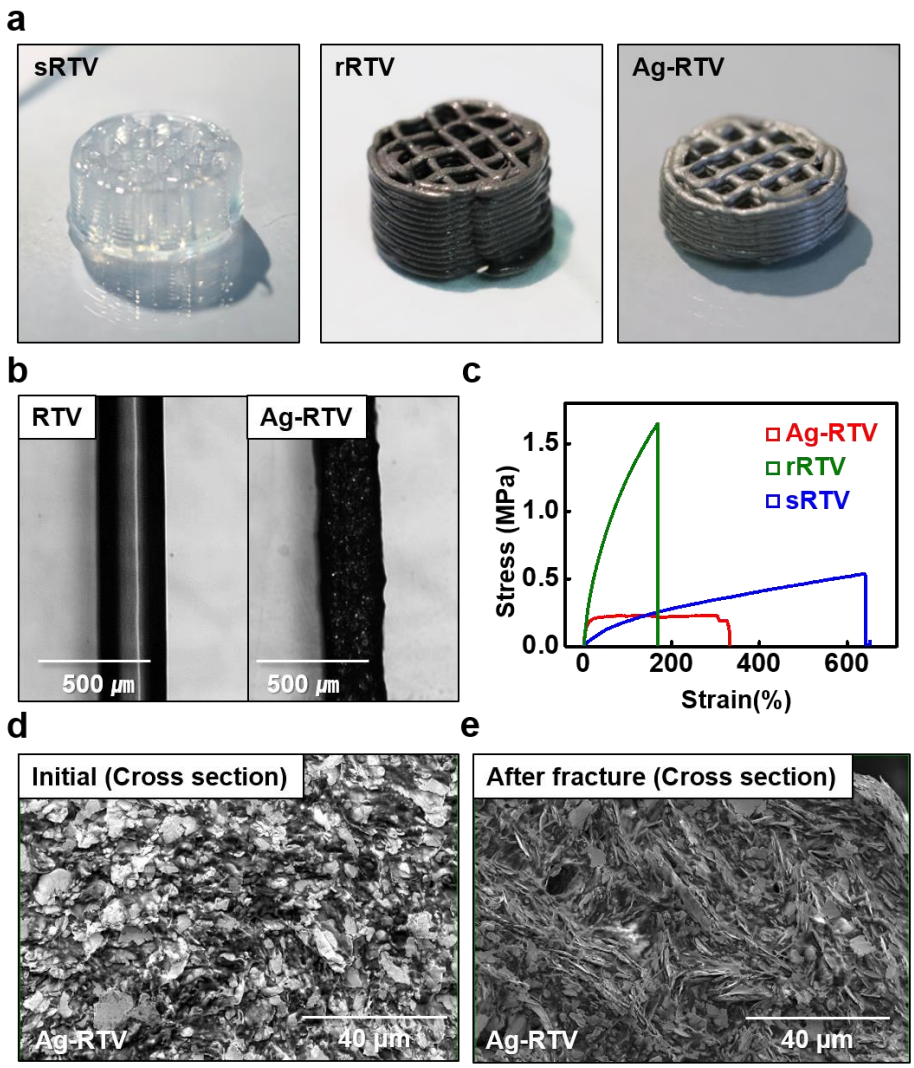

Figure 57. Printed images and mechanical testing of sRTV, rRTV, Ag-RTV. (a) Printed scaffolds with sRTV, rRTV, Ag-RTV (b) Optical image of printed line of RTV, Ag-RTV (c) Stress-strain curve of Ag-RTV, rRTV, sRTV. SEM images of cross sectional image of Ag-RTV (d) initial state (e) after fracture.

4.3.2. Electrical properties of ink

Addition of Ag flakes to the sRTV at various volume fractions for optimizing the conductivity of Ag-RTV was conducted. Furthermore, a percolation threshold was observed at a volume fraction of 17.5% in Ag-RTV, confirming the rapidly increased conductivity. Furthermore, the higher the volume fraction of Ag flakes, the greater the percolation path, resulting in ~10^4 S/m conductivity, becoming saturated after a volume fraction of ~30%.

In the Ag volume fraction range in Ag-RTV where conductivity was high, printability was not optimal. To maintain conductivity while reducing yield shear stress, lubricant was introduced. To aid the dispensing of Ag flakes in the sRTV silicone, 4-methyl-2-pentanone was used as a lubricant, which blends well in silicone elastomers[171]. Dispensed line structures, including Ag flakes and various 4-methyl-2-pentanones in sRTV, underwent lubricant vaporization at 120 ℃, and the resulting conductivity was measured at room temperature. Despite the increase in the lubricant-reduced conductivity of Ag-RTV, ~3000 S/m was reached at a 40% lubricant percentage, which is applicable for electronics. After the lubricant dried out, the ratio between the Ag flakes and sRTV became 31 vol% and 69 vol%, which showed good conductivity previously.

4.3.3. Rheological properties of ink

Ag-RTV with a volume fraction of 40% of lubricant showed excellent dispensing through the nozzle without clogging, and the dispensed line also stacked well. Showing 3D printability with a securing conductivity condition for 3D printable Ag-RTV was determined as [Ag flake: sRTV: 4-methyl-2-pentanone = 18:40:42] in the volume fraction. Rheology of Ag-RTV, sRTV ink was then quantitatively measured. The viscosity at a shear rate of $10s^{-1}$ was 210 Pas and 103 Pas, while the yield shear stress was 2.6 Pa and 1.01 Pa for Ag-RTV and sRTV, respectively, which

showed a shear thinning behavior applicable for 3D printing under low pressure (< 100 kPa). Diverse feature size could be obtained with various printing speed under Ag-RTV and sRTV at the minimum dispensing pressure (Ag-RTV, 90 kPa; sRTV, 80 kPa) with a 27-gauge conical nozzle. Feature size was optimized to 400 μm for each ink.

4.3.4. Mechanical properties of ink

sRTV exhibited hyperelastic mechanical properties with an elastic modulus of 83.59 kPa and a fracture occurring at a strain of approximately 650%. The Ag-RTV exhibited a reduced elastic range of approximately 20% and a fracture occurring at approximately 350% strain with higher modulus of 708.2 kPa, which was attributed to the reduced volume of sRTV and increased stress points due to the addition of the Ag flakes and lubricant. rRTV exhibited elastic modulus of 977.1 kPa and a fracture occurring at approximately 150% which has similar modulus with Ag-RTV compare to sRTV. By observing SEM image of Ag-RTV before and after fracture, linear alignment and the partial agglomeration of Ag flakes were observed after fracture, indicating the migration of Ag flakes owing to external mechanical force.

4.3.5. Mechanical properties of missing rib structure

The geometrical determination of the unit cell of the structure, both missing rib and modified missing rib forms was conducted. The distance (r) of the pattern was 2.121 mm and the pattern feature size was 0.4 mm. Three types of expandable structure arrays, which are composed of simple unit cells were tested. Each pattern type was photographed using a DSLR camera equipped with a macro-lens, with the structure changing as the engineering strain increased from 0 to 20% along the x-axis at 2.5% intervals. A marker was placed at the 1/4, 2/4, and 3/4 positions on the y-axis to enable the calculation of the change in engineering strain using

Image J software (National Institutes of Health, Bethesda, USA), while the average and standard deviation are displayed on a graph.

The Poisson's ratio of pattern type 1 changed from −0.1448 (2.5%) to −0.0185 (20%), while for pattern type 2, it appeared to be maintained at −0.3. The Poisson's ratio of pattern type 3 decreased overall, with the absolute value of the Poisson's ratio increasing from −0.452 (2.5%) to −0.6 (15%) and converging to −0.457 (20%). When sRTV and rRTV were used, respectively, in pattern type 1 to measure the Poisson's ratio with strain dependency, the Poisson's ratio had a positive value (an average of ~0.05), according to the vertical strain in the case of sRTV. Therefore, the spring constant of sRTV for the auxetic effect was not appropriate, while the moduli of Ag−RTV and rRTV were similar and could provide auxetic effects.

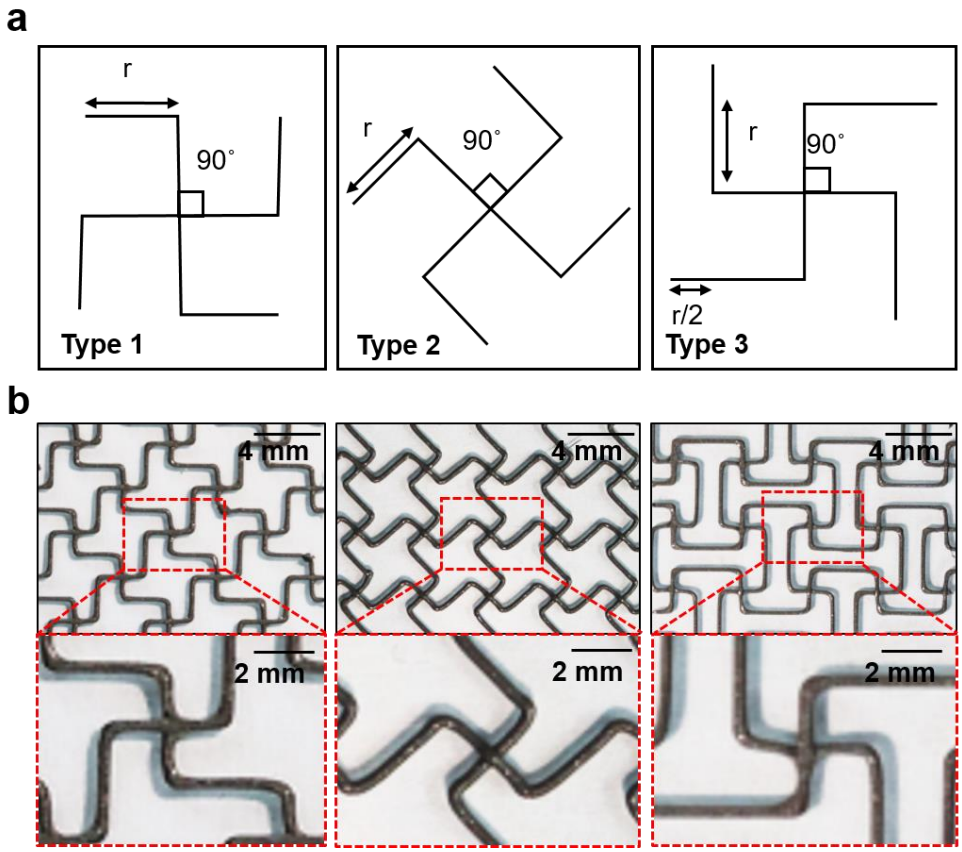

Figure 58. Design of missing rib structure (a) Geometrical design of 3 types of missing rib structure unit (b) Images of array of missing rib structure units

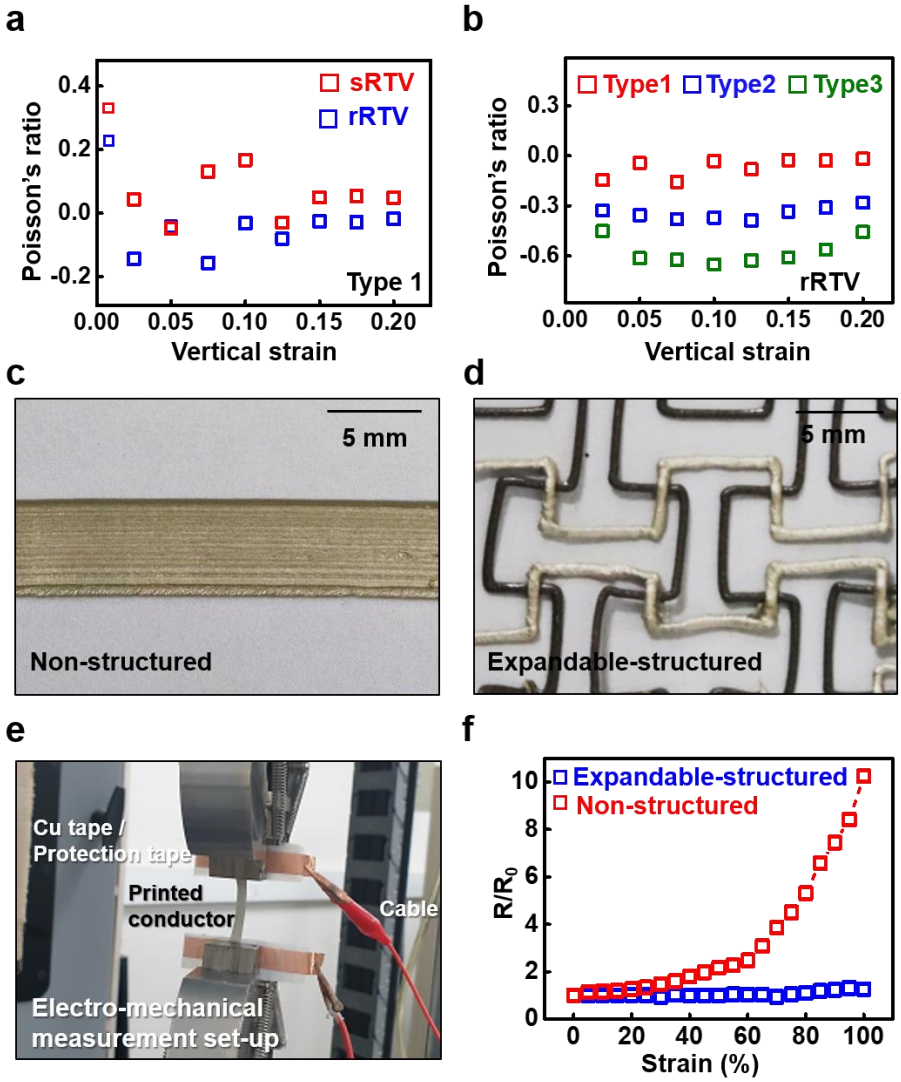

Figure 59. Mechanical properties of missing rib structure and electromechanical properties of conductors. (a) Poisson's ratio by vertical strain on type 1 missing rib structure with sRTV, rRTV. (b) Poisson's ratio by vertical strain with type 1, 2, 3 with rRTV. Image of conductors with (c) non-structured (d) expandable-structured. (e) Image of electromechanical testing setup (f) Resistance ratio by vertical strain on two types of conductor

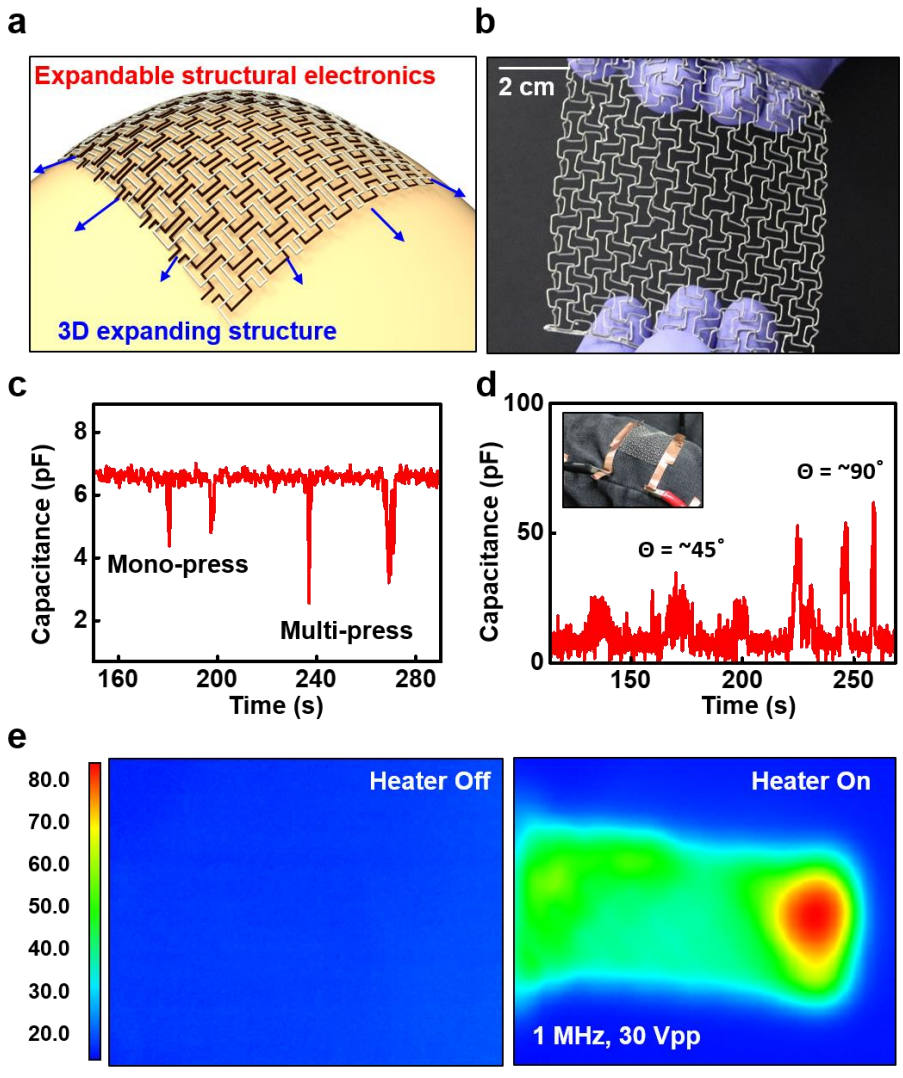

Figure 60. Expandable structural electronic system based electronics (a) Schematic illustration of expandable structural electronics without substrate directly interfacing expanding structure (b) Image of printed expandable structured capacitive sensor (c) Capacitance by number of finger pressing on sensor (d) Capacitance by strain of knee on the sensor with repetitive stimulus (e) IR image of before (left) and after (right) applying AC voltage to resistive type expandable heater.

4.3.6. Electronic components within missing rib structure

In the context of printing an expandable structure, variable expandable electronics were enabled by the partially printed conductor (Ag-RTV) with control frame (rRTV). Non-structured printed resistor and an expandable structure based resistor shows the different trends of resistance change when the strain was applied from 0 to 100%. Regarding non-structured resistors, resistance continued to increase with the strain. After 60% of strain, a rapid increase in resistance was observed owing to the decreased percolation path of the Ag flakes as the polymer was stretched. Regarding the expandable-structured resistor, the change in resistance was insignificant despite 100% strain being applied. Furthermore, the stretch deformation of the polymer could be reduced.

Capacitor type strain sensor, based on a structure wherein rRTV forms the structure on the x-axis and Ag-RTV forms the electrode on the y-axis. The capacitance remained at 6 pF under no external force but decreased to approximately 4 pF when pressed with one finger and decreased to 2 pF when pressed with two fingers, demonstrating the sensor's variable pressure sensitivity. Also it was attached to the knee to measure the capacitance change according to the strain correlated with the leg angle change after attachment. A capacitance of approximately 6 pF was maintained when the leg was not moved, while a capacitance of approximately 20 pF was confirmed when the leg angle was changed by approximately 45°. A large change in the leg angle of approximately 90° resulted in an increased capacitance of 20 pF. The distance between the two electrodes forming the capacitor and the conformal contact of the fabric increased according to the knee movement, which increased the capacitance.

The device was also applicable to cloth for heating system due to substrateless platform, with expandable structured resistor type heater. The expandable structure could function stably as an

electronic device because of the negligible change in resistance to 100% strain. When the heater is off, the overall temperature is between 20 and 30 °C. However, when the heater was operated under 1 MHz and 30 Vpp conditions, the overall temperature of the heater was between 50 and 60 °C, with a local temperature of up to 80 °C.

4.3.7. Pneumatic soft actuator integration

One-step manufacturing to create a 3D-structured soft actuator and soft electronic devices was demonstrated. 3D-printed actuators and sensors integrated into the strain limiter of the soft actuator. Two types of electronics are integrated: a non-structured, resistor-based strain sensor and an expandable-structured, deformation-resistive electrode. Resistance changes in the embedded electronics during actuator operation are measured, indicating the potential use of the strain sensor and the effectiveness of the structured electrode in maintaining resistance. Furthermore, operation of a surface-mounted device (SMD) chip through the embedded stretchable conductor of the fabricated actuator was demonstrated, highlighting the versatility and potential applications of the printed structures.

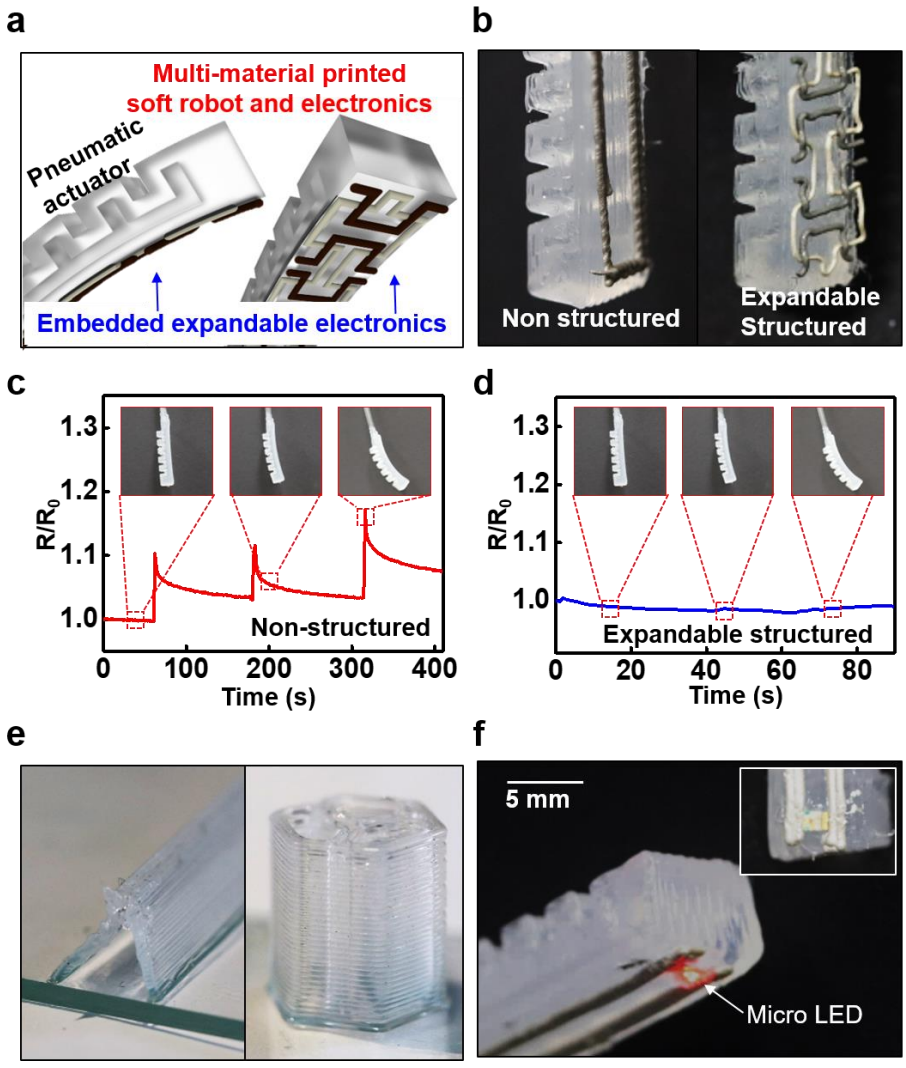

Figure 61. Integration of expandable structural electronics with pneumatic actuator. (a) Schematic illustration of the concept (b) Images of non-structured (left) and expandable structured (right) resistor on pneumatic actuator. Resistance ratio change by pressure applied to actuator with (c) non-structured resistor and (d) expandable structured resistor. (e) Various shape of fluidic channels for pneumatic actuator with sRTV, triangular horizontal 1 channel (left) hexagonal vertical 3 channels (right). (f) Integration of micro LED with expandable electronic system on actuator

4.4. Conclusion

In chapter 4, we proposed three types of 3D printable ink materials for expandable structural electronics with three types of missing rib structures. Ag-RTV is used as a stretchable conductor, high strength elastic rRTV as a control frame, and hyperelastic sRTV as an object frame for the pneumatic actuator. We demonstrated the fabrication of expandable structural electronics via multi-material printing, such as capacitor type strain sensors and resistor type heaters. Our one step 3D printing process simplified the manufacturing system and enabled the realization of soft actuators embedded in various structured electronics. Our findings show the potential of these 3D printable ink materials and expandable structures for the development of soft and stretchable electronics. This study demonstrates the potential of utilizing a simplified multi-material based fabricating platform to extend the functionality of 3D printed structures, providing unique opportunities for future applications such as personalized and customized soft electronics and actuators in cases requiring multi-dimensional deformations.

Chapter 5. 3D patternable eco-friendly photoresist

5.1. Motivation

In Chapters 2, 3, and 4, the focus was on creating 3D-printable biodegradable electronic components for primarily customized applications and addressing the stability of electronic systems under multi-axial deformation caused by real-world usage. In this chapter, instead of 3D printing electronic components for bespoke product, the goal was to develop a 3D photoresist capable of patterning existing deposition-based electronic materials. The idea was to combine this photoresist patterning method, which is compatible with eco-friendly development and removal processes, with existing vapor deposition techniques that are safe for human and biological interactions, to achieve bespoke bio-interfaced electronics.

By enabling patterning on 3D surfaces from the initial state, it would eliminate the need to consider prerequisite design factors for conformal contact and solely focus on design factors related to deformation occurring in the real world. For instance, when bending or stretching thin films to achieve conformal contact, the mechanical properties are already approaching their limits. However, with the ability to achieve conformal contact from the beginning, designs such as serpentine structures would only need to regard deformation-related factors. The technology for patterning with light in 3D space is recently developed, and it can be effectively incorporated. Examples include computed axial lithography (CAL), which involves rotating resin and performing 3D photopolymerization using projection[172], and the use of micro-patterned lenses to create various 3D patterns based on diffraction patterns when transmitted through them[173]. However, those methods aren't yet enable for in-situ patterning on 3D target

surfaces.

There are also some methods introduced for in-situ deposition of electronic materials on biostructures or 3D surfaces. For example, oxidative chemical vapor deposition (oCVD) was used to deposit PEDOT-Cl on plants or cotton using a vapor deposition method[174, 175]. Also evaporation induced sintering of liquid metal with biological nanofibrils on leaf[176]. Other methods showed carbon based inks (highly transparent and conductive graphene, plasma treated carbon black with block co polymer) on 3D or diverse insulating surfaces[177, 178].

While there has been considerable research on water-soluble photoresists, there have been no reports on the development of biocompatible photoresists capable of patterning on 3D surfaces. This research is expected to open up opportunities for on-demand production of electronic tattoos and other applications.

5.2. Materials and methods

5.2.1. Preparation of 3D patternable eco-friendly photoresist

4-pentanoic anhydride (PNA), PEGDA, 2,2-dimethoxy-2-phenyl-acetophenone, and pentaerythritol tetrakis(3-mercapto-propionate) were proportioned following the synthesis method for the existing polyanhydride (PA). The ratio of PNA and PEGDA was adjusted to improve wettability, and brilliant yellow (BY) was included as a bioabsorbable inhibitor. The mixture was then placed in a brown vial and mixed using a vortex mixer.

5.2.2. Characterization of rheological properties of photoresist

The viscosity of photoresist was measured using a rheometer by increasing the shear rate from 0.1 s^{-1} to 100 s^{-1}. For photo-

responsive rheology, continuous exposure to UV 365 nm at 15 mW/cm^2 was applied, and the plate gap was set to 0.123 mm. The shear modulus was measured for 600 seconds, and the measurement was stopped at the point of saturation.

5.2.3. Characterization of wettability of photoresist

For contact angle measurements of photoresist, a micro stage capable of movement along the XYZ axes was used. A DSLR camera (Canon, Inc) with a macro lens was positioned to capture the images. The camera lens was installed to face the front of the micro stage. A glass substrate was placed horizontally on the micro stage, and either PA or photoresist was carefully deposited on the substrate using a Pasteur pipette, creating a single droplet with a meniscus. Backlighting was applied from the back of the sample in the direction of the camera, and images were captured. The contact angle analysis tool in Image J was used to measure the contact angles.

5.2.4. Characterization of coating ability of photoresist

A slide glass (76 mm x 26 mm) is placed on top of a PDMS block to enable various incline angles. To measure the coating thickness based on the incline angle, a 200 μl droplet is dispensed at the middle section of the slide glass, and as it reaches the other end point, it is immediately cured using a UV lamp (365nm, 15W). Subsequently, using a Vernier caliper (with 1 μm accuracy), the thickness is measured at various distances from the droplet (0, 3, 6 cm). To measure the coating thickness over time, the same setup as before is used, but at regular intervals, the droplet is cured immediately at the same incline angle, and the thickness is measured.

5.2.5. Design and 3D patterning / 3D printing of photoresist

The laser marker capable of 3D autofocusing (MD U1000C, Keyence, Inc) is used to pattern various surfaces with photoreist according to the designed patterns in CAD files. Multi-layered designs can enable 3D printing, while layer by layer deposition of can be done via high slope angle in rapid time by additional droplet.

5.3. Results and discussion

5.3.1. Strategy for 3D patternable eco-friendly photoresist

The goal is to achieve in-situ 3D patterning of photoresist coated on a 3D solid substrate. The photoresist exhibits wetting on the surfaces of 3D objects due to three different surface tensions. Higher wettability on the surface leads to better coating, making the control of photoresist wettability a crucial factor in 3D patterning. The composition of the internal agents in the photoresist includes an inhibitor, photocurable crosslinks, water-soluble crosslinks, wettability control polymer, and a photoinitiator. The proposed scenario for using the developed photoresist would involve uniform patterning of the photoresist on the 3D surface, followed by patterning using laser equipment, development using water, and removal of various materials using either water or propylene carbonate (PC).

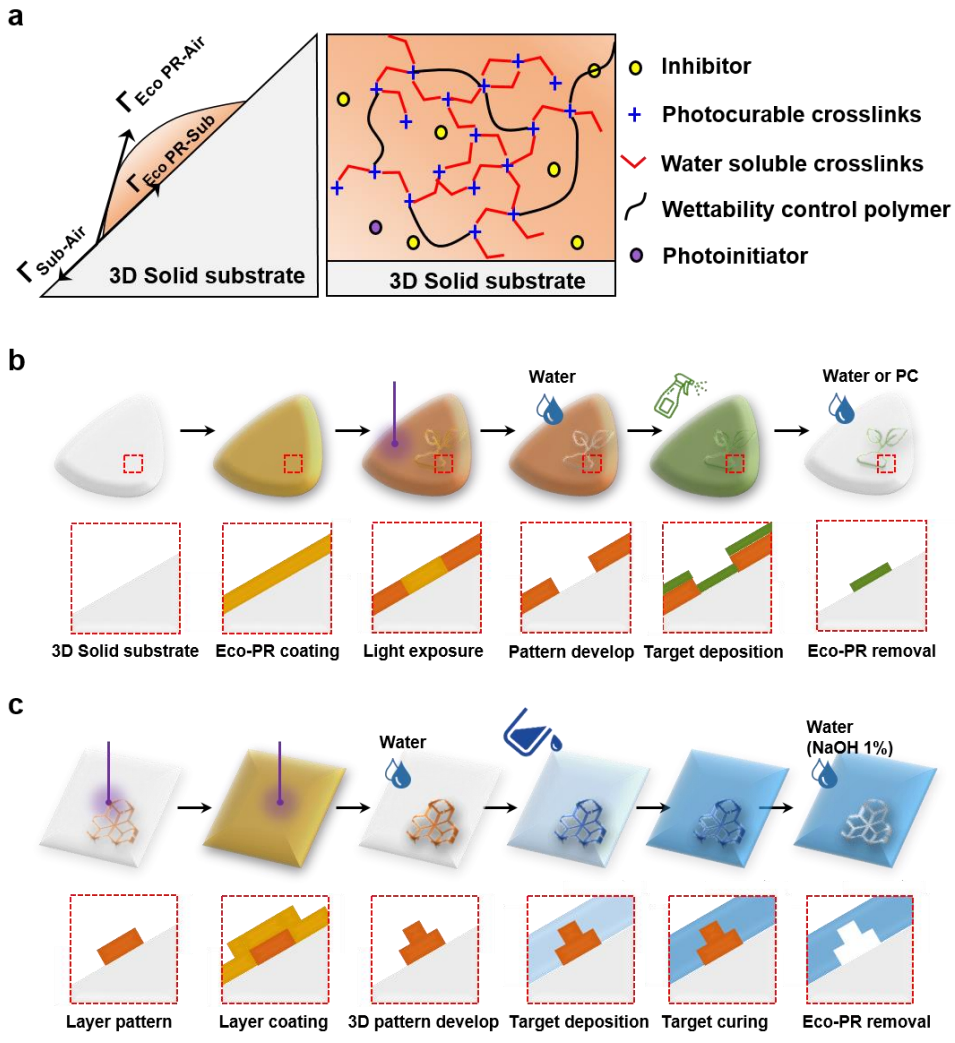

Figure 62. Schematic illustration of concept of the 3D patternable eco-friendly photoresist. (a) Illustration of balanced surface energy for wettability of photoresist on 3D substrate. Constituents include water soluble, photocurable crosslinks and wettability control polymer, photoinitiator, inhibitor (b) Scenario of using the photoresist for 3D patternable masks for vapor deposition (c) Scenario of using the photoresist for 3D patternable mold for fluidic channel

5.3.2. Characterization of photoresist matrix

The characterization of the properties of PA, which serves as the matrix material for the photoresist, was conducted first. From the perspective of wettability, the contact angle on glass was measured according to the ratio of PNA/PEGDA. It was observed that as the ratio of PNA/PEGDA increased, the contact angle decreased, indicating higher wettability. However, considering that a higher ratio of PNA/PEGDA results in a lower proportion of acrylate, which leads to decreased photo curable ability, a fixed ratio of PNA / PEGDA = 14 was chosen. Subsequently, the photopolymerization behavior was evaluated. When exposed to 15 mW/cm^2 of light, the shear modulus was measured, and it was observed that gelation occurred rapidly with the storage modulus and loss modulus crossing each other in less than 1 minute. The viscosity, determined by shear rate, exhibited minimal changes, suggesting the photoresist behaved as a Newtonian fluid, capable of flowing well on inclined surfaces regardless of external stress. Additionally, it was confirmed that the photoresist exhibited high wettability with contact angles of approximately 30−40 degrees on various substrates such as metal, ceramic, elastomer, plastic, and Si wafer.

Based on the measurements of PA's wettability and rheology, droplets were deposited on inclined surfaces to measure the thickness based on the angle and the thickness over time after droplet deposition. All thickness measurements were performed after curing. For different incline angles, curing was initiated as the droplet reached the end of the slope. For a droplet−to−substrate distance of 0 cm, the thickness was approximately 40 μm, which was similar to the thickness observed at 3 cm (~110 μm). For a distance of 6 cm, a steeper incline of 75 degrees resulted in thinner thickness (~170 μm) as the PA flowed off the slope. However, significant differences were observed when measuring thickness over time. A comparison between immediate curing after droplet

deposition (~4 seconds) and curing after 30 minutes revealed thicknesses of approximately 40 μm, 110 μm, and 170 μm for 0 cm, 3 cm, and 6 cm, respectively, in the 4-second case. However, in the 30-minute case, thicknesses of approximately 8 μm, 13 μm, and 14 μm were observed for the same distances. These findings provide optimization factors for achieving the desired coating thickness on each surface.

Considering the need for prompt removal of PA, various conditions were investigated. Although PA is a substance that dissolves in water, it did not dissolve rapidly within 5 minutes. Therefore, it was observed that removal within 1 minute was achieved when using a slightly basic solution of approximately 1% NaOH. This concentration of NaOH was determined to be safe for brief contact with the skin based on references. However, it was anticipated that patterning followed by deposition of materials in a NaOH 1% environment could lead to delamination or instability. To address this concern, it was considered beneficial to induce swelling and subsequent removal by creating wrinkles, similar to a developing process in photography. Thus, propylene carbonate (PC), a polar solvent with a significantly higher dipole moment compared to water, was used. It was observed that the thickness increased by approximately 1.5 to 2 times within 5 minutes, and subsequently, successful delamination from the substrate was achieved.

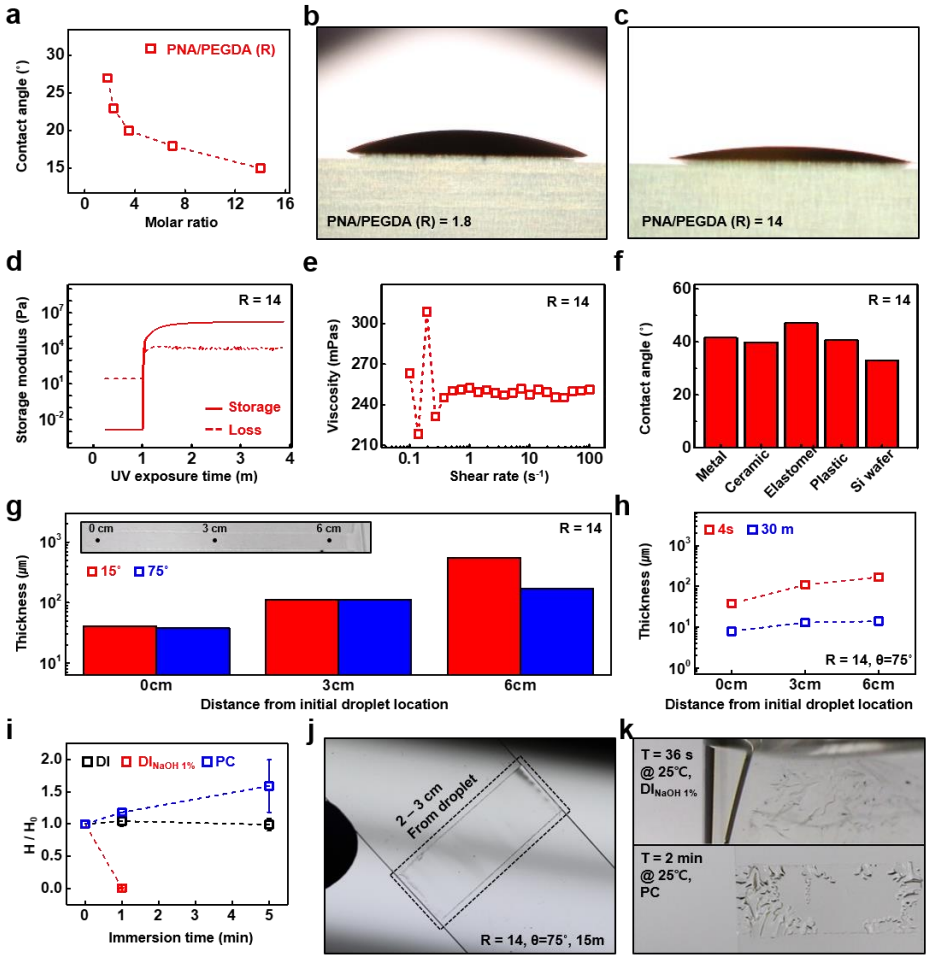

Figure 63. Characterization of photoresist matrix. (a) Contact angle of PA by molar ratio between PNA/PEGDA on glass. Image of droplet on glass with (b) PNA/PEGDA = 1.8, (c) PNA/PEGDA = 14. (d) Photo-rheological properties of PA with PNA/PEGDA = 14 with 15 mW/cm^2. (e) Viscosity of PA by shear rate (f) Contact angle of PA on various substrate (Metal, ceramic, elastomer, plastic, Si wafer). Thickness of PA on (g) different slope angle of glass substrate and (h) different time with same slope angle. (i) Thickness of PA in diverse polar solvents in 5 min. (j) Image and condition of tested samples for interactions with polar solvents (k) Images of morphological difference of PA in NaOH 1% water and propylene carbonate.

5.3.3. Characterization of photoresist matrix with inhibitor

The photopolymerization mechanism of PA utilizes thiol-ene reactions. However, the power of the laser marker used was 3.6W, resulting in a large power output of approximately 36 mW at 1% power, which was received by a spot size with a diameter of about 25 μm. As a result, when attempting actual patterning, many areas quickly hardened and experienced over-curing. To address this issue, a bioabsorbable inhibitor that absorbs in the UV range was used to selectively pattern desired areas. Subsequent quantitative analysis similar to the previous PA characterization was conducted. When evaluating the photopolymerization with varying amounts of inhibitor, it was observed that the curing rate slowed down when reaching 20% compared to the saturation point of the storage modulus. For example, with an inhibitor concentration of 0 g/ml, the curing time was 1.26 min, while at 0.06 g/ml, it increased to 1.40 min, and at 0.12 g/ml, it further extended to 3.15 min. Although no significant differences were observed in wettability, the viscosity exhibited shear thinning behavior with increasing inhibitor concentration, indicating better flow under high external stress. This implies that in future experiments involving flow on inclined surfaces, it may be necessary to test at steeper angles, as the material may not flow well at lower inclinations.

For experiments maintaining an incline angle of 75 degrees and varying the curing time, the thickness measured from the droplet at distances of 0 cm, 3 cm, and 6 cm was approximately 120 μm, 120 μm, and 160 μm, respectively, after 4 seconds. However, after 30 minutes, the corresponding thicknesses were approximately 12 μm, 17 μm, and 39 μm. This indicates that at the intermediate time range, at a distance of 3 cm from the droplet, the thickness ranged from approximately 20 μm to 110 μm. Additionally, it was confirmed that the material could be developed using water, and it dissolved rapidly in a basic water environment.

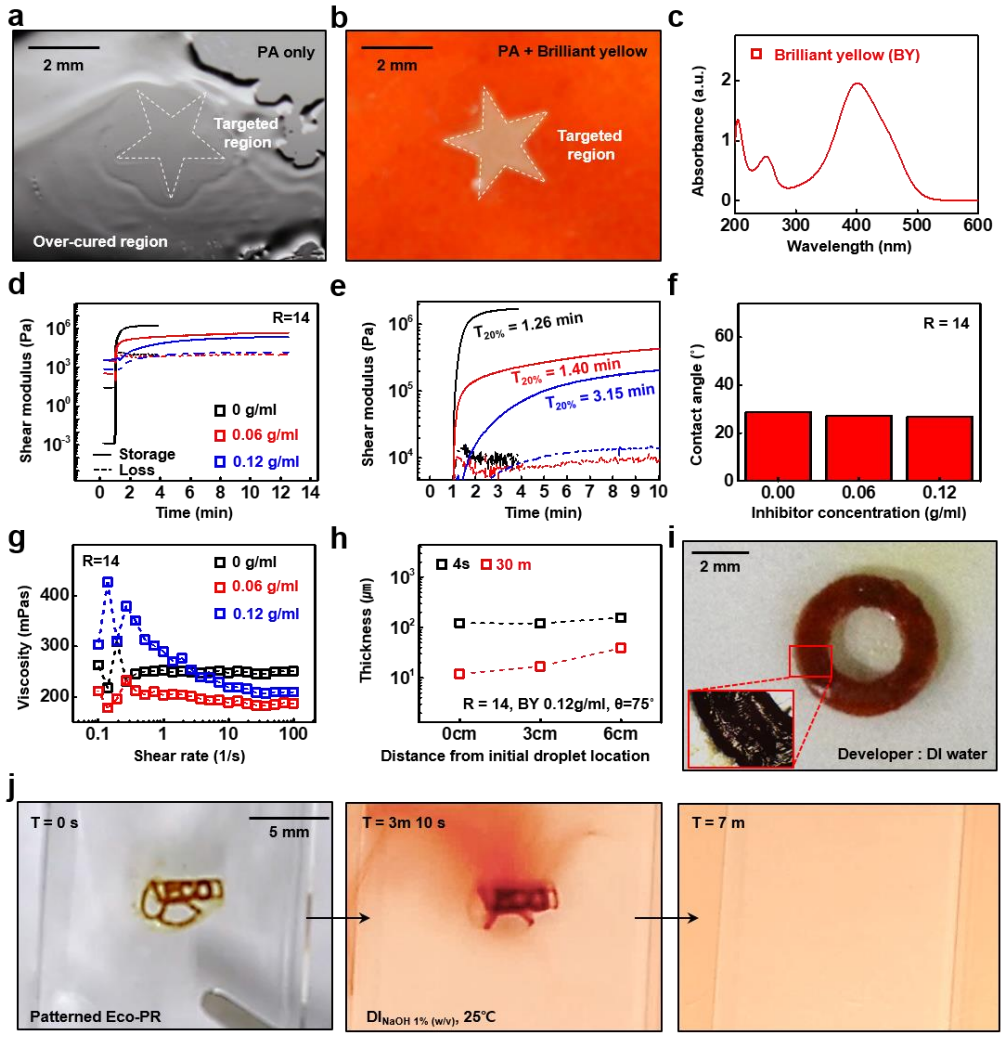

Figure 64. Characterization of photoresist matrix with inhibitor. Image of photo patterned PA (a) without Brilliant yellow (b) with Brilliant yellow. (c) UV-VIS spectra of Brilliant yellow (d) Photo-rheological properties of PA with different concentration of Brilliant yellow. (e) Magnified view of photo-rheological properties of PA with Brilliant yellow. (f) Contact angle, (g) Viscosity by shear rate and (h) thickness by different time at same slope angle of PA with Brilliant yellow. (i) Developed pattern with photoresist with water (j) Serial images of dissolution behavior of photoresist in NaOH 1% water

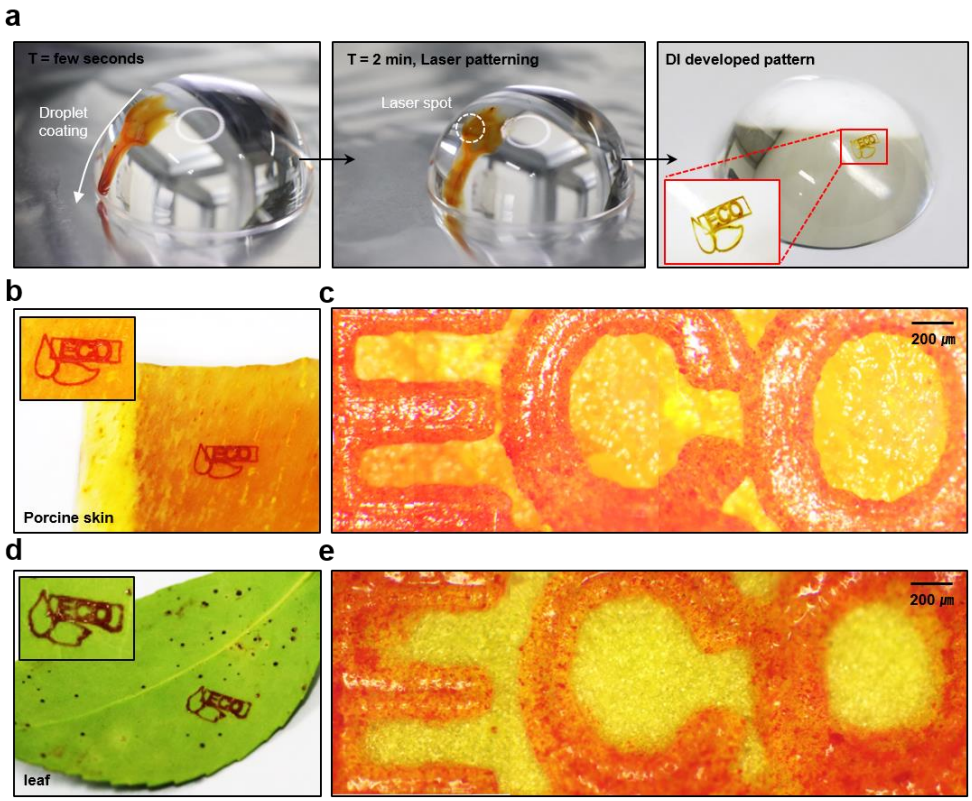

Figure 65. Photoresist patterning on various substrate (a) Serial images of patterning photoresist on 3D glass hemisphere (b) Images of patterned 'Eco' icon on porcine skin. (c) Magnified view of patterned 'Eco' icon on porcine skin. (d) Images of patterned 'Eco' icon on leaf. (e) Magnified view of patterned 'Eco' icon on leaf.

5.3.4. Patterning on complex surface / tissue surface

The optimized photoresist, referred to as "Eco," was patterned on various surfaces, including each hemisphere glass, porcine skin, and a leaf, in the form of an icon. The patterning process proceeded as follows: a droplet was coated, and after a certain period, selective polymerization was carried out by illuminating the area with a laser. Subsequently, during the development process using water, even with vigorous washing using a squeezer, it was observed that the pattern adhered well to each surface. This could be attributed to the effective crosslinking between the functional groups, particularly amines present in the proteins, and the acrylate groups of the photoresist, or the presence of micro-roughness on the glass surface, which might contribute to Van der Waals interactions. However, further analysis is planned as part of subsequent research to investigate these phenomena. When the patterned icon was magnified, it was confirmed that the 200 μm tolerance was sufficient to distinguish the pattern clearly.

5.3.5. Patterning mask for electronics

Using the developed photoresist, masks were created for patterning various electronics. For instance, strain sensors, heaters, EMG electrodes, and capacitive sensor arrays were attempted, and all of them were successfully patterned. Subsequently, a capacitive sensor mask was patterned on a glass substrate treated with 1 minute of O_2 plasma treatment, and a conductive spray based on graphite was coated. The purpose of the O_2 plasma treatment was to enhance the adhesion of the commercial conductive spray. If there is a conductive coating material with good adhesion in the future, this step may no longer be necessary. The mask was then detached using PC, and the electrical performance of the patterned sensor was measured. In a tactile sensor demonstration, when fingers were placed on 0, 1, or 2 electrodes, the dielectric between the electrodes was filled with the finger, resulting in an increase in

capacitance. It was observed that the capacitance values changed to approximately 6 pF, 23 pF, and 43 pF, respectively. Additionally, in a hydration sensor demonstration, as 100 μL of DI water was added incrementally, the capacitance values showed a nearly uniform increase: 4.2 pF (0 μL), 8.3 pF (100 μL), 11 pF (200 μL), and 15.6 pF (300 μL). Furthermore, it was observed that inductors patterned on hemispheres exhibited higher Q factors compared to inductors patterned on a flat plane with uniform sizes.

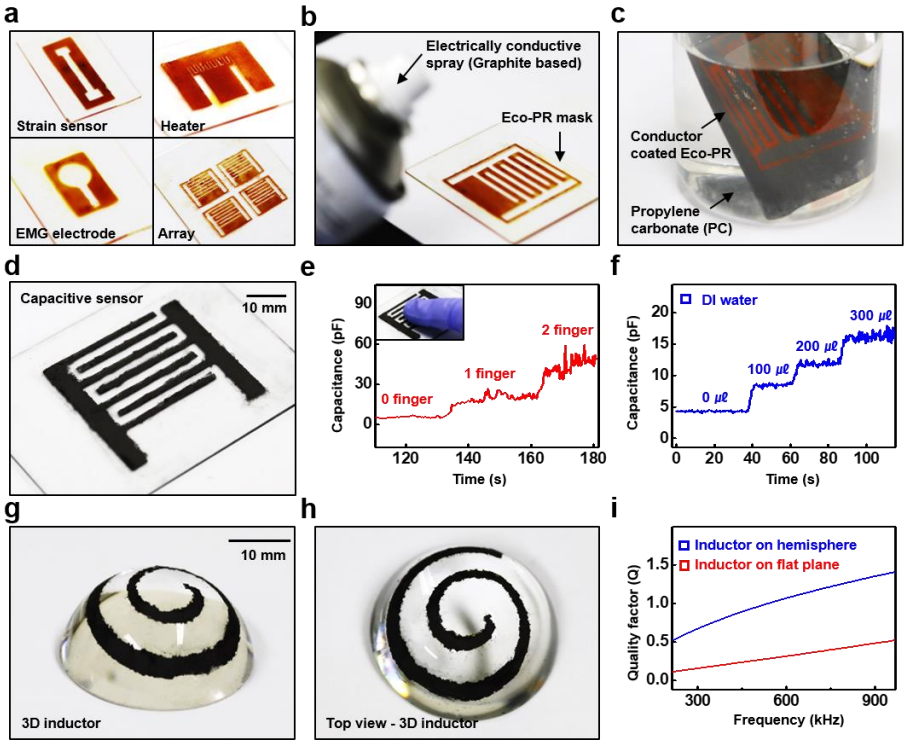

Figure 66. Applications of patterned photoresist for 3D mask (a) Masks patterned with photoresist for various sensors (b) Image of spray-coating of conductive inks on photoresist patterned masks (c) Image of removing masks with propylene carbonate (d) Image of patterned capacitive sensor and it performance measuring (e) number of fingers on sensors and (f) water contents. (g,h) Perspective and top image of 3D patterned inductor on glass hemisphere. (i) Quality factor of 3D patterned inductor and planar patterned inductor.

5.3.6. Patterning mold for fluidics

Although the focus was initially on using photoresist for photo masks, it was demonstrated that photoresist can also be used to create fluidics and various shapes of different heights for fluidics molds through 3D printing. First, by placing a slope and controlling the thickness of each droplet over time, layer-by-layer patterning was performed, resulting in the creation of 3-layered stars and 5-layered pyramids. This allows for future possibilities of multi-material printing. PEGDA and multi-material printing were also attempted. However, the rapid decrease in thickness on the slope, which could lead to decreased quality, was a concern. Assuming that the thickness decreases linearly from 12 μm at 4 seconds to 120 μm at 1800 seconds at a distance of 0 cm from the droplet with a 75-degree slope, the thickness would decrease at a rate of 0.06 μm/sec. Considering the printing speed of 15 mm/s, if each unit layer takes 100 seconds to print, there would be an error of 6 μm. However, since the spot size is 25 μm, it is considered tolerable for small objects. Subsequently, photoresist was patterned to create a fluidic channel, and printing at different heights demonstrated the use of the printed structure as a pump mold. Finally, it was shown that on a final 3D curved surface, reaction chambers can be formed in specific local areas. Silicone sealant was used to create a fluidic frame, and desired reaction chambers were formed by perfusing with basic water.

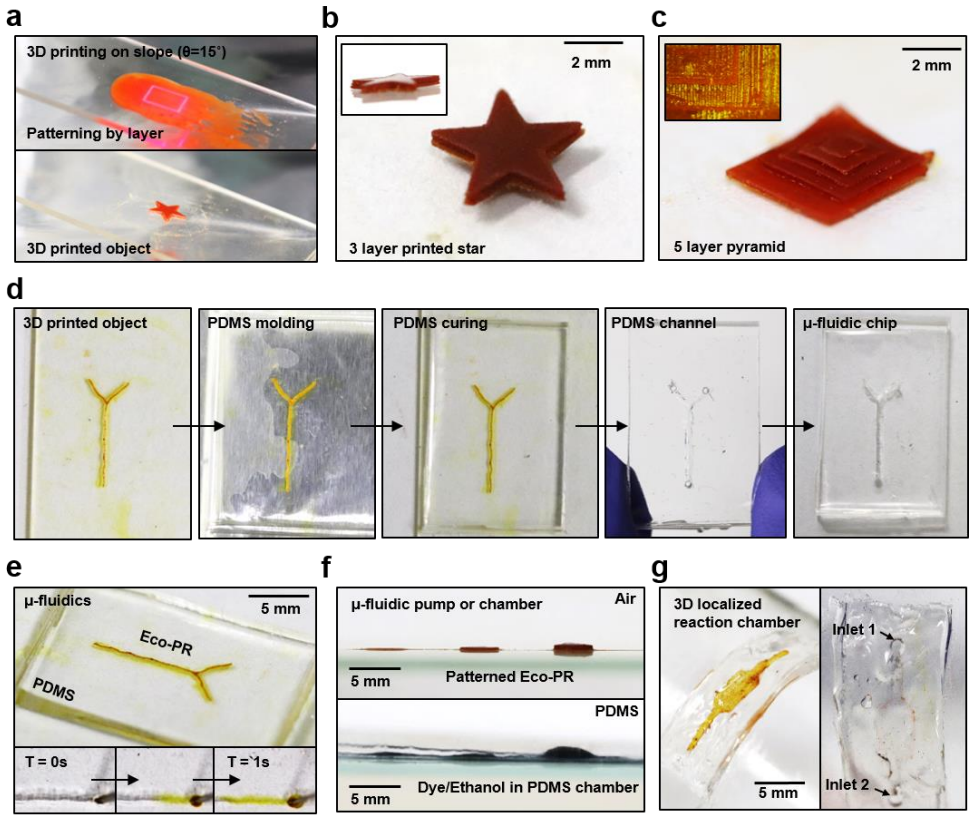

Figure 67. Applications of patterned photoresist for 3D mold. (a) Images of 3D printing process of photoresist on slope (b) 3D printed 3 layered stars on slope (c) 3D printed 5 layered pyramid on slope (d) Fabrication process of microfluidic chip with the photoresist. (e) Image of cured PDMS channel via photoresist and serial images of fluid flow inside the generated channel (f) Image of mold and fabricated microfluidic pumps or well with different height monolithically fabricated by photoresist (g) Image of mold and fabricated localized reaction chamber on 3D glass surface.

5.4. Conclusion

In Chapter 5, an eco-friendly photoresist called Eco-PR was developed to enable patterning on 3D surfaces from the beginning. First, the properties of the matrix material without any inhibitors were evaluated, and then the properties of the photoresist fabricated using a bioabsorbable inhibitor were also evaluated. It was demonstrated that the photoresist can be used for printing not only on solid objects but also on tissues such as porcine skin or leaves. Eco-PR can be developed using water as a developer and can be removed using slightly alkaline water or propylene carbonate. Furthermore, it was verified that it can be used for making masks for electronics fabrication through vapor deposition and for creating 3D printed molds for fluidics fabrication.

References

1. Nicolini, C., *From neural chip and engineered biomolecules to bioelectronic devices: an overview.* Biosensors and Bioelectronics, 1995. **10**(1-2): p. 105-127.
2. *Medical electronics international organization.* IEEE Electrical Engineering, 1959. **78**(1): p. 119-120.
3. Choi, S., et al., *Recent advances in flexible and stretchable bio-electronic devices integrated with nanomaterials.* Advanced materials, 2016. **28**(22): p. 4203-4218.
4. Gao, D., K. Parida, and P.S. Lee, *Emerging soft conductors for bioelectronic interfaces.* Advanced Functional Materials, 2020. **30**(29): p. 1907184.
5. Cho, K.W., et al., *Soft bioelectronics based on nanomaterials.* Chemical Reviews, 2021. **122**(5): p. 5068-5143.
6. Yuk, H., J. Wu, and X. Zhao, *Hydrogel interfaces for merging humans and machines.* Nature Reviews Materials, 2022. **7**(12): p. 935-952.
7. Gu, J.W., J.H. Lee, and S.K. Kang, *3D Electronic Sensors for Bio-Interfaced Electronics and Soft Robotics.* Advanced Sensor Research, 2023: p. 2300013.
8. *Bioelectric Medicine Market Size, Share & Trends Analysis Report By Type (Implantable Electroceutical Devices, Non-invasive Electroceutical Devices), By Product, By Application, By End-use, By Region, And Segment Forecasts, 2022 - 2030, Accessed 2023-06-15, https://www.grandviewresearch.com/industry-analysis/electroceuticals-bioelectric-medicine-market.*
9. *Wearable Medical Device Market Size, Share & Trends Analysis Report By Product (Diagnostic, Therapeutic Devices), By Site (Handheld, Headband, Strap, Shoe Sensors), By Application, By Region And Segment Forecasts, 2023 - 2030, Accessed 2023-06-15, https://www.grandviewresearch.com/industry-analysis/wearable-medical-devices-market.*
10. *Brain Computer Interface Market Size, Share & Trends Analysis Report By Application (Healthcare, Communication & Control), By Product (Invasive, Non-invasive), By End Use (Medical, Military), And Segment Forecasts, 2023 - 2030, Accessed 2023-06-15, https://www.grandviewresearch.com/industry-analysis/brain-computer-interfaces-market.*
11. Wang, C., et al., *Conformal electrodes for on-skin digitalization.* SmartMat, 2021. **2**(3): p. 252-262.
12. Sunwoo, S.-H., et al., *Wearable and implantable soft bioelectronics: device designs and material strategies.* Annual Review of Chemical and Biomolecular Engineering, 2021. **12**: p. 359-391.
13. Yao, G., et al., *Flexible bioelectronics for physiological signals sensing and disease treatment.* Journal of Materiomics, 2020. **6**(2): p. 397-413.

14. Cho, Y.U., et al., *Transparent neural implantable devices: A comprehensive review of challenges and progress.* npj Flexible Electronics, 2022. **6**(1): p. 53.
15. Kim, D.-H., et al., *Epidermal electronics.* science, 2011. **333**(6044): p. 838-843.
16. Kaltenbrunner, M., et al., *An ultra-lightweight design for imperceptible plastic electronics.* Nature, 2013. **499**(7459): p. 458-463.
17. Lipomi, D.J., et al., *Skin-like pressure and strain sensors based on transparent elastic films of carbon nanotubes.* Nature nanotechnology, 2011. **6**(12): p. 788-792.
18. Park, Y.-G., S. Lee, and J.-U. Park, *Recent progress in wireless sensors for wearable electronics.* Sensors, 2019. **19**(20): p. 4353.
19. Yu, Y., et al., *Flexible electrochemical bioelectronics: the rise of in situ bioanalysis.* Advanced materials, 2020. **32**(15): p. 1902083.
20. Hong, Y.J., et al., *Wearable and implantable devices for cardiovascular healthcare: from monitoring to therapy based on flexible and stretchable electronics.* Advanced Functional Materials, 2019. **29**(19): p. 1808247.
21. Li, H., Y. Ma, and Y. Huang, *Material innovation and mechanics design for substrates and encapsulation of flexible electronics: a review.* Materials Horizons, 2021. **8**(2): p. 383-400.
22. Carlson, A., et al., *Transfer printing techniques for materials assembly and micro/nanodevice fabrication.* Advanced Materials, 2012. **24**(39): p. 5284-5318.
23. Kim, D.H., et al., *Stretchable, curvilinear electronics based on inorganic materials.* Advanced Materials, 2010. **22**(19): p. 2108-2124.
24. Miyamoto, A., et al., *Inflammation-free, gas-permeable, lightweight, stretchable on-skin electronics with nanomeshes.* Nature nanotechnology, 2017. **12**(9): p. 907-913.
25. Matsuhisa, N., et al., *Materials and structural designs of stretchable conductors.* Chemical Society Reviews, 2019. **48**(11): p. 2946-2966.
26. Xu, S., et al., *Stretchable batteries with self-similar serpentine interconnects and integrated wireless recharging systems.* Nature communications, 2013. **4**(1): p. 1543.
27. Zhang, Y., et al., *Experimental and theoretical studies of serpentine microstructures bonded to prestrained elastomers for stretchable electronics.* Advanced Functional Materials, 2014. **24**(14): p. 2028-2037.
28. Kim, D.H., et al., *Optimized structural designs for stretchable silicon integrated circuits.* small, 2009. **5**(24): p. 2841-2847.
29. Someya, T., et al., *Conformable, flexible, large-area networks of pressure and thermal sensors with organic transistor active matrixes.* Proceedings of the National Academy of Sciences, 2005. **102**(35): p. 12321-12325.
30. Shyu, T.C., et al., *A kirigami approach to engineering elasticity in nanocomposites through patterned defects.* Nature materials, 2015. **14**(8): p. 785-789.

31. Morikawa, Y., et al., *Ultrastretchable kirigami bioprobes.* Advanced healthcare materials, 2018. **7**(3): p. 1701100.
32. Wu, H., et al., *A transparent electrode based on a metal nanotrough network.* Nature nanotechnology, 2013. **8**(6): p. 421-425.
33. Khang, D.Y., J.A. Rogers, and H.H. Lee, *Mechanical buckling: mechanics, metrology, and stretchable electronics.* Advanced Functional Materials, 2009. **19**(10): p. 1526-1536.
34. Kim, D.-H., et al., *Stretchable and foldable silicon integrated circuits.* Science, 2008. **320**(5875): p. 507-511.
35. Kaltenbrunner, M., et al., *Ultrathin and lightweight organic solar cells with high flexibility.* Nature communications, 2012. **3**(1): p. 770.
36. Sun, Y., et al., *Controlled buckling of semiconductor nanoribbons for stretchable electronics.* Nature nanotechnology, 2006. **1**(3): p. 201-207.
37. Kim, J., et al., *Stretchable silicon nanoribbon electronics for skin prosthesis.* Nature communications, 2014. **5**(1): p. 5747.
38. Dickey, M.D., *Stretchable and soft electronics using liquid metals.* Advanced materials, 2017. **29**(27): p. 1606425.
39. Zhu, S., et al., *Ultrastretchable fibers with metallic conductivity using a liquid metal alloy core.* Advanced Functional Materials, 2013. **23**(18): p. 2308-2314.
40. Yang, C. and Z. Suo, *Hydrogel ionotronics.* Nature Reviews Materials, 2018. **3**(6): p. 125-142.
41. Keplinger, C., et al., *Stretchable, transparent, ionic conductors.* Science, 2013. **341**(6149): p. 984-987.
42. Rivnay, J., et al., *Structural control of mixed ionic and electronic transport in conducting polymers.* Nature communications, 2016. **7**(1): p. 11287.
43. Dion Khodagholy, J.N.G., Thomas Thesen, Werner Doyle, Orrin Devinsky, George G Malliaras & György Buzsáki *NeuroGrid: recording action potentials from the surface of the brain.* Nature Neuroscience, 2015. **18**: p. 310–315.
44. Graeme A. Snook, P.K., Adam S. Best, *Conducting-polymer-based supercapacitor devices and electrodes.* Journal of Power Sources, 2011. **196**(1): p. 1-12.
45. Bryan D. Paulsen, K.T., Eleni Stavrinidou & Jonathan Rivnay *Organic mixed ionic–electronic conductors.* Nature Materials, 2020. **19**: p. 13-26.
46. Xi Fan, W.N., Hsinhan Tsai, Naixiang Wang, Huihui Huang, Yajun Cheng, Rongjiang Wen, Liujia Ma, Feng Yan, Yonggao Xia, *PEDOT:PSS for Flexible and Stretchable Electronics: Modifications, Strategies, and Applications.* Advanced Science, 2019. **6**(19): p. 1900813.
47. Michael Vosgueritchian, D.J.L., Zhenan Bao, *Highly Conductive and Transparent PEDOT:PSS Films with a Fluorosurfactant for Stretchable and Flexible Transparent Electrodes.* Advanced Functional Materials, 2011. **22**(2): p. 421-428.
48. Savagatrup, S., et al., *Plasticization of PEDOT:PSS by Common*

Additives for Mechanically Robust Organic Solar Cells and Wearable Sensors. Advanced Functional Materials, 2015. **25**(3): p. 427-436.
49. Jin Young Oh, S.K., Hong-Koo Baik, Unyong Jeong, *Conducting Polymer Dough for Deformable Electronics.* Advanced Materials, 2015. **28**(22): p. 4455-4461.
50. Wang, Y., et al., *A highly stretchable, transparent, and conductive polymer.* Science Advances, 2017. **3**(3): p. e1602076.
51. Mei Ying Teo, N.K., Seyoung Kee, Bong Seong Kim, Geunjin Kim, Soonil Hong, Suhyun Jung, and Kwanghee Lee, *Highly Stretchable and Highly Conductive PEDOT:PSS/Ionic Liquid Composite Transparent Electrodes for Solution-Processed Stretchable Electronics.* ACS Applied Materials and Interfaces, 2017. **9**(1): p. 819-826.
52. Ambroise de Izarra, S.P., Jinhee Lee, Yves Lansac, and Yun Hee Jang, *Ionic Liquid Designed for PEDOT:PSS Conductivity Enhancement.* Journal Of The American Chemical Society, 2018. **140**(16): p. 5375–5384.
53. Liu, J., et al., *Self-Healing Kirigami Assembly Strategy for Conformal Electronics.* Advanced Functional Materials, 2022. **32**(12): p. 2109214.
54. Yu-Ki Lee, Z.X., Young-Joo Lee, Yun-Hyeong Kim, Yue Hao, Hongjin Choi, Myoung-Gyu Lee, Young-Chang Joo, Changsoon Kim, Jyh-Ming Lien, In-Suk Choi, *Computational wrapping: A universal method to wrap 3D-curved surfaces with nonstretchable materials for conformal devices.* Science Advances, 2020. **6**(15): p. eaax6212.
55. Lin, D., et al., *Three-dimensional printing of complex structures: man made or toward nature?* ACS nano, 2014. **8**(10): p. 9710-9715.
56. Ngo, T.D., et al, *Additive manufacturing (3D printing): A review of materials, methods, applications and challenges.* Composites Part B: Engineering, 2018. **143**: p. 172-196.
57. Guo, Y., et al, *Degradable and Fully Recyclable Dynamic Thermoset Elastomer for 3D-Printed Wearable Electronics.* Advanced Functional Materials, 2021. **31**(9): p. 2009799.
58. Hopkins, N., Liben Jiang, and Hadley Brooks., *Energy consumption of common desktop additive manufacturing technologies.* Cleaner Engineering and Technology, 2021. **2**: p. 100068.
59. Bader, C.e.a., *Making data matter: Voxel printing for the digital fabrication of data across scales and domains.* Science advances, 2018. **4**(5): p. eaas8652.
60. Skylar-Scott, M.A., et al., *Voxelated soft matter via multimaterial multinozzle 3D printing.* Nature, 2019. **575**(7782): p. 330-335.
61. Schaffner, M., et al., *3D printing of bacteria into functional complex materials.* Science Advances, 2017. **3**(12): p. eaao6804.
62. Zhou, L.Y., Fu, J., & He, Y., *A review of 3D printing technologies for soft polymer materials.* Advanced Functional Materials, 2020. **30**(28): p. 2000187.
63. Yan, Q., et al., *A review of 3D printing technology for medical applications.* Engineering, 2018. **4**(5): p. 729-742.

64. Liu, C., et al, *3D printing technologies for flexible tactile sensors toward wearable electronics and electronic skin.* Polymers 2018. **10**(6): p. 629.
65. Heiden, A., et al., *3D printing of resilient biogels for omnidirectional and exteroceptive soft actuators.* Science Robotics, 2022. **7**(63): p. eabk2119.
66. Zhu, Y., et al., *3D printing biomimetic materials and structures for biomedical applications.* Bio-Design and Manufacturing, 2021. **4**: p. 405-428.
67. Zhou, Y., et al, *Implantable thin film devices as brain-computer interfaces: recent advances in design and fabrication approaches.* Coatings, 2021. **11**(2): p. 204.
68. Park, Y.G., et al., *High-Resolution 3D Printing for Electronics.* Advanced Science, 2022. **9**(8): p. 2104623.
69. *DragonFly IV Tech Specs and Capabilities, Accessed 2023-06-16, https://www.nano-di.com/dragonfly-iv.*
70. Bae, J., et al, *3D-printed quantum dot nanopixels.* ACS nano, 2020. **14**(9): p. 10993-11001.
71. Jung, W., et al, *3D Nanoprinting with Charged Aerosol Particles—An Overview.* Accounts of Materials Research, 2021. **2**(11): p. 1117-1128.
72. Liu, S.-F., et al, *3D nanoprinting of semiconductor quantum dots by photoexcitation-induced chemical bonding.* Science, 2022. **377**(6610): p. 1112-1116.
73. Liu, S.F., et al, *3D Laser Nanoprinting of Functional Materials.* Advanced Functional Materials, 2023: p. 2211280.
74. Yang, L., et al., *Laser printed microelectronics.* Nature communications, 2023. **14**: p. 1103.
75. *IBM BRINGS AN ARCHITECTURE GUN TO A CHIP KNIFE FIGHT, Accessed 2023-06-16, https://www.nextplatform.com/2020/08/18/ibm-brings-an-architecture-gun-to-a-chip-knife-fight/.*
76. *Printed RFID in 2010, Accessed 2023-06-16, Last modified 2010-01-07, https://www.idtechex.com/en/research-article/printed-rfid-in-2010/1961.*
77. Lind, J.U., et al, *Instrumented cardiac microphysiological devices via multimaterial three-dimensional printing.* Nature materials, 2017. **16**(3): p. 303-308.
78. Zhu, Z., Hyun Soo Park, and Michael C. McAlpine., *3D printed deformable sensors.* Science Advances, 2020. **6**(25): p. eaba5575.
79. Lee, B., et al, *Omnidirectional printing of elastic conductors for three-dimensional stretchable electronics.* Nature Electronics, 2023: p. 1-12.
80. Valentine, A.D., et al, *Hybrid 3D printing of soft electronics.* Advanced materials, 2017. **29**(40): p. 1703817.
81. Haghiashtiani, G., et al., *3D printed patient-specific aortic root models with internal sensors for minimally invasive applications.* Science advances 2020. **6**(35): p. eabb4641.

82. Yuk, H., et al, *3D printing of conducting polymers.* Nature communications, 2020. **11**(1): p. 1604.
83. Asulin, M., et al, *One-Step 3D Printing of Heart Patches with Built-In Electronics for Performance Regulation.* Advanced Science, 2021. **8**(9): p. 2004205.
84. Singh, M., et al, *Minimally invasive electroceutical catheter for endoluminal defect sealing.* Science Advances, 2021. **7**(14): p. eabf6855.
85. Ouyang, X., et al, *3D printed skin-interfaced UV-visible hybrid photodetectors.* Advanced Science, 2022. **9**(25): p. 2201275.
86. Hui, Y., et al, *Three-dimensional printing of soft hydrogel electronics.* Nature Electronics 2022: p. 1-11.
87. Kim, M., et al, *Multimodal Characterization of Cardiac Organoids Using Integrations of Pressure-Sensitive Transistor Arrays with Three-Dimensional Liquid Metal Electrodes.* Nano Letters, 2022. **22**(19): p. 7892-7901.
88. Cheng, S., et al, *Electronic blood vessel.* Matter, 2020. **3**(5): p. 1664-1684.
89. Massetti, M., et al, *Fully 3D-printed organic electrochemical transistors.* npj Flexible Electronics, 2023. **7**(1): p. 11.
90. Su, R., et al., *3D-printed flexible organic light-emitting diode displays.* Science Advances, 2022. **8**(1): p. eabl8798.
91. Kong, Y.L., et al, *3D printed quantum dot light-emitting diodes.* Nano letters, 2014. **14**(12): p. 7017-7023.
92. Wu, S.-Y., et al., *3D-printed microelectronics for integrated circuitry and passive wireless sensors.* Microsystems & Nanoengineering, 2015. **1**(1): p. 1-9.
93. Kwon, J., et al, *Three-dimensional monolithic integration in flexible printed organic transistors.* Nature communications, 2019. **10**(1): p. 54.
94. Chamis, A.L., et al, *Staphylococcus aureus bacteremia in patients with permanent pacemakers or implantable cardioverter-defibrillators.* Circulation, 2001. **104**(9): p. 1029-1033.
95. Maytin, M., and Laurence M. Epstein, *Lead extraction is preferred for lead revisions and system upgrades: when less is more.* Circulation: Arrhythmia and Electrophysiology, 2010. **3**(4): p. 413-424.
96. Farooqi, F.M., et al, *Extraction of cardiac rhythm devices: indications, techniques and outcomes for the removal of pacemaker and defibrillator leads.* International journal of clinical practice, 2010. **64**(8): p. 1140-1147.
97. Fu, K.K., et al. , *Transient electronics: materials and devices* Chemistry of Materials 2016. **28**(11): p. 3527-3539.
98. Kang, S.-K., et al, *Bioresorbable silicon electronic sensors for the brain.* Nature 2016. **530**(7588): p. 71-76.
99. Koo, J., et al., *Wireless bioresorbable electronic system enables sustained nonpharmacological neuroregenerative therapy.* Nature medicine, 2018. **24**(12): p. 1830-1836.

100. Hwang, S.-W., et al, *A physically transient form of silicon electronics.* Science 2012. **337**(6102): p. 1640-1644.
101. Ashammakhi, N., et al. , *Biodegradable implantable sensors: materials design, fabrication, and applications.* Advanced Functional Materials 2021. **31**(49): p. 2104149.
102. Górski, F., et al., *Study on properties of automatically designed 3d-printed customized prosthetic sockets.* Materials 2021. **14**(18): p. 5240.
103. Chang, E., et al, *Percolation mechanism and effective conductivity of mechanically deformed 3-dimensional composite networks: Computational modeling and experimental verification.* Composites Part B: Engineering, 2021. **207**: p. 108552.
104. Han, W.B., et al, *Materials and Fabrication Strategies for Biocompatible and Biodegradable Conductive Polymer Composites toward Bio-Integrated Electronic Systems.* Advanced Sustainable Systems, 2022. **6**(2): p. 2100075.
105. Lee, Y.K., et al, *Room temperature electrochemical sintering of Zn microparticles and its use in printable conducting inks for bioresorbable electronics.* Advanced Materials, 2017. **39**(38): p. 1702665.
106. Li, J., et al., *Anhydride-Assisted Spontaneous Room Temperature Sintering of Printed Bioresorbable Electronics.* Advanced Functional Materials, 2020. **30**(29): p. 1905024.
107. Jayasayee, K., et al. , *Cold sintering as a cost-effective process to manufacture porous zinc electrodes for rechargeable zinc-air batteries.* Processes 2020. **8**(5): p. 592.
108. Greiner, M.T., et al., *Universal energy-level alignment of molecules on metal oxides.* Nature materials, 2012. **11**(1): p. 76-81.
109. Gamon, J., et al, *The effect of organic additives on the intergranular conductivity of Al-doped ZnO.* RSC advances, 2017. **7**(60): p. 38019-38027.
110. Li, R., et al, *An analytical model of reactive diffusion for transient electronics.* Advanced functional materials, 2013. **23**(24): p. 3106-3114.
111. Benramache, S., et al. , *The effect of film thickness on the structural, optical and electrical properties of ZnO thin films deposited by ultrasonic spray deposition.* Materials Research Express, 2019. **6**(12): p. 126418.
112. Todd, M.G., and Frank G. Shi., *Complex permittivity of composite systems: a comprehensive interphase approach.* IEEE Transactions on Dielectrics and Electrical Insulation, 2005. **12**(3): p. 601-611.
113. Lay, M., et al. , *Interphase volume calculation of polyimide/TiO 2 nanofibers nanocomposite based on dielectric constant model and its effect on glass transition.* Journal of Materials Science: Materials in Electronics, 2018. **29**: p. 20742-20749.
114. Alhabill, F.N., et al., *Introducing particle interphase model for describing the electrical behaviour of nanodielectrics.* Materials & Design, 2018. **158**: p. 62-73.

115. Ezzat, M., N. A. Sabiha, and M. Izzularab, *Accurate model for computing dielectric constant of dielectric nanocomposites.* Applied Nanoscience, 2014. **4**(3): p. 331-338.
116. Boongird, A., et al, *Biocompatibility study of glycofurol in rat brains.* Experimental Biology and Medicine, 2011. **236**(1): p. 77-83.
117. Bhattacharyya, A., et al, *Schottky barrier height engineering in β-Ga 2 O 3 using SiO 2 interlayer dielectric.* IEEE Journal of the Electron Devices Society, 2020. **8**: p. 286-294.
118. Chand, S., and Saroj Bala, *Simulation studies of current transport in metal–insulator–semiconductor Schottky barrier diodes.* Physica B: Condensed Matter, 2007. **390**(1-2): p. 179-184.
119. Çetin, H.İ.D.A.Y.E.T., et al., *Ti/p-Si Schottky barrier diodes with interfacial layer prepared by thermal oxidation.* Physica B: Condensed Matter, 2005. **364**(1-4): p. 133-141.
120. Khademi, M., and Dominik PJ Barz, *Structure of the electrical double layer revisited: Electrode capacitance in aqueous solutions.* Langmuir, 2020. **36**(16): p. 4250-4260.
121. Carvalho, J.T., et al, *Fully printed zinc oxide electrolyte-gated transistors on paper.* Nanomaterials, 2019. **9**(2): p. 169.
122. Ahn, H.-S., et al. , *Carbon-nanotube-interfaced glass fiber scaffold for regeneration of transected sciatic nerve.* Acta biomaterialia, 2015. **13**: p. 324-334.
123. Yeoh, S., et al. , *Rapid-stretch injury to peripheral nerves: comparison of injury models.* Journal of Neurosurgery 2020. **135**(3): p. 893-903.
124. Li, R., et al. , *Peripheral nerve injuries treatment: a systematic review.* Cell biochemistry and biophysics, 2014. **68**: p. 449-454.
125. Grinsell, D., and C. P. Keating, *Peripheral nerve reconstruction after injury: a review of clinical and experimental therapies.* BioMed research international, 2014.
126. Steed, M.B., et al, *Advances in bioengineered conduits for peripheral nerve regeneration.* Atlas of the oral and maxillofacial surgery clinics of North America, 2011. **19**(1): p. 119-130.
127. Al-Majed, A.A., et al, *Brief electrical stimulation promotes the speed and accuracy of motor axonal regeneration.* Journal of Neuroscience, 2000. **20**(7): p. 2602-2608.
128. Piech, D.K., et al, *A wireless millimetre-scale implantable neural stimulator with ultrasonically powered bidirectional communication.* Nature biomedical engineering, 2020. **4**(2): p. 207-222.
129. Silverå Ejneby, M., et al, *Chronic electrical stimulation of peripheral nerves via deep-red light transduced by an implanted organic photocapacitor.* Nature Biomedical Engineering, 2022. **6**(6): p. 741-753.
130. Chen, J.C., et al, *A wireless millimetric magnetoelectric implant for the endovascular stimulation of peripheral nerves.* Nature Biomedical Engineering, 2022. **6**(6): p. 706-716.
131. Freeman, D.K., et al, *A sub-millimeter, inductively powered neural stimulator.* Frontiers in neuroscience 2017. **11**: p. 659.

132. He, T., et al, *Self-sustainable wearable textile nano-energy nano-system (NENS) for next-generation healthcare applications.* Advanced Science, 2019. **6**(24): p. 1901437.
133. Lee, S., et al, *Toward bioelectronic medicine—Neuromodulation of small peripheral nerves using flexible neural clip.* Advanced Science, 2017. **4**(11): p. 1700149.
134. Otchy, T.M., et al, *Printable microscale interfaces for long-term peripheral nerve mapping and precision control.* Nature Communications, 2020. **11**(1): p. 4191.
135. Zhang, Y., et al., *Climbing-inspired twining electrodes using shape memory for peripheral nerve stimulation and recording.* Science advances, 2019. **5**(4): p. eaaw1066.
136. Song, K.-I., et al, *Adaptive self-healing electronic epineurium for chronic bidirectional neural interfaces.* Nature communications, 2020. **11**(1): p. 4195.
137. Choi, Y.S., et al, *Stretchable, dynamic covalent polymers for soft, long-lived bioresorbable electronic stimulators designed to facilitate neuromuscular regeneration.* Nature communications, 2020. **11**(1): p. 5990.
138. Yin, L., et al. , *Dissolvable metals for transient electronics.* Advanced Functional Materials, 2014. **24**(5): p. 645-658.
139. Lu, D., et al, *Transient Light-Emitting Diodes Constructed from Semiconductors and Transparent Conductors that Biodegrade Under Physiological Conditions.* Advanced Materials, 2019. **31**(42): p. 1902739.
140. Herrera, R., et al., *Characterization and degradation behavior of poly (butylene adipate-co-terephthalate) s.* Journal of Polymer Science Part A: Polymer Chemistry, 2002. **40**(23): p. 4141-4157.
141. Fernández, J., Agustin Etxeberria, and Jose-Ramon Sarasua, *In vitro degradation studies and mechanical behavior of poly (ε-caprolactone-co-δ-valerolactone) and poly (ε-caprolactone-co-L-lactide) with random and semi-alternating chain microstructures.* European Polymer Journal, 2015. **71**: p. 585-595.
142. Kunwar, A., et al. , *Quantitative cellular uptake, localization and cytotoxicity of curcumin in normal and tumor cells.* Biochimica et Biophysica Acta (BBA)-General Subjects 2008. **1780**(4): p. 673-679.
143. Lin, Y.-K., et al. , *Anti-psoriatic effects of indigo naturalis on the proliferation and differentiation of keratinocytes with indirubin as the active component.* Journal of dermatological science, 2009. **54**(3): p. 168-174.
144. Yazdani, M., et al. , *Beta-carotene/cyclodextrin-based inclusion complex: improved loading, solubility, stability, and cytotoxicity.* Journal of Inclusion Phenomena and Macrocyclic Chemistry, 2022. **102**(1-2): p. 55-64.
145. Pasdaran, A., et al, *Effects of some cosmetic dyes and pigments on the proliferation of human foreskin fibroblasts and cellular oxidative stress; potential cytotoxicity of chlorophyllin and indigo carmine on fibroblasts.* Journal of Cosmetic Dermatology, 2022. **21**(9): p. 3979-

3985.
146. Kehrl, J., et al, *Vesicular glutamate transporter inhibitors: Structurally modified brilliant yellow analogs.* Neurochemical Research, 2017. **42**: p. 1823-1832.
147. Joo, K.-M., et al, *Development and validation of UPLC method for WST-1 cell viability assay and its application to MCTT HCE™ eye irritation test for colorful substances.* Toxicology in Vitro, 2019. **60**: p. 412-419.
148. Ceylan, H., et al., *3D-printed biodegradable microswimmer for theranostic cargo delivery and release.* ACS nano, 2019. **13**(3): p. 3353-3362.
149. Soares dos Santos, M.P., and Rodrigo Bernardo., *Bioelectronic multifunctional bone implants: recent trends.* Bioelectronic Medicine, 2022. **8**(1): p. 1-13.
150. dos Santos, M.P.S., et al, *Instrumented hip implants: Electric supply systems.* Journal of biomechanics, 2013. **46**(15): p. 2561-2571.
151. Cai, L., et al, *Osseosurface electronics—thin, wireless, battery-free and multimodal musculoskeletal biointerfaces.* Nature Communications, 2021. **12**(1): p. 1-12.
152. Kim, Y., et al., *Chip-less wireless electronic skins by remote epitaxial freestanding compound semiconductors.* Science, 2022. **377**(6608): p. 859-864.
153. Jiang, S., et al., *Flexible metamaterial electronics.* Advanced Materials, 2022: p. 2200070.
154. Junio, R.F.P., et al., *Development and applications of 3D printing-processed auxetic structures for high-velocity impact protection: A review.* Eng, 2023. **4**(1): p. 903-940.
155. Wang, Z., et al., *Progress in auxetic mechanical metamaterials: structures, characteristics, manufacturing methods, and applications.* Advanced Engineering Materials, 2020. **22**(10): p. 2000312.
156. Qi, J., et al., *Recent progress in active mechanical metamaterials and construction principles.* Advanced Science, 2022. **9**(1): p. 2102662.
157. Li, F. and R. Hu, *Metamaterials-enabled sensing for human-machine interfacing.* Sensors, 2020. **21**(1): p. 161.
158. Kapnisi, M., et al., *Auxetic cardiac patches with tunable mechanical and conductive properties toward treating myocardial infarction.* Advanced functional materials, 2018. **28**(21): p. 1800618.
159. Olvera, D., et al., *Electroconductive melt electrowritten patches matching the mechanical anisotropy of human myocardium.* Advanced Functional Materials, 2020. **30**(44): p. 1909880.
160. Kim, B.S., et al., *2D reentrant auxetic structures of graphene/CNT networks for omnidirectionally stretchable supercapacitors.* Nanoscale, 2017. **9**(35): p. 13272-13280.
161. Kim, H.W., et al., *Hygroscopic auxetic on-skin sensors for easy-to-handle repeated daily use.* ACS applied materials & interfaces, 2018. **10**(46): p. 40141-40148.
162. YeonáLee, S., *High-performance, biaxially stretchable conductor based on Ag composites and hierarchical auxetic structure.* Journal

of Materials Chemistry C, 2020. **8**(5): p. 1556-1561.
163. Jang, B., et al., *Auxetic meta-display: Stretchable display without image distortion.* Advanced Functional Materials, 2022. **32**(22): p. 2113299.
164. Wang, Z., et al., *High-performance auxetic bilayer conductive mesh-based multi-material integrated stretchable strain sensors.* ACS Applied Materials & Interfaces, 2021. **13**(19): p. 23038-23048.
165. Jiang, Y., et al., *Auxetic mechanical metamaterials to enhance sensitivity of stretchable strain sensors.* Advanced Materials, 2018. **30**(12): p. 1706589.
166. Su, R., et al., *3D printed self-supporting elastomeric structures for multifunctional microfluidics.* Science advances, 2020. **6**(41): p. eabc9846.
167. Ji, J., et al., *Synthesis and characterization of room temperature vulcanized silicone rubber using methoxyl-capped MQ silicone resin as self-reinforced cross-linker.* Polymers, 2019. **11**(7): p. 1142.
168. Liao, K. and J. Zhu, *A Facile and Cost-Effective Method to Prepare a Robust Superhydrophobic RTV Silicone Coating.* Coatings, 2021. **11**(3): p. 312.
169. Wang, X., et al., *Preparation and properties of room-temperature-vulcanized silicone rubber using modified dopamine as a crosslinking agent.* Materials Research Express, 2022. **9**(4): p. 045304.
170. Wen, X., et al., *RTV silicone rubber degradation induced by temperature cycling.* Energies, 2017. **10**(7): p. 1054.
171. Yoon, I.S., et al., *Ag flake/silicone rubber composite with high stability and stretching speed insensitive resistance via conductive bridge formation.* Scientific reports, 2020. **10**(1): p. 1-8.
172. Kelly, B.E., et al., *Volumetric additive manufacturing via tomographic reconstruction.* Science, 2019. **363**(6431): p. 1075-1079.
173. Nam, S.-H., et al., *Photolithographic realization of target nanostructures in 3D space by inverse design of phase modulation.* Science Advances, 2022. **8**(21): p. eabm6310.
174. Kim, J.J., L.K. Allison, and T.L. Andrew, *Vapor-printed polymer electrodes for long-term, on-demand health monitoring.* Science advances, 2019. **5**(3): p. eaaw0463.
175. Kim, J.J., et al., *On-site identification of ozone damage in fruiting plants using vapor-deposited conducting polymer tattoos.* Science Advances, 2020. **6**(36): p. eabc3296.
176. Li, X., et al., *Evaporation-induced sintering of liquid metal droplets with biological nanofibrils for flexible conductivity and responsive actuation.* Nature Communications, 2019. **10**(1): p. 3514.
177. Kwon, J., et al., *Scalable electrically conductive spray coating based on block copolymer nanocomposites.* ACS applied materials & interfaces, 2020. **12**(7): p. 8687-8694.
178. Carey, T., et al., *Spray-coating thin films on three-dimensional surfaces for a semitransparent capacitive-touch device.* ACS applied materials & interfaces, 2018. **10**(23): p. 19948-19956.

Abstract

이 학위 논문은 사용자 맞춤형 3차원 구조 내에서 생체 인터페이스 전자 기기의 무선 제어 및 자극/센싱이 가능하도록 능동/수동 소자의 집적화를 단일 단계로 가능하게 하는 적층 제조 기반 생분해성 전자 소재의 개발에 관한 내용이다. 또한 다축 변형에 저항하는 전도체/구조체 메타구조와 in-situ 기상 증착을 통해 3차원 구조로 맞춤 제작할 수 있는 친환경 광경화성 레지스트 재료에 대한 개발에 대한 내용도 포함한다.

1장에서는 생체 인터페이스 전자 기기의 적층 제조의 필요성에 대해 논의한다. 맞춤형 접촉을 위해 기존의 접근 방식인 얇은 박막/연성 전자 제작 기술은 신축성 배선, 소자를 제작하거나 역설계를 사용했다. 이러한 접근법은 부착 시 신뢰성 문제, 복잡성에 따른 높은 비용, 3차원 공간 내 제한된 공간 활용도/디자인 자유도 등의 문제가 있을 수 있다. 또한 적층공정으로 이를 구현하기 위해선 무선 작동을 위해 voxel화된 반도체도 필요로 했다. 이를 위해 적층 제조를 사용하여 3차원 맞춤형 구조 내에서 능동/수동 소자를 집적하고 디바이스를 제작하는 것을 목표로 한다.

2장에서는 전도성, 반도체 및 유전체 잉크를 포함한 3차원 인쇄 가능한 생분해성 전자 잉크의 개발을 목표로 하였다. 전자 잉크의 전도성을 향상시키기 위한 전략과 3차원 인쇄 가능한 반도체 소재에 대한 새로운 접근법을 제안 및 개발하였다. 서로 다른 잉크 간의 접합에 대한 연구를 통해 오믹, 쇼트키 및 PN 접합을 기반으로 한 능동소자 제작을 하였다. 또한 이 장에서는 복잡한 3차원 정적/동적 구조에 맞춤형으로 제작된 물리, 화학 및 생체 센서의 활용성을 확인하였다.

3장에서는 2장에서 개발한 생분해성 전자 잉크와 잉크 간 접합 관계를 활용하여 인터페이스 방식을 3가지로 분류하여 주변 인터페이스, 관통

인터페이스 및 내장 인터페이스와 같은 다양한 접촉 모드에 대한 기기 개발을 제시한다. 이러한 기기는 무선 전기 자극, 3D 구조에 대한 정렬된 신호 변환 배선 및 무선 압력 모니터링을 목표로 제작하였다. 무선 전기 자극기의 경우 소동물 및 대형 동물 실험으로 체내 자극 가능성과 기기의 치료 효과를 검증하였다.

4장은 다축 변형 하에서 안정적인 작동이 가능한 전자 기기의 제작을 목표로 한다. 음의 포아송 비율을 가진 메타재료 구조를 실리콘 엘라스토머와 은을 기반으로 한 연성 전도체와 프레임 재료를 사용하여 3D 인쇄하였다. 이 때 다중 재료 인쇄를 통해 구조 및 전자 구성 요소의 분리를 한 실체 내에서 구현하였다. 이 디자인은 팽창 중에도 안정된 저항을 보장한다. 수동적 구성 요소를 기반으로 한 다양한 센서와 히터가 제작되며, 기기의 적용 가능성을 보여주기 위해 소프트 액추에이터와의 결합 가능성을 확인하였다.

5장에서는 3차원 맞춤형 형태에 대하여 패터닝된 기상 증착을 가능하게 하는 새로운 포토레지스트에 대한 연구를 진행하였다. 생분해성이고, 생적합성이 높은 재료로 구성된 친환경적이고 3차원 패턴 가능한 포토레지스트를 개발하였다. 포토레지스트의 패턴화 가능성은 3차원 개체, 돼지 피부 및 잎에 대해 검증하였다. 이 포토레지스트는 물을 사용하여 패턴 생성이 가능하고, 약 알칼리성 물 또는 프로필렌 카보네이트를 사용하여 제거가 가능하였다. 이것은 기상 증착을 통한 전자 소자 제조용 마스크로 사용하거나 유체의 채널 제작을 위한 금형으로 사용될 수 있음을 확인하였다.

Acknowledgement

2018년도 1월 2일에 처음 교수님을 뵙고 연구실을 셋업했던 날이 엊그제 같은데 벌써 5년이라는 시간이 흘러 재료공학과 박사 학위 졸업을 하게 되었습니다. 3D 프린터로 생분해성 전자소자를 제작하는 연구는 기존에 참고할 수 있는 논문이 많이 없어 수많은 시행 착오를 겪으며 저에게 많은 도전으로 다가왔지만, 이때마다 물성을 체득하고, 현상들에 대해 더 많은 공부를 할 수 있는 기회가 왔다고 여기며 긍정적으로 이겨냈습니다. 세운 가설에 맞춰 운이 좋게 결과가 잘 나왔을 때 몇 번의 희열은 지금도 생각만 하면 가슴이 벅찹니다. 이 연구가 완성되기까지 저 혼자선 절대 할 수 없었고, 도와주신 분들께 이 글을 통해 감사를 드리고자 합니다.

먼저 교수님들과 박사님들께 감사의 말씀을 드리고자 합니다. 저의 지도 교수님이신 강승균 교수님께 정말 감사드립니다. 부족했던 제가 성장할 수 있도록 끊임없이 격려해주시고, 많은 피드백과 지원을 해주셔서 아직도 부족하지만 재료공학과로써 박사 학위를 취득할 수 있었습니다. 바쁘신 중에도 많은 시간을 내주시어 앞으로 제 연구 인생에서의 기반을 닦을 수 있도록 격려를 해주신 것에 정말 감사드립니다. 앞으로 BIE 연구실의 첫 박사 졸업생으로써 부끄럼이 없는 제자로 성장할 수 있도록 노력하겠습니다.

제작한 전자소자들을 동물실험에 잘 적용할 수 있도록 조언을 주시고, 직접 실험에도 참여해주셨던 현정근 교수님께도 감사드립니다. 이전에 칠판 위에 생물학적 개념들을 하나씩 자세히 설명해주신 것이 아직도 기억에 많이 남습니다. 또한 개발 중인 기술이 더 발전적으로 나아가기 위해 필요한 요소들에 대해 말씀주시고, 동물 실험도 같이 해주셨던 이강식 박사님, 전도성 평가를 할 수 있도록 플랫폼을 제작해주셨던 김주영 교수님, 실리콘 웨이퍼 밀링을 하여 실리콘 파티클에 대해서도

연구할 수 있도록 해주셨던 김우병 교수님, 동물실험에 전자소자를 적용하셨던 경험들과 노하우를 전수해주시고, 지원을 해주시고, 학위 심사위원으로도 참석해주셨던 구자현 교수님, 무선 통신에 대한 평가 기준들과 무선 전력 관련 연구의 진행하는 방향에 대해서 코멘트 주셨던 김정현 교수님, 제작하신 프린터를 기반하여 개발한 잉크들을 더 높은 해상도로 뽑을 수 있게 해주시고, 학위 심사위원으로도 참석해주셨던 설승권 박사님께 정말 감사드립니다. 또한 바쁘신 중에도 시간을 내어주시며 열정적으로 제 학위 연구에 대하여 양질의 코멘트를 주셔서 무사히 학위를 마칠 수 있도록 해주신 선정윤교수님, 이관형 교수님께 정말 감사드립니다.

다음으로는 기술적 지원을 많이 주셨던 기업 분들에게도 감사의 말씀을 드립니다. 3D 프린팅할 때 제품에 대한 기술적 지원 및 논의를 진행해주셨던 Cellink의 Daniel, Matthew, 김영필 과장님, 강선아 선생님, 이승희 선생님, Tomoko 에게 감사드립니다. 프린팅에 필요한 물품들은 언제든 빠르게 보내주셨던 알티코퍼레이션 손성근 부장님, 병현바이오텍 이호민 과장님께도 감사드립니다. 또한 잉크의 물성을 측정하기 위해 정말 많은 샘플과 함께 여러 번 찾아뵈어도 마다하지 않으시고, 항상 도와주셨던 Antonpaar 코리아 전설희 선생님, 김혜지 선생님, 이현휘 과장님께도 정말 감사드립니다. 또한 3D 프린팅에 대해 처음 알아가고, 프린터기를 제작할지 기성제품을 구매할지 많은 고민이 있을 때에 도움을 주셨던 반석정밀공업 김용현 이사님, 애니모션텍 김주형 선생님께 정말 감사드립니다. 직접 박람회나 기업으로 찾아뵈어 현장에서 스케일에 대한 감각과 프린팅이라는 분야에 대해 많이 배울 수 있었던 것 같습니다. 또한 운이 좋게 발견한 3차원으로 마킹을 할 수 있는 장비를 개발한 키엔스와 마킹기를 이용한 다양한 샘플 테스트, 장비 계약 및 3차원 스캐닝 등 기술적 지원을 도와주신 박상국 과장님, 안정민 대리님께도 감사드립니다. 또한 불쑥 전화하여 Deep UV 데모를 부탁드렸는데 흔쾌히 도와주셨던 DTX 사장님, 오송실험동물센터에서 계약과 실험이

원활히 진행될 수 있도록 친절하게 도와주셨던 이선원 선생님, 그리고 무슨 물건이든 연구에 필요하다면 구해주시고, 친절하게 대해주셨던 씨앤씨랩 박준기 부장님, 김유리 선생님, 대한과학 허광열 팀장님, 엘케이랩 박상철 부장님 정말 감사드립니다. 또한 제 전문연 생활과 저희 과제 연구비를 책임져주시는 신소재 공동연구소 강혜영 선생님, 이경희 선생님, 권순미 선생님께도 정말 감사드립니다. 또한 카이스트에 있을 때에 행정적으로 많은 도움을 주셨던 김진희 선생님과 서울대에 있을 때 도움을 주신 오송희 선생님, 계혜란 선생님, 김정선 선생님, 김경숙 선생님께 정말 감사드립니다. 컨텐츠를 잘 표현하기 위해 일러스트에 대해서도 토의를 진행해주시고, 시안도 제작 해주셨던 임소진 작가님 정말 감사드립니다.

또한 긴 세월 같이 함께하며 동고동락했던 형, 누나, 동생들에게도 정말 감사드립니다. 랩 셋업을 같이 해준 멤버들, 랩이 커지면서 체제를 안정화시키는데 노력을 해주었던 멤버들, 연구적으로 해결이 안될 때 서로 토론하거나 같이 실험하며 집념으로 해결을 같이 해냈던 멤버들 누구 하나 빼놓을 수 없이 모두가 BIE가 잘 운영되기 위해 노력해준 성근형, 재영이형, 민하형, 지오누나, 재환이, 경섭이, 승민이, 지우, 윤남이, 준석이, 명균이, 준민이, 영서, 세훈이, 주현이, 예슬누나, 용우, 우진이, 이정이, 지은이, 민성이형, 영인이, 유정이, 영환이, 태경이, 혜준씨, 민정씨, 인턴친구들 (유림, 도훈, 성우, 명준, 수환, 석민, 임덕), 대학원 선배로써 경험하신 내용을 공유해주시고, 조언 해주셨던 우주형, 종형이형, 준상이형, 경열이형, 종호형에게도 감사드립니다.

공동연구를 같이 진행했던 다른 대학, 기관 연구원님들께도 정말 감사드립니다. 미흡한 기술로 제작한 전자소자임에도 전폭적으로 실험을 해주시며 결과가 실패해도 발전적으로 나아가 결국 잘해낼 수 있도록 도와주신 전주익 박사님, 전도성 평가를 위해 필요로 했던 스텐실 마스크를 많이 제작해 주셨던 박선영 박사님, 무선 전력 및 NFC 칩 관련하여

논의를 진행해 주셨던 김준우 연구원님, 또한 개발한 기술을 바탕으로 세포 배양 플랫폼을 제작하기 위해 세포 테스트를 도와주셨던 이경우 연구원님과 정고은 연구원님, 광학적 소결 시도를 위해 도와주셨던 박재호 박사님 감사드립니다. 또한 연구 경험에 대해서도 많이 공유주시고, 나노파티클 합성과 관련하여 많은 가르침을 주신 Reza 박사님, 그리고 함께 파티클 연구를 진행했던 왕정함 연구원님 정말 감사드립니다.

또한 지칠 때 정서적으로 응원해주며 긍정적 에너지로 함께했던 친구들 준식이, 재현이, 치우, 승민이, 훈식이형, 준홍형, 양환형, 욱재, 찬우형, 곤희형, 선이, 혜리, 예지, 희섭이형, 용우형, 민재, 순혁이, 상균형, 동훈이, 민혁이형, 우용이형, 정봉이형, 카이스트 공정 교육팀, 훈련소 동기들, 고든 학회에서 만난 분들께 정말 감사드립니다. 부족한 저에게 자신감을 주고, 앞으로 오랜 시간 함께할 세연이에게도 정말 고맙습니다. 리프레쉬 하는 시간은 제가 연구에 더 정진할 수 있도록 만들어주는 시간이었습니다.

마지막으로 제가 학위과정을 무사히 마칠 수 있도록 긴 세월 기쁠 때나 힘들 때나 항상 옆에서 응원해주시고, 전폭적으로 믿어주신 우리 엄마, 아빠, 효선이, 할머니, 외할아버지, 외할머니, 고모들, 삼촌들, 사촌들께 무한한 감사드립니다.

대학원 생활 동안 제가 배우고, 경험한 내용을 바탕으로 세상에 도움이 되는 공학도로써 성장해나가도록 하겠습니다.

2023년 08월 1일

이주용